Volume 94, Number 3, May–June 1989
Journal of Research of the National Institute of Standards and Technology

Contents

Articles

Volume 94, Number 3, May–June 1989
Journal of Research of the National Institute of Standards and Technology

News Briefs

The Secretary of Commerce has determined that the publication of the periodical is necessary in the transaction of the public business required by law of the Department. Use of funds for printing this periodical has been approved by the Director of the Office of Management and Budget through October 1, 1989.

United States Government Printing Office, Washington: 1989

Volume 94, Number 3, May–June 1989
Journal of Research of the National Institute of Standards and Technology

A Brief Review of Recent Superconductivity Research at NIST

Volume 94 Number 3 May–June 1989

D. R. Lundy,
L. J. Swartzendruber,
and L. H. Bennett

National Institute of Standards
and Technology,
Gaithersburg, MD 20899

A brief overview of recent superconductivity research at NIST is presented. Emphasis is placed on the new high-temperature oxide superconductors, though mention is made of important work on low-temperature superconductors, and a few historical notes are included. NIST research covers a wide range of interests. For the new high-temperature superconductors, research activities include determination of physical properties such as elastic constants and electronic structure, development of new techniques such as magnetic-field modulated microwave-absorption and determination of phase diagrams and crystal structure. For the low-temperature superconductors, research spans studying the effect of stress on current density to the fabrication of a new Josephson junction voltage standard.

Key words: ceramics; copper oxides; cryogenic engineering; crystal structure; electronic structure; materials science; measurement science; overview; perovskites; superconductivity.

Accepted: January 26, 1989

Contents

1. Introduction

Research in superconductivity at NIST has a long history, in part because of its important applications to measurements and materials science. The recent discovery of materials with unexpectedly high superconducting transition temperatures has brought renewed interest in the science and technology of superconductors throughout the world. The purpose of this paper is to briefly review recent activities at NIST in this field and to discuss current usage and future possibilities for both conventional and high temperature superconductors. Some references will be made to historical superconductivity contributions at NIST but a complete review is not attempted.

2. Background

The field of superconductivity began with the discovery by H. Kamerlingh-Onnes in 1911 that mercury wire at 4.2 K had zero electrical resistance. Zero resistance implied transmission of current at any distance with no losses, the production of large magnetic fields, or—because a superconducting loop could carry current indefinitely—storage of energy. These applications were not realized because, as was quickly discovered, the superconductors reverted to normal conductors at a relatively low current density, called the critical current density, J_C, or in a relatively low magnetic field, called the critical field, H_C. In 1916, Silsbee, at the National Bureau of Standards, hypothesized [1] that the critical current for a superconducting wire was equal to that current which gave the critical field at the surface of the wire. The reason for this behavior was not made clear until the discovery [2] of the Meissner effect in 1933.

The discovery and development, in the 1950s and 1960s, of superconductors which can remain superconducting at much higher fields and currents made practical the production of useful superconducting magnets (see table 1). Such high-field superconductors, which exhibit two critical fields designated H_{C1} and H_{C2}, are called type-II. In 1950, another NBS scientist, E. Maxwell, was the discoverer [3] of the isotope effect, which was also independently discovered by Serin et al. [4]. This experimental observation was an important key to theoretical explanations of the mechanism of superconductivity. In the isotope effect, the critical temperature for many superconductors depends on the isotopic mass, indicating that lattice vibrations are involved in the superconductivity, and that the attractive coupling between electrons is through the lattice vibrations (i.e., phonon-mediated). The discovery [5] of the Josephson effect in 1962 opened up exciting potential for the use of superconductors

Table 1. Selected superconductor applications

Application	Advantage	Comments
Generators with superconducting wires in rotors	Lifetime cost savings up to 40%	U.S. built a 10 MW prototype; USSR is building a 300 MW prototype
Energy storage rings	Efficient, site independent, can revert from charging to discharging mode in less than 1 second. Can stabilize system	Pilot programs
Power transmission lines	Reduced resistive losses	Prototypes tested
Magnets for magnetic resonance imaging	Superconducting magnets result in shorter exposure times and sharper images compared to conventional magnets	Largest current commercial application of superconductivity; wide acceptance as medical diagnostic tool
Chip interconnects	Lack of electrical resistance; reduces heat buildup; permits dense packing...rapid transmission of signal	In research stage
SQUIDS (superconducting quantum interference devices)	Extremely sensitive to magnetic fields	Used for mineral exploration; anti-submarine warfare potential; development underway for use in medical diagnosis
Josephson Junction switches	Fast switching times, low power dissipation, dispersionless transmission	Used in fast-sampling oscilloscope; potential computer logic elements
Josephson Junction voltage standards	Reliable, stable. Absolute voltage based on fundamental constants	In use by, and available from, NIST
Magnets for fusion devices	Magnets to confine plasma	Prototype systems constructed in France and the Soviet Union
High-energy physics	High fields to guide beams, reduced energy consumption	Superconducting supercollider
Ship propulsion (motors)	Smaller, quieter motors; elimination of gearbox	Navy has protoype
Magnetohydrodynamic (MHD) power generation	High fields interact with a plasma to generate electricity	Prototypes constructed by the Soviet Union
Magnets for MHD ship propulsion	Quiet, more efficient, higher potential speeds	Demonstrated by Japan
Magnetic casting	Eliminates contamination	
Magnetic separation	Separates weakly magnetic materials	
Magnetic bearings	Eliminates friction	
IR sensors	Smaller packages	
Magnets for magnetically levitated trains (MAGLEV)	Rapid and efficient mode of transportation	Demonstrated by Japan

in measurement science and in high-speed electronic devices.

Until 1986, the highest critical temperature obtained for any superconductor was only 23.2 K. This meant that superconductors had to be cooled by liquid helium—an expensive and sometimes unreliable process. Consequently, many potential applications were not commercially viable. In addition, most scientists had come to regard superconductivity as a mature field with little possibility for any significant increase in critical temperatures. All this suddenly changed with the discovery by K. A. Bednorz and J. G. Müller of high-temperature superconductivity.

In April 1986, Müller and Bednorz published a paper [6] on the possible existence of superconductivity in a ceramic material, La-Ba-Cu-O, with a superconducting transition temperature, T_C, of 30 K, the first increase since 1973. Their discovery was the result of several years of extensive investigations on metal oxides, some of which had earlier been shown to be superconducting. It is noteworthy that superconductivity in oxides had been known for many years. In fact the first oxide superconductor was discovered at NIST. In 1964, Cohen predicted [7] that, based on the Bardeen-Cooper-Schrieffer (BCS) theory [8], semiconductors could become superconductors. At this time a metal-oxide semiconductor—$SrTiO_3$—being investigated at NIST seemed to have the characteristics postulated by Cohen as necessary for superconductivity. Kahn and Leyendecker [9] had determined the energy band structure of $SrTiO_3$ and Frederikse et al. [10] had determined the density of states in the conduction band. Schooley et al. [11] found superconductivity below 0.3 K in reduced $SrTiO_3$ in 1964; this oxide was demonstrated to be a type-II superconductor by Ambler et al. [12] in 1966 (see fig. 1). T_C was only 0.3 K however. Though substituting Ca and Ba for Sr [13] raised the T_C to 0.5 K, the low critical temperatures limited general interest in these materials.

According to Müller and Bednorz [6], their research was influenced by the French work on the La-Ba-Cu-0 system [14]. However, the French scientists were not looking for superconductivity. When researchers from the University of Tokyo [15] confirmed the findings of Müller and Bednorz, the era of "High-Temperature Superconductivity" was ushered in.

The end of 1986 and the beginning of 1987 was marked by synthesis of rare-earth metal oxides of increasingly higher T_C, culminating with the discovery [16] of the Y-Ba-Cu-O (YBCO) superconductor with a T_C of 93 K. This was a significant breakthrough because the material was superconducting in liquid nitrogen (boiling point=77 K). Nitrogen is much more abundant than helium, much less expensive, and liquid nitrogen cryogenic systems are less complex than systems using helium refrigeration. One application which could benefit from nitrogen cooling is the development of hybrid microelectronic technology (semiconductor-superconductor devices)—both gallium arsenide and silicon can be tailored to perform better at liquid nitrogen temperatures.

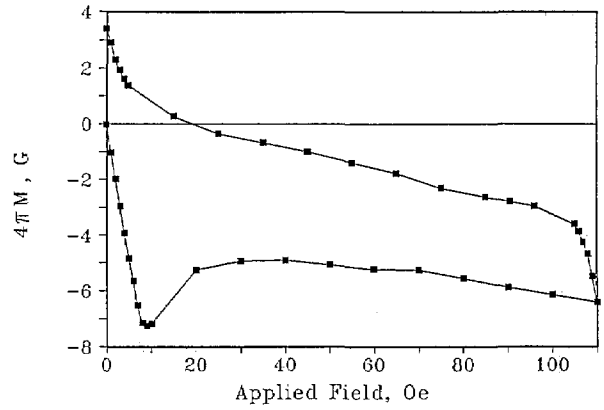

Figure 1. Partial hysteresis loop of $SrTiO_3$ obtained at 0.15 K using a ballistic galvanometer. The shape of the loop indicates that $SrTiO_3$ is a type-II superconductor. (Unpublished data courtesy of J. F. Schooley.)

The ease of making YBCO permitted its investigation by many laboratories. In fact, a number of high school students synthesized it for use in science fair projects. At various times researchers reported T_C's greater than 100 K—some reported superconductivity at room temperature and above. These observations were not confirmed; many of the results were irreproducible or the samples were not stable. At the end of 1987, the highest T_C stood at 95 K. In February 1988, Japanese, Chinese, and U.S. researchers found superconductivity in copper-containing oxides without rare earths. These new non-rare-earth containing superconductor materials incorporate either bismuth or thallium. Compounds containing the latter have a confirmed T_C of $\approx$127 K. These new high-temperature superconductors containing bismuth or thallium may have some advantages over the superconductors containing rare-earths. Since the critical current density increases as T/T_C decreases, a T_C far above the operating temperature of liquid nitrogen (77 K) is advantageous. Furthermore, the new materials are more stable than the rare earth superconductors; they do not lose oxygen or react with water.

In addition to trying to develop new high-T_C materials, researchers also were trying to fabricate materials with improved critical current densities (J_C). Current densities as high as 10^5-10^6 A/cm^2 may be needed for applications such as magnets, motors, and electronic components. The high-temperature superconductors are ceramics and have all the brittleness problems associated with non-superconducting ceramics. In addition, J_C is not an intrinsic property of superconductors but is a function of the processing procedure. The rare-earth superconductors also have highly directional properties. Therefore, a crucial problem is to fabricate the material into a useful shape and still have sufficiently high J_C and mechanical strength for practical applications.

Single crystal films of YBCO have current densities above a million A/cm^2. However, results for bulk polycrystalline materials are orders of magnitude less. Recently, researchers have grown non-oriented polycrystalline thallium films with J_C in the millions [17]. Novel processing techniques such as explosive compaction, rapid solidification and laser ablation are currently being explored.

NIST personnel have been actively engaged in fabricating and characterizing high-T_C superconducting materials. This paper is a brief synopsis of their wide-ranging activities. Some mention of significant work in other superconductors will also be made.

3. Crystal Structure

As was true for the previously mentioned $SrTiO_3$, the superconducting YBCO phase is a distorted perovskite [18]. Ideal perovskites have the form ABX_3, where A and B are metallic cations and the X atoms are non-metallic anions. In superconducting yttrium barium copper oxide, the structure (fig. 2) is a defect perovskite of the form $YBa_2Cu_3O_{7-x}$ (YBCO). Oxygen and oxygen vacancies are the key to the superconductivity. One widely-used method for refining the structure of YBCO is neutron diffraction because x-rays are not sensitive to oxygen atoms.

$YBa_2Cu_3O_{7-x}$ with $x=0$, 0.2, 0.5, and 1 was studied [19–22] using the neutron diffraction facilities of the NIST reactor. $YBa_2Cu_3O_7$ and $YBa_2Cu_3O_{6.8}$ are orthorhombic and superconducting, and are characterized by Cu-O chains along the b axis. In the O_7 material, oxygen atoms occupy 4 different sites with O(4) forming chains along the b-axis direction of the orthorhombic cell. The environments of the barium atoms and the copper atoms located at (000), (00z) change significantly with the amount of oxygen in the cell. $YBa_2Cu_3O_6$, which is tetragonal and a semiconductor, is derived from $YBa_2Cu_3O_7$ by removing oxygen along the b axis. While all the oxygen sites are occupied in the O_7 material, in the $O_{6.8}$, there are oxygen vacancies located in the chains. The superconducting T_C is reduced for deviations from O_7, indicating that oxygen vacancies disrupt conduction pathways.

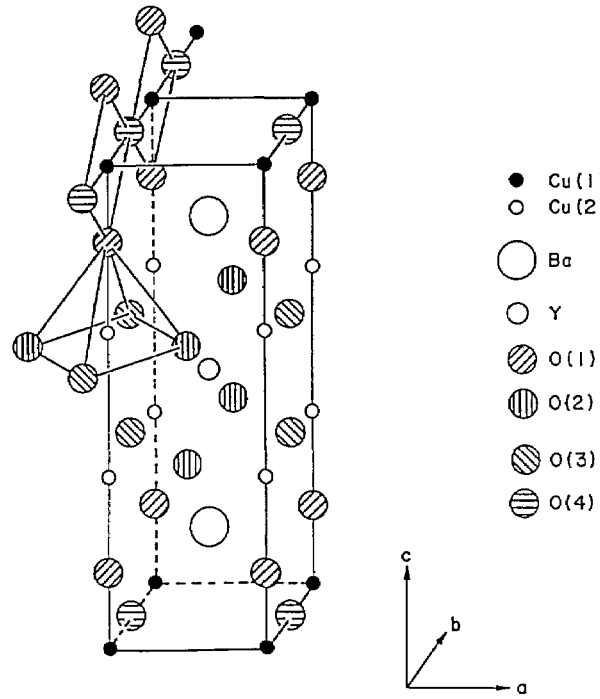

Figure 2. Crystal structure of YBCO as determined from neutron diffraction showing location of the four O sites, two Cu sites and single Ba and Y sites [21].

The crystal structure of a strontium analog of La-Ba-Cu-O, $La_{1.85}Sr_{0.15}CuO_4$, was also examined by neutron diffraction [23]. This highly two-dimensional structure, shown in figure 3, was found to be tetragonal at ambient temperature, but became orthorhombic at 200 K, resulting in the buckling of the Cu-O planes.

4. Impurity Effects

One of the outstanding questions in high-T_C $YBa_2Cu_3O_7$ superconductors is the relative importance of the Cu-O_2 planes [Cu(2)-site] and the Cu-O chains [Cu(1)-site]. Zn and Ga [24] have been used

to selectively substitute the Cu(2) and Cu(1) sites while maintaining the oxygen content near 7, as determined using neutron diffraction. These results, plus other recent work on Al, Co, and Fe substitutions, have shown that, in general, 3^+ ions (e.g., Ga, Co, etc.) substitute predominantly for Cu^{++} on the chain sites, suppress the orthorhombic crystal distortion, and enhance the overall oxygen content above 7 due to valency effects. On the other hand, di-positive Zn^{++}, which substitutes only on the "plane" sites, retains the orthorhombic structure, but rapidly destroys superconductivity with only a few percent Zn substitution. These neutron results (combined with bulk data) have demonstrated that the integrity of the planes is much more important in sustaining high-T_C superconductivity than the chains, and have also shown that the orthorhombic cell distortion is not essential for high transition temperatures.

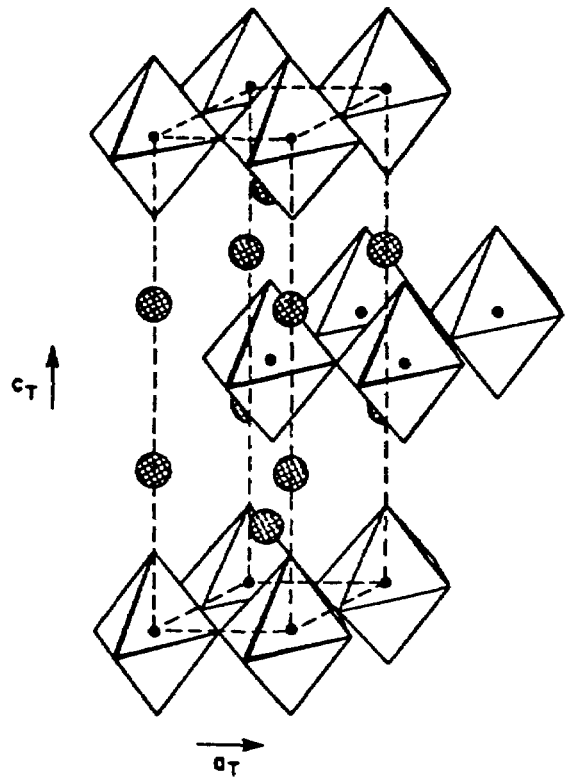

Figure 3. Generalized view of the highly two-dimensional tetragonal $La_{1.85}Sr_{0.15}CuO_4$ structure. On the scale of the figure, the orthorhombic and the tetragonal structures are not distinguishable except that the orthorhombic unit cell is twice the area in the plane perpendicular to c. The large shaded areas are La and Sr atoms; the small circles, Cu. Oxygen atoms are at the vertices of polyhedra [23].

Much of the prevailing theoretical work pertaining to the origin of the superconducting pairing in the high-T_C superconductors has focussed on a magnetic coupling of spins. $YBa_2Cu_3O_{7-x}$ with total oxygen content below ≈ 6.5 (i.e., $x > 0.5$) has been shown to exhibit strong antiferromagnetic correlations. To examine these matters in more detail, neutron diffraction studies [25] were carried out on materials in which Co has been substituted for the Cu on the "chain" site in order to enhance the magnetic interactions. The results showed magnetic ordering temperatures near 400 K, representing more than enough energy to account for the ≈ 95 K superconducting transition temperatures. For Co concentrations of 20%, distinct ordering temperatures were found for plane (≈ 400 K) and for chain (≈ 200 K) site antiferromagnetic orderings, while for 80% substitutions, both sites ordered at the same temperature (≈ 435 K). The form of the temperature dependence of the observed magnetization revealed strong couplings, both within the planes and also between chain and plane sites.

By using the Mössbauer effect in Fe-doped rare earth-barium-copper-oxygen samples (with the rare earth being Y, Pr, or Er) the antiferromagnetic coupling correlations could be directly observed [26, 27]. Since the Fe atoms substitute for the Cu on both chain and plane sites, the antiferromagnetism present on the plane sites and the paramagnetism on the chain sites could be simultaneously observed in the Mössbauer patterns. It was also demonstrated that asymmetries in the Mössbauer spectra are the result of a preferential alignment of the crystallites that arise during the normal sample preparation process.

5. Synthesis

Phase equilibria diagrams provide phase compositions and relationships under specific conditions. Such information is needed to characterize materials and develop synthesis procedures. Roth and his colleagues have been active in determining phase relationships for the Y-Ba-Cu-O system. Preliminary phase diagrams were constructed [28] for the binary systems $BaO\text{-}1/2Y_2O_3$; BaO-CuO; and $1/2Y_2O_3\text{-}CuO_x$, the bounding oxide systems of the ternary, and Y-Ba-Cu-O. Nine compounds are found in the $BaO\text{-}Y_2O_3\text{-}CuO_x$ system [29, 30] in the temperature range 950-1000 °C. Three of the compounds, $Ba_2YCu_3O_{7-x}$ (the superconducting phase), BaY_2CuO_5 (the "green" phase which is found to

exist with other phases), and $Ba_3YCu_2O_z$ were characterized by x-ray diffraction (XRD) [31-33]. Substitutions of lanthanides for yttrium in BaY_2O_5 were also characterized by XRD [34]. Fourteen standard reference patterns for six high-T_C superconducting and related phases have been reported [35]. Roth [28] found that all compositions in the ternary system containing 50% BaO always showed a small amount of the green phase. A tenth phase, Ba_2CuO_3, which has a melting point below 950 °C was characterized by XRD [36]. Studies of phase equilibria in air [37] showed that the superconductor phase melts through a four-phase region (fig. 4) from about 950-1002 °C. This region is due to the presence of CO_2, probably mainly in the liquid phase. The presence of CO_2 in the superconducting phase was inferred. The transition from tetragonal to orthorhombic structure was concluded to be metastable and no large primary phase field consisting only of the superconducting phase and liquid was identified.

The substitution of SrO for BaO in the $BaO:Y_2O_3:CuO$ system was studied to determine the extent of solid solution of Sr in YBCO and to identify any new phases. It was found that Sr could be substituted for Ba up to about 60%. There were no ternary compounds in the Sr-Y-Cu-O equivalent to the three ternary phases in the Ba system, but a new binary phase $Sr_{14}Cu_{24}O_{41}$ was found. The SrO-CaO-CuO system was also studied as part of an investigation of the $SrO\text{-}CaO\text{-}Bi_2\text{-}O_3\text{-}CuO$ system. At 950 °C, there were three extensive solid solutions at (Sr, Ca):Cu ratios of 2:1, 1:1, and 24:41. A new ternary $Sr_xCa_{1-x}CuO_2$ (x0.15) was found and a new phase, probably $CaCu_2$, stable only below ~740 °C, was identified [38, 39].

Since the oxygen content in $YBa_2Cu_3O_{7-x}$ strongly affects the superconducting and structural properties, the effects of variations in annealing (oxygenating) were studied. Single-phase samples were annealed at temperatures from 400 °C to 1000 °C [40, 41], then quenched in a liquid-

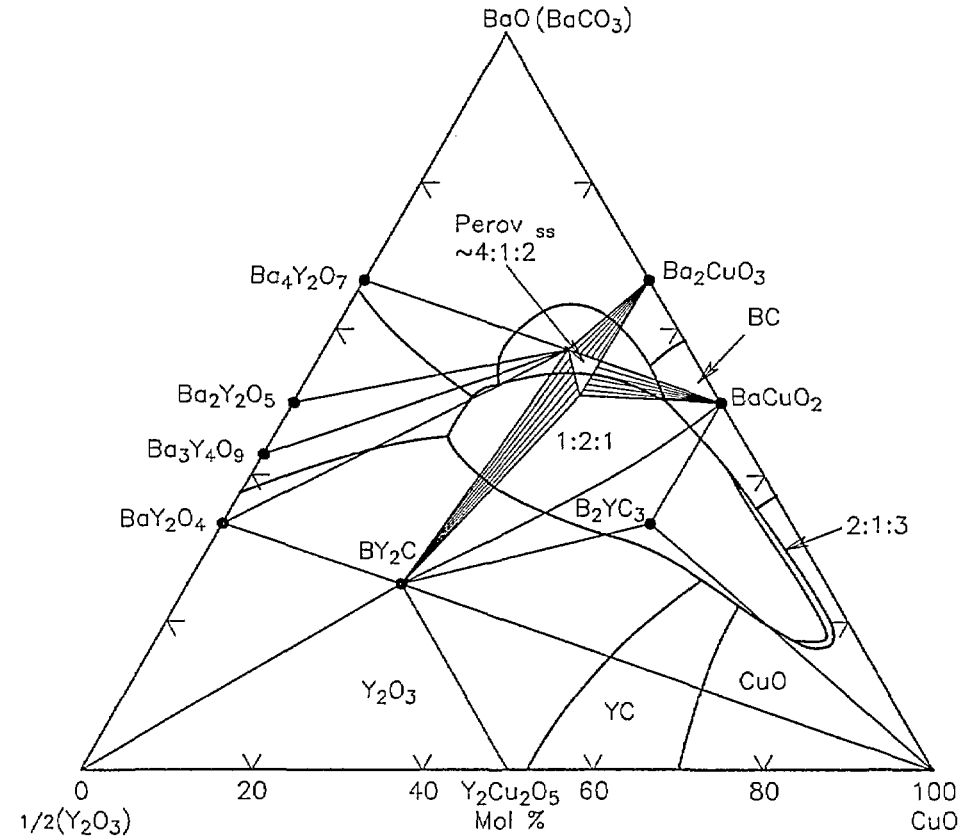

Figure 4. Ternary phase diagram of Y-Ba-Cu-O constructed from figures 1 and 6 of reference [37]. (Unpublished figure courtesy of R. Roth.)

nitrogen-cooled copper cold well, through which liquid-nitrogen-cooled helium gas was passed at a rapid rate. The goal was to quench in the high-temperature structures and stoichiometries. Samples were initially examined by x-ray diffraction. It was observed that, as the annealing temperature decreased, the ceramic became more orthorhombic—going from fully tetragonal at 1000 °C to fully orthorhombic at 400 °C (fig. 5). The phase transition occurred at 708-719 °C. The dependence of cell volume on temperature was not linear, becoming substantial only at 400-650 °C, the orthorhombic region. The limiting volumes were the volume of $YBa_2Cu_3O_7$ annealed in air and $YBa_2Cu_3O_6$ annealed in argon. Two possible orthorhombic regions were indicated—$a<b=c/3$, and $a<b<c/3$. ac susceptibility measurements were made for samples annealed up to 708 °C (samples annealed above 750 °C showed no Meissner effect). As shown in figure 6, a plot of T_{Co} (T_C onset) versus annealing temperature showed two plateaus—91 and 58 K. While these might indicate two different orthorhombic phases, lack of corroborating x-ray data prevented a firm identification. $YBa_2Cu_3O_{7-x}$ was also examined by thermogravimetric analysis (TGA) and differential scanning scanning calorimetry (DSC). TGA results also gave indications of two regions. DSC/TGA analysis showed a thermal event when $YBa_2Cu_3O_{7-x}$ was heated to 900 K which might be the result of microhomogeneities or of discontinuities in the oxygen vacancy ordering [42]. DSC studies of this material [43] showed that the phase transition does not associate with an enthalpy change, a characteristic of second-order transitions. Based on this and the x-ray data, the phase transition appears to be a

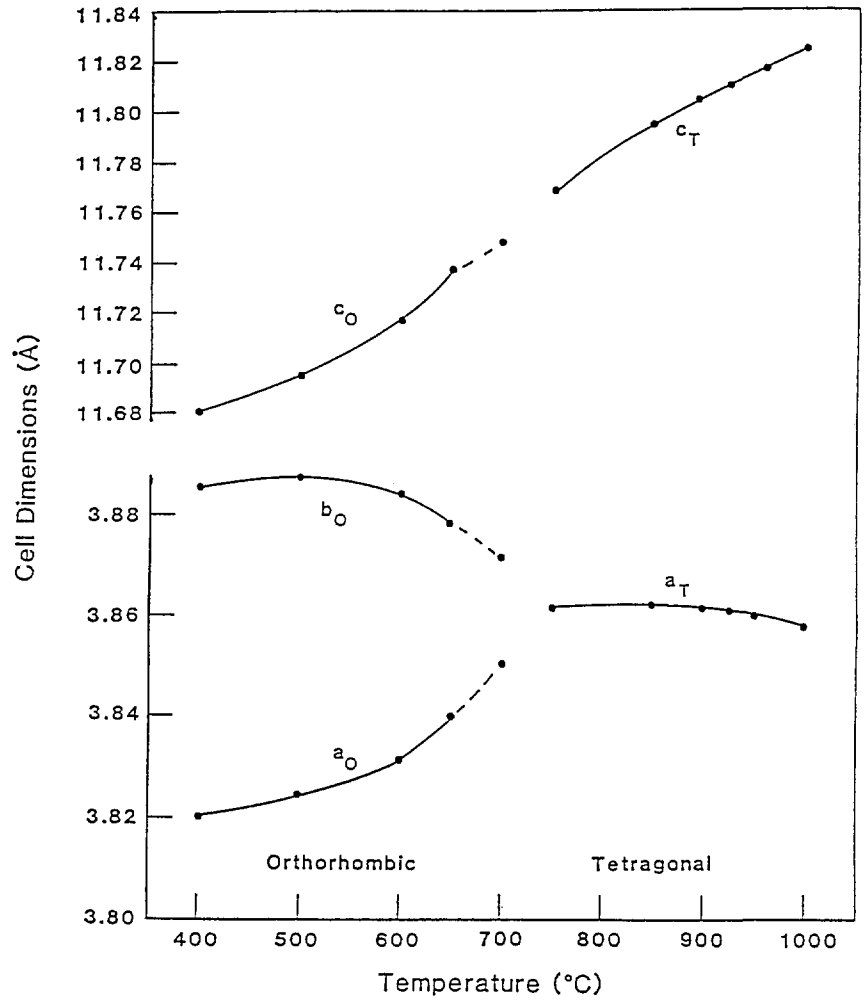

Figure 5. A plot of the cell dimensions of YBCO as a function of annealing temperature. As the temperature increases, the cell dimension b_0 decreases while a_0 increases [40].

second order, order-disorder type. TGA was also used to determine the oxygen diffusion coefficient of YBCO [44]. The oxygen was found to diffuse faster than in some insulating oxides, such as Al_2O_3, but slower than in oxides which have been classed as oxygen conductors. The diffusion constant plotted against $1/T$ is linear from 400-600 K. From 600-750 K, it is not linear and only weakly dependent on temperature, which may be due to structural phase changes.

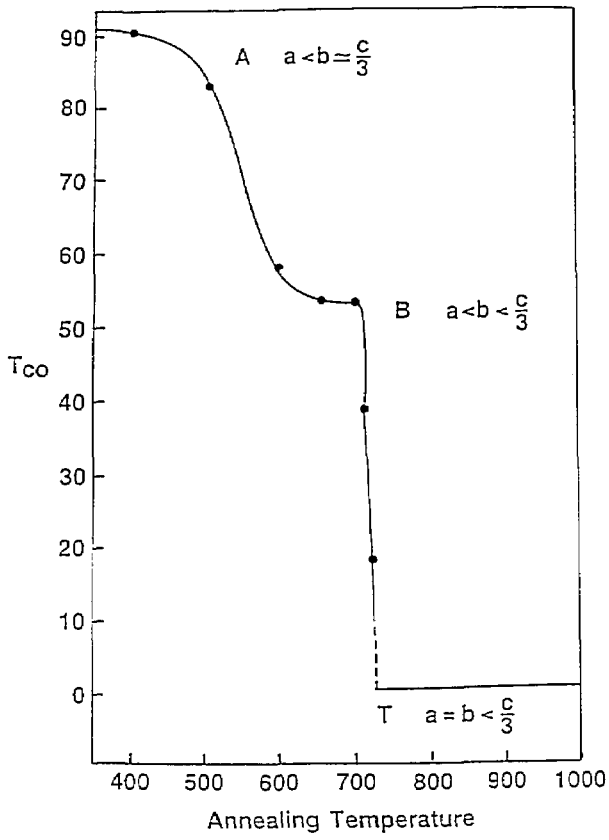

Figure 6. A plot of T_{co} versus annealing temperature. Note the two plateaus at 91 K and 58 K [41].

Structural phase transitions of $Ba_2RCu_3O_{6+y}$ (where R=Sm, Gd, or Er) were studied [45] to determine the effect of the span of radii and the magnetic properties of Gd and Er. Samples were annealed at 400-1000 °C and quenched in a liquid-nitrogen-cooled copper well. The x-ray spectra were similar to that of YBCO. The orthorhombic-tetragonal transition always occurred between 625-770 °C. The Gd compounds showed an increase in the *c* axis due to oxygen vacancies, as in YBCO. The rare-earth elements with smaller radii stabilized the orthorhombic phase to a higher temperature. The phase transformations are apparently second order and may involve two orthorhombic regions which correspond to two T_C plateaus—one at 92 K and one between 52 and 60 K. These regions have the same general structure, but different oxygen distributions corresponding to ordered and disordered modifications within the orthorhombic structure. No obvious plateau was detected for the Gd compounds however. TGA also identified plateaus—three apparently single-phase regions for Sm, Y, and Er and two for Gd. The fact that the literature T_C values are about the same for all the compounds suggests that the superconducting electrons are not strongly associated with the rare-earth elements [46].

The effect of annealing atmosphere (fig. 7) was also studied [47, 48]. Samples annealed and cooled in oxygen were found to have sharper superconducting transitions than those annealed and cooled in air. They also had sharper diffraction peaks. The broadening is due to crystallite size differences and microstrain/chemical inhomogeneity which can originate from twinning, anisotropic thermal expansion, and oxygen vacancies. Thermal analysis determined that the maximum oxygen content is obtained by annealing at 450 °C, or slightly above, and that the oxygen loss is reversible [43].

It is clear from these results that the processing parameters must be carefully controlled to yield the desired material. There is an additional concern. While it is known that exposure to water can destroy the superconducting ability of $YBa_2Cu_3O_7$ it also has been found that acetone can be deleterious [49]. To obtain dense, strong ceramics, the powders are often milled to a small size before sintering. When an acetone slurry is used, a non-superconducting tetragonal phase can be formed if the slurry is dried at 200 °C. The superconducting orthorhombic phase can be restored by annealing at 950 °C in O_2.

It may be possible to avoid the grinding steps altogether by employing chemical synthesis. Four systems—the coprecipitation of yttrium, barium, and copper hydroxy-carbonates; the hydrolysis of yttrium, barium, and copper alkoxides in ethanol/toluene; the reaction of barium and yttrium alkoxides with $Cu(OH)_2$; and the hydrolysis of yttrium, barium, and copper alkoxides in methoxyethanol/ethanol were studied [50]. All the systems showed $BaCO_3$, CuO, and Y_2O_3 when heated at 400-600 °C. The samples must then be heated to 800-950 °C to obtain $YBa_2Cu_3O_{7-x}$ and subsequently annealed in oxygen at 450-600 °C to obtain superconductivity.

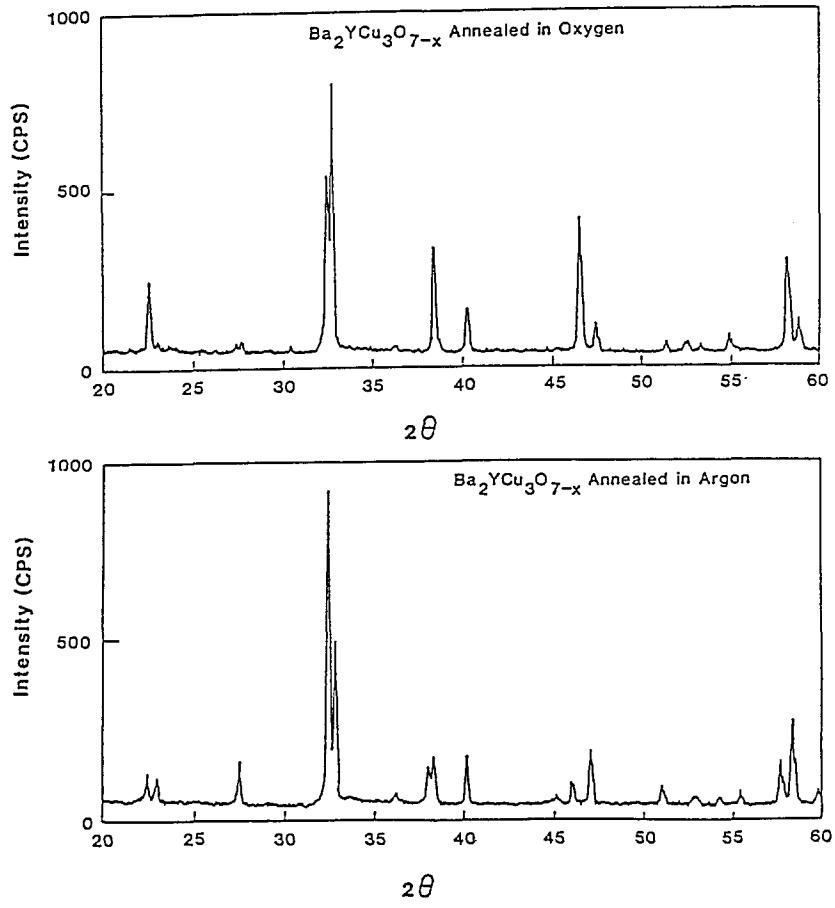

Figure 7. Effect of oxygen on the structure of YBCO. a) x-ray diffraction pattern of YBCO annealed in air (orthorhombic). b) x-ray diffraction pattern of YBCO annealed in argon (tetragonal). The most striking features are the intensity reversal of the two sets of doublets at around 32-33° and 57-60°, and the shifting of positions of corresponding peaks which indicates different cell dimensions [47].

The making of YBCO films was also investigated using two different techniques. In the first approach, films were made from a bulk superconductor by laser ablation [51], as shown in fig. 8. A pulsed-laser source was used to vaporize the surface of a disk made from superconducting YBCO and deposit a film on a fused silica substrate. Films were made by irradiating a spot or raster scanning. The resulting films were 1 cm^2 in area and thicker in the center, ~ 2 μm, than on the edges. The as-deposited films had superconducting regions with properties comparable to the bulk material. Similar results were obtained for La-Sr-Cu-O (LSCO). The potential advantage of this method is that the film does not need a high temperature anneal to incorporate oxygen. This is important in hybrid electronic (superconductor-semiconductor) applications where a heat treatment could destroy the semiconductor.

A second technique investigated for making YBCO films [52] utilized co-evaporation of Y, Cu, and BaF_2. These materials were deposited simultaneously onto a room-temperature substrate. Oxygen was introduced into the vacuum system during deposition. At this stage, films containing BaF_2 are tolerant to moisture, air, positive photoresist, developer, and common solvents. Annealing in oxygen and water vapor incorporated additional oxygen into the film and reacted away the fluorine. The choice of substrate is critical for many applications. The best films have been fabricated on $SrTiO_3$. A resistive transition, about 0.5 K wide, is shown in fig. 9.

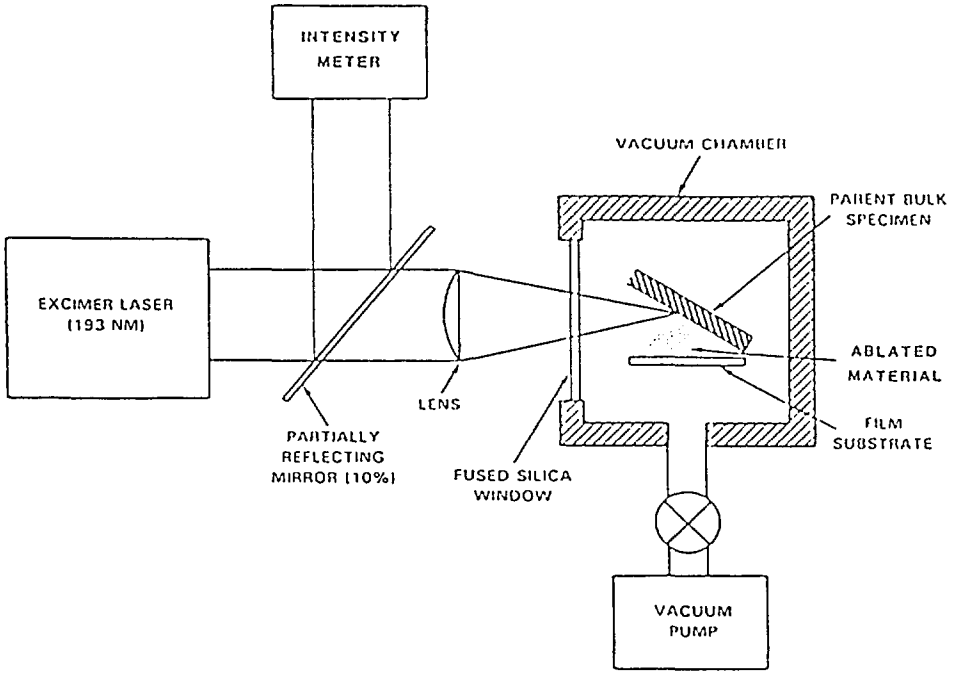

Figure 8. Schematic of laser-ablation process [141].

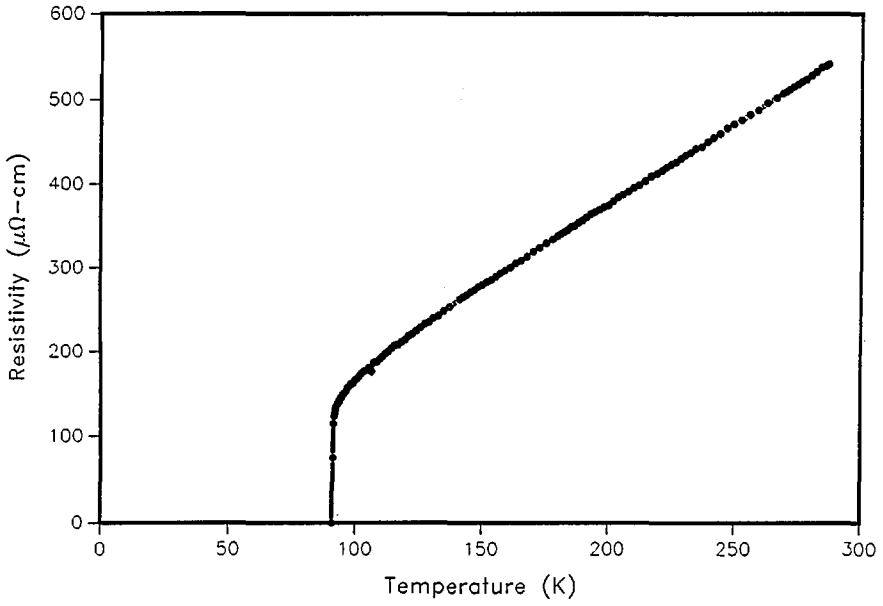

Figure 9. Resistive transition of YBCO film made by coevaporation of Y, Cu, and BaF_2 on a $SrTiO_3$ substrate [52].

Films deposited using the second method are patterned using conventional photolithographic processes [52]. Prior to deposition of the YBCO, the substrate is coated with photoresist, exposed with a pattern using a projection printer, and developed. The exposed and developed resist exposes bare substrate where the patterned YBCO is to remain. After the room temperature deposition of the Y, Cu, and BaF_2, but before the oxygen anneal, the remaining photoresist is dissolved, removing the unwanted portions of the film. Annealing in oxygen as before creates a patterned superconducting film.

Superconducting strips with dimensions as small as 1.5 μm have been successfully fabricated. A patterned film having a constriction of 5×5 μm had a critical current density of 5.6×10^6 A/cm^2 at 4 K. As mentioned earlier, such high critical current densities are not yet achievable in bulk samples. Patterned films of this sort are being used in fundamental studies of noise in small constrictions and as transition edge bolometers. Efforts to make high-T_C Josephson junctions are in progress.

6. Processing-Property Relationships

The understanding of the relationship between microstructure, processing, and properties is particularly important for the high-temperature superconductors. These are oxygen-sensitive, brittle materials whose processing parameters need to be controlled to produce optimum properties. The understanding of this relationship requires, in addition to the measurement of electrical conductivity, techniques such as x-ray diffraction, magnetic susceptibility, and ultrasonics. Neutron activation analysis can be used to determine the stoichiometry [53]. ac susceptibility measurements can be used to characterize the superconducting properties. The ac data consist of a real and an imaginary component. The real part can be used to determine T_C and to estimate the percentage of superconducting sample. There have been questions about the interpretation of the imaginary part. Goldfarb et al. [54] have provided evidence that the imaginary part is almost totally due to hysteresis losses and have shown how the temperature at which the slope of the imaginary component becomes positive upon warming can be used to estimate H_{C1}. To observe a sharp magnetic transition and complete bulk diamagnetism, the applied measuring field must be very small. As shown in figure 10, two distinct superconducting components in a single-phase specimen were identified [55]—one a relatively high T_C, H_{C1} superconductor and the other a relatively low T_C, H_{C1} superconductor (see fig. 11). These two components were found in all sintered high-temperature superconductors that were examined. The results of subsequent experiments on sintered and powdered samples suggested that the first component was intrinsic to the material, while the second arose from inter-granular coupling [56].

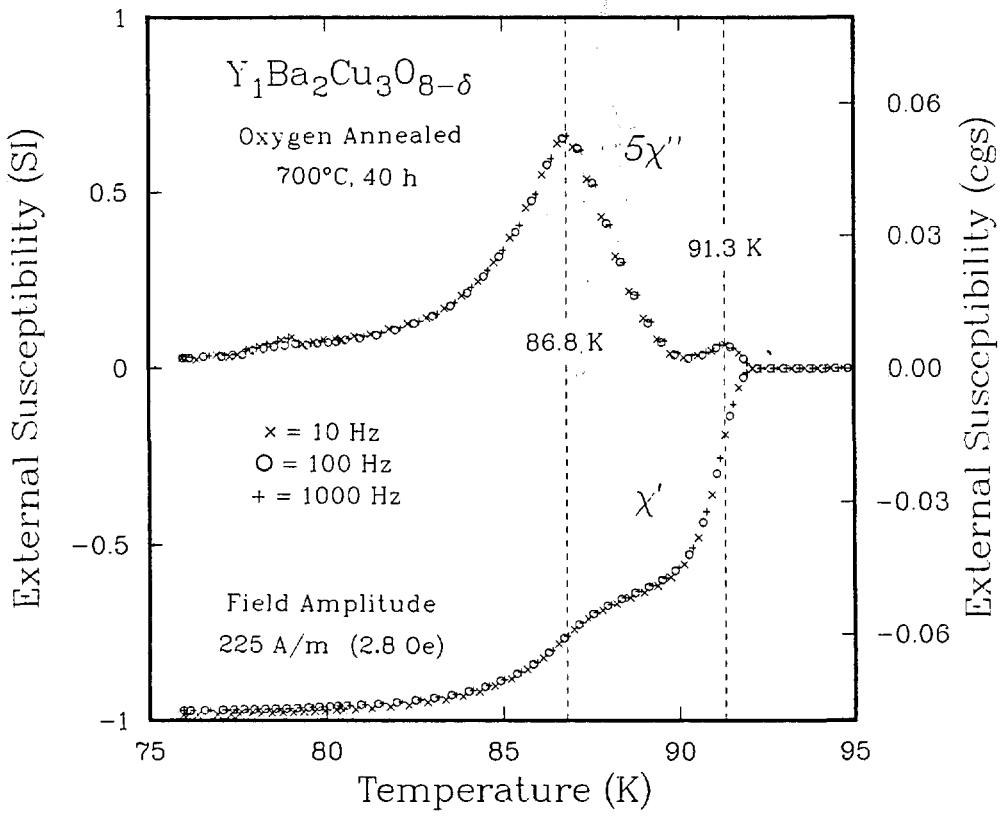

Figure 10. ac susceptibility vs temperature for YBCO. In the imaginary part, two peaks are apparent. Note that the susceptibility is almost independent of frequency [55].

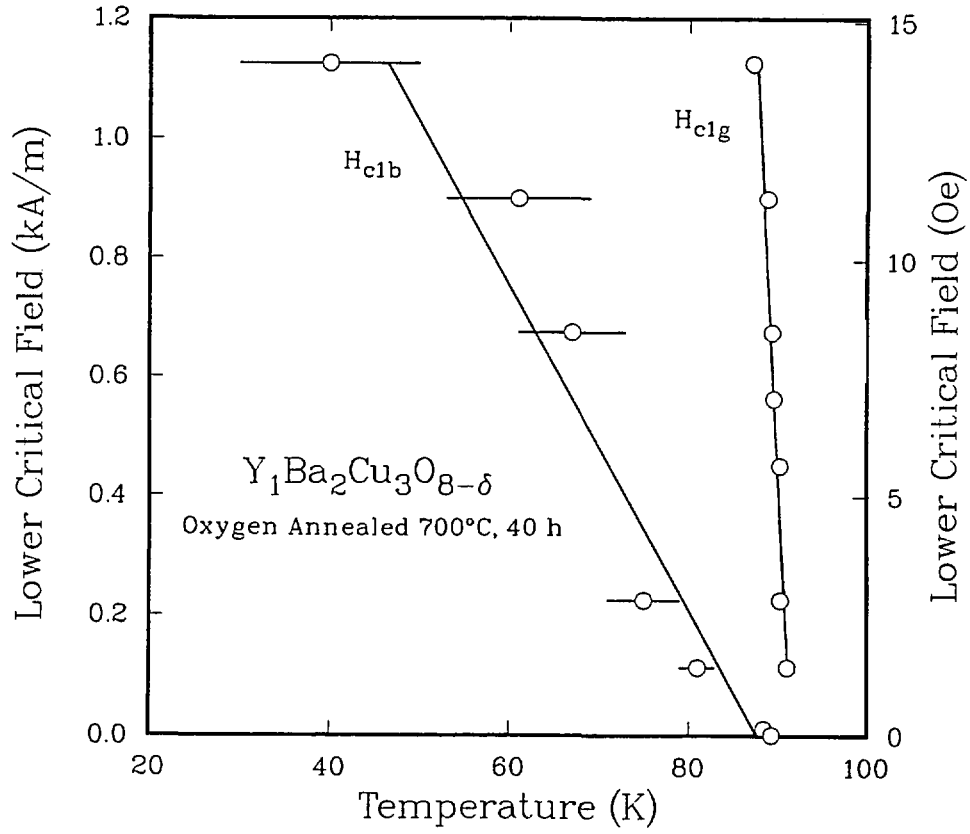

Figure 11. Lower critical fields vs temperature for the two components observed in figure 8. The g refers to the higher T_c component [55].

Since the superconducting properties of the new superconductors are strongly dependent on microstructure and composition, techniques available for elemental and molecular microanalysis, principally, electron-probe compositional mapping and micro-Raman spectroscopy were employed to investigate a variety of samples in the YBCO system. Electron-probe compositional mapping is computer-aided x-ray microanalysis furnishing spatially-resolved digital images in which the displayed grey scale is related to the true composition of the specimen and not merely to x-ray intensity of any given element. In studying YBCO, three wavelength dispersive spectrometers were employed; one each for the detection of yttrium, barium, and copper. A representative result is shown in figure 12. Compositional mapping is most useful, therefore, in the identification of compositional heterogeneities on the micrometer-scale, and the determination of dissimilar phases in a high-temperature superconductor [57-59].

Raman and infrared spectroscopy are widely used tools for investigating and characterizing high-T_C superconductors. The Raman spectra exhibit vibrational modes mostly related to Cu-O bonds and to vibrations of other atoms in the lattice. The spectra are sensitive to differences in crystal structure, bonding, and phase relationship and, furthermore, show a variation with oxygen content, thus providing information on oxygen stoichiometry. Micro-Raman spectroscopy extends these capabilities into the microscopic domain with a spatial resolution comparable to that of electron-probe microanalysis. Preliminary work [60] has shown that this technique can provide molecular information not revealed by macro or average structure methods. A micro-Raman spectrum of the YBCO superconducting ceramic in the orthorhombic phase is shown in figure 13. Any variations in the frequency positions and relative intensities of the bands observed in these spectra are indicative of compositional and structural differences attesting to sample heterogeneities.

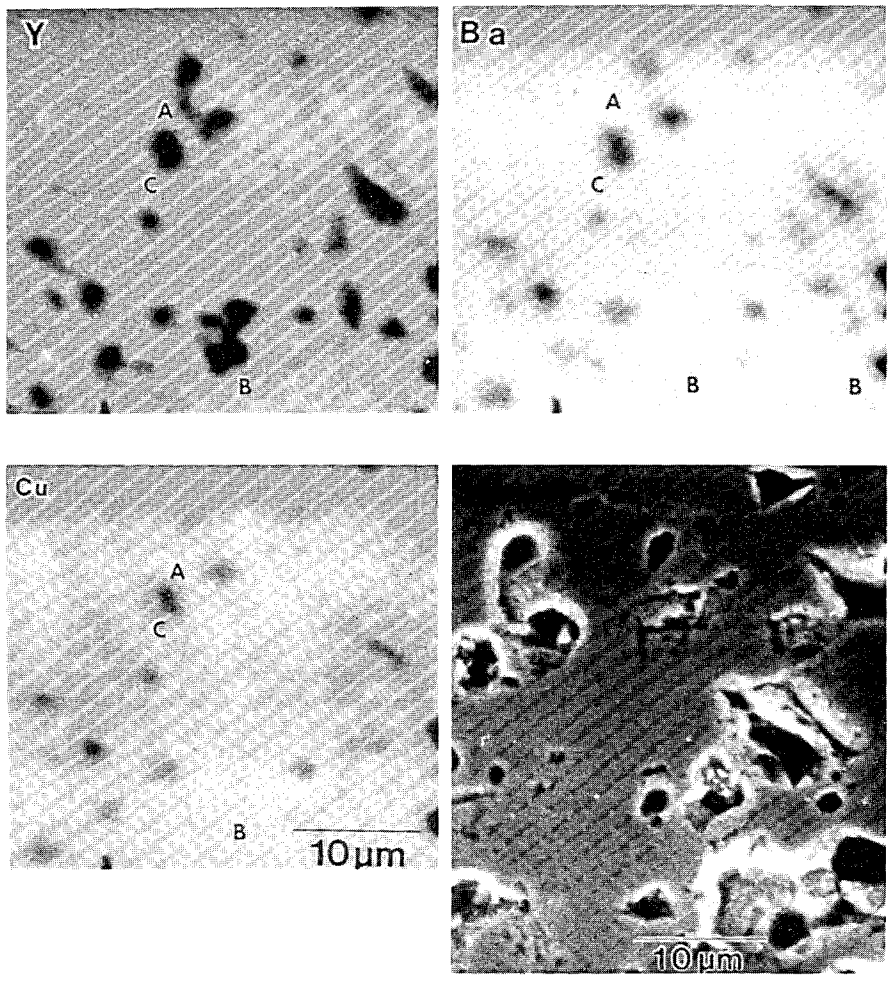

Figure 12. Electron-microprobe compositional maps for Y, Ba, and Cu and corresponding SEM image of YBCO sample. Region A shows a decrease in yttrium concentration, but no copper or barium enhancement; B shows an yttrium-poor region corresponding to a barium-rich but unchanged copper region; C shows an enhancement of barium with no changes in copper or yttrium concentrations [58].

Lattice defects in YBCO can be identified by field-ion microscopy (FIM). This technique permits the qualitative determination of surface and bulk atomic configurations and microstructural features. Atomic striations observed in FIM images are possibly due to preferentially conducting layers in the material. Thus the superconductivity is possibly localized to specific layers, which are tentatively identified as the Cu-O planes of the orthorhombic unit cell. FIM identified various lattice defects such as dislocations and grain boundaries in the superconductors $YbBa_2Cu_3O_{7-x}$, $SmBa_2Cu_3O_{7-x}$, $GdBa_2(Cu_{.96}Fe_{.04})_3O_{7-x}$, and $GdBa_2(Cu_{.92}Fe_{.08})O_{7-x}$ $(0<\times<.5)$, in addition to YBCO [61-64].

A new technique has been developed to observe the superconducting transitions—magnetic-field-modulated microwave absorption (MAMMA) detection [51, 65]—which differs from conventional microwave techniques in that it observes only magnetic-field induced changes in the sample's microwave loss as a function of temperature. The technique is accomplished in a conventional ESR spectrometer by applying a small ac magnetic field to the sample and phase detecting the microwave power reflected from the cavity at the ac modulation frequency. It has the advantages of ease of implementation using commercial ESR apparatus: high sensitivity due to noise reduction by narrow-band amplification and phase-sensitive detection,

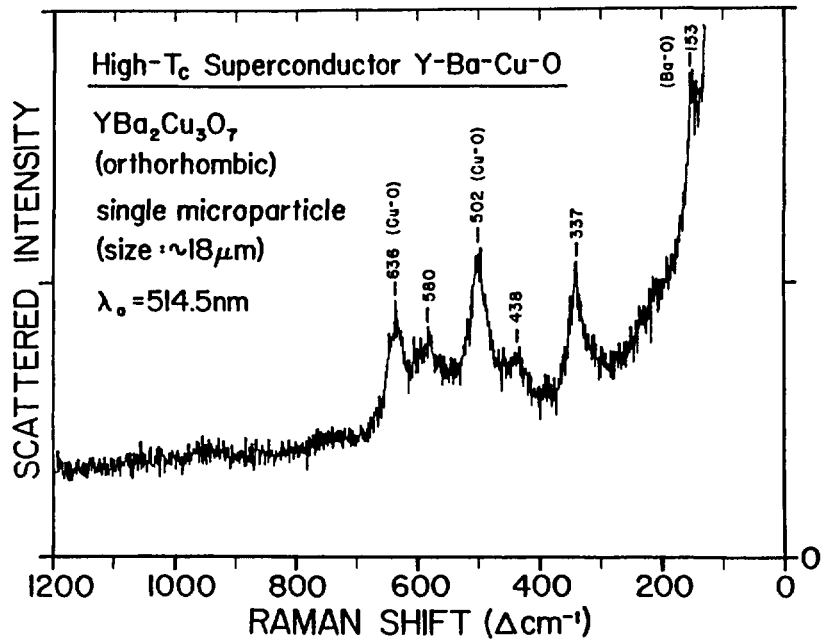

Figure 13. Micro-Raman spectrum of an arbitrary isolated particle of the superconductor $YBa_2Cu_3O_{7-x}$ ($x \approx 0$) identified to be in the orthorhombic phase. The spectrum is excited with the 514.5 nm line of an argon/krypton ion laser at low irradiance, employing 5 mW in a ~12 μm beam spot. The microparticle is supported by a lithium fluoride substrate. The resolution is 7 cm^{-1} [60].

and selectivity since only changes in sensitivity which are magnetic field dependent will be observed. The latter is characteristic of a superconductive transition, as illustrated in figure 14a. This MAMMA technique has been used to study bulk and film specimens of lanthanum, yttrium, and bismuth high-temperature superconductors (fig. 14b). These films were prepared from oxide targets by laser ablation [51].

The composition and microstructure of YBCO was studied as a function of processing [45]. Strontium was found to be the major contaminant. The starting compositions were barium rich relative to the Y:B:Cu ratio, which remained constant during processing. Electron-probe microanalysis revealed three types of inhomogeneities that are within regions which correspond to the YBCO composition—(i) Ba-rich; Y, Cu-poor, (ii) Y-rich, Ba-poor, and (iii) Cu-rich with lesser amounts of Ba and Y. These phases have been identified as (i) $BaCu_2O_4$, (ii) BaY_2CuO_3, and (iii) the remnants of a liquid phase that is present at the sintering temperature. The liquid phase limits J_C since the intergranular phases are not superconducting. Another source of insulating grain boundary film is carbon, which may arise from atmospheric CO_2 and from solvents used during grinding. During low-temperature oxidation of the sintered material, residual carbon may react with oxygen to form gas-filled pores along the grain boundary and a high concentration of defects adjacent to the grain boundary. Hence, it is apparent that a large degree of compositional control is needed to control the properties of YBCO.

Processing-property relationships for YBCO have been studied as a function of annealing temperature and environment. It was found [57, 58, 66] that annealing at low temperature in oxygen is necessary to obtain the highest T_C, sharpest transition, and the largest superconducting fraction. Samples contained a small amount of inhomogeneous second phase liquid, insufficient to prevent current flow. Sintering was more rapid and to a higher density in air than in oxygen. Segregation occurred during sintering and pores and micro-cracks were observed. The thermal expansion was very high for a ceramic—indicating that thermal shock may be a problem for these materials. Fracture toughness was quite low and the material was susceptible to moisture-enhanced cracking.

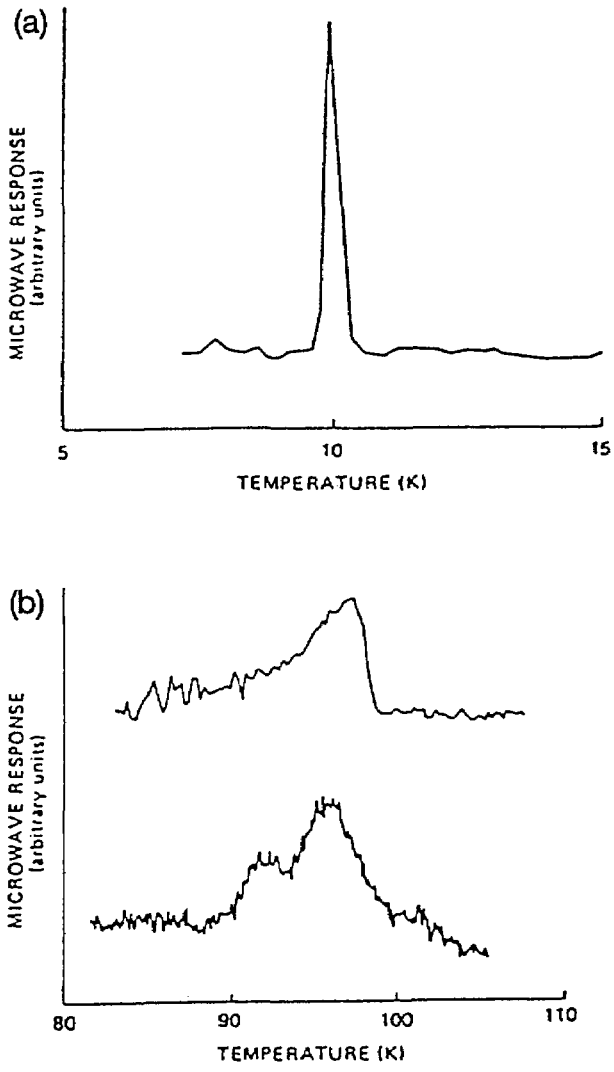

Figure 14. a) Microwave (MAMMA) signal vs temperature for a bulk sample of niobium. The T_c obtained was in good agreement with known values of T_c for niobium. b) Microwave (MAMMA) signal vs temperature for bulk YBCO (above) and thin film (below) made by laser ablation from the bulk. The value of T_c=95 K is in good agreement with resistivity and Meissner data. The double peak for the thin film is indicative of two phases with slightly different T_c's [51].

Sintering at 950 °C gave the best density but poorest superconductivity due to a lack of porosity required for oxygen diffusion. Sinter-forging was investigated [66] reasoning that it should be possible to increase the current density by aligning the grains. The grains had a high density center with the edges cracked and not very dense. Large yttrium-rich bands were formed perpendicular to the stress direction as a result of local segregation. The apparatus is shown in figure 15. The *c* axis tended to be aligned parallel to the applied stress direction. The transport J_C was less than 100 A/cm^2, however, and in some cases even zero. This was due to weak linking. Transmission electron microscopy showed second phases at grain boundaries, forming S-N-S junctions [67].

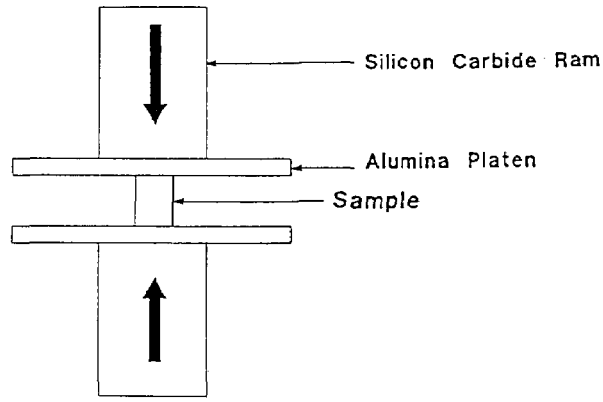

Figure 15. Sinter-forging apparatus. The load was applied in the vertical direction with no die wall constraints. The sample was separated from the ram by alumina plates [67].

Another possible method to align the grains would be to cast the samples in a magnetic field. The alignment is due to anisotropy of the paramagnetic susceptibility of the grains. Ostertag et al. [68] studied the magnetic casting of YBCO and HBCO (H=holmium). A slurry of the superconducting powder and isopropanol was placed in a homogeneous magnetic field of 2 T for 30 minutes (see fig. 16). The samples, which were then pressed and sintered, tended to align with their *c* axes parallel to the applied field ([001] alignment). However, this alignment is not sufficient for high J_C. Alignment in the [010] and [100] or [010] is also needed since tilt decreases J_C. Clean grain boundaries are also a requirement. Current densities of samples aligned in the oxygen-rich state were up to five times greater than samples aligned in an oxygen-deficient state and then oxygenated, due to the presence of non-superconducting junctions. Bulk J_C calculated from magnetic measurements were 10^3-10^4 A/cm^2.

7. Electrical Contacts

One problem that existed in the study of high-temperature superconductors was too high a resistivity in the electrical contacts. Contacts made of indium solder, silver paint or epoxy, direct wire

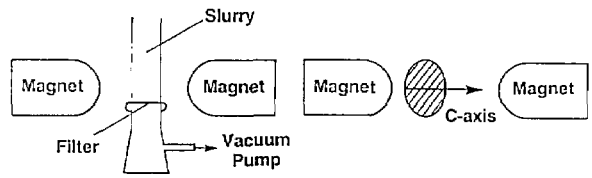

Figure 16. *Configuration for casting in a magnetic field.* The slurry of isoproponal and powder was placed in a homogeneous 2 T magnetic field [68].

bonds, and pressure contacts have contact surface resistivities in the range of 10^{-2} to 10 Ω-cm^2 which is several orders of magnitude too high for measurement and applications. Contact resistivities of 10^{-4} to 10^{-5} Ω-cm^2 or lower are needed. Ekin and coworkers [69-71] developed a method consisting of sputter etching the surface of the superconductor to remove the degraded surface area immediately before depositing noble metal (Ag or Au) pads, followed by annealing the noble metal/superconductor interface in oxygen. Contact resistance for the silver pads showed metallic behavior, decreasing by a factor of 3 to 12 as the temperature decreased from 295 to 76 K. Contact surface resistivities less than 10 μΩ cm^2 at 76 K were achieved without oxygen annealing. After annealing in oxygen at 500 °C for 1 hour, contact resistivities were reduced to as low as 0.1 nΩ cm^2 [70]. The low oxygen affinity of the noble metals may play an important role in passivating the contact interface. On the other hand, oxygen and indium formed a semiconducting oxide with resistivities greater than that of pure indium [70, 72]. Room-temperature diffusion of oxygen is limited in the noble metals, thus protecting the YBCO. This may explain why there can be low contact resistance despite exposure of the YBCO to air.

Moreland and Goodrich [73] have developed silver screen contacts for rapid characterization of YBCO. The screens can be used for making voltage contacts and voltage taps. Silver wire screens are interleaved between calcined powder sections and fixed to form a composite pellet. Silver diffuses in the powder during sintering to form proximity contacts permeable to oxygen.

8. Electronic Structure

One method of obtaining information on the electronic structure of superconductors is by tunneling measurements. A technique used for such measurements was developed by Moreland and Ekin [74]—the break-junction technique (fig. 17). In a break junction, tunneling occurs across the fracture of a bulk sample. A small piece of a bulk material is mechanically fractured under liquid helium and the freshly fractured surfaces are adjusted to form a tunneling barrier with helium as the insulator. The sample can be a single crystal, polycrystal, or sintered pellet. Unlike other tunneling techniques, break junctions give information on the interior of bulk samples. Break junctions have been used to study both the lanthanum and yttrium superconductors. Tunneling junctions for LSCO (fig. 18) exhibited a variety of tunneling behavior [75-77]. Scanning-electron microscopy showed a rough surface with numerous voids and scattered

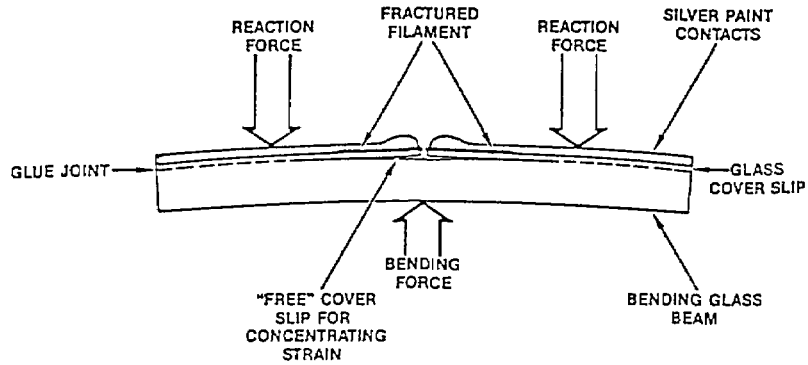

Figure 17. Fabricating a break junction. A superconducting filament is mounted on a beam which is bent using an electromagnetic force. Once the filament is fractured, the beam is relaxed to form a tunneling contact within the fracture of the filament. Contact may be either through a thin insulating medium (vacuum, gas or liquid) or by closing the fracture to form a point contact. An electromagnetic assembly affords precise control of the tunneling gap [84].

inclusions. This variability may be due to tunneling between different phases in the material. Large energy gaps and deep structure in the conductance derivatives are evidence for a strong coupling mechanism.

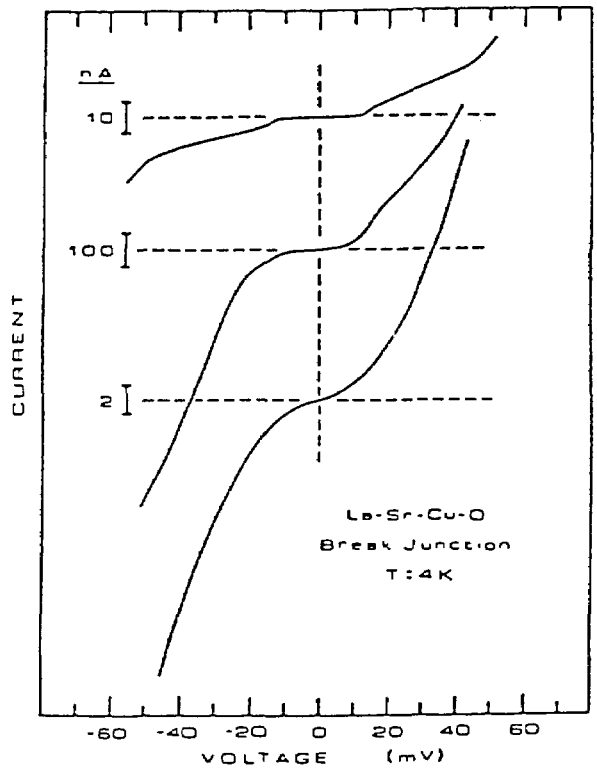

Figure 18. Voltage vs current curves for a LSCO electron tunneling break junction immersed in liquid helium at 4 K for three different barrier settings. The bottom curve was the most common V-I characteristic found [75].

Break junctions for YBCO gave results indicative of strongly coupled superconductors [78] but had the same variability as LSCO. Variable results in perovskites can be explained as being due to the structure which consists of alternating layers of insulating and conducting platelets which can be superconducting, semiconducting, or both [77]. While evidence for the usual pairing state associated with the BCS theory was found, so was a lower $I_C R$ product which is indicative of a lower energy gap than that expected from BCS theory. In addition, a Josephson junction effect was found [79]. Evidence of an intrinsic energy gap was found in both LSCO and YBCO [80]. The gap scales with T_C and decreases and vanishes when approaching T_C from a lower temperature. This points to the energy gap being quasiparticle in nature.

Break junctions in single crystals should permit a direct measurement of gap anisotropy if the samples are fractured along cleavage planes. To this end, break junctions of single crystal $HoBa_2Cu_3O_x$ (HBCO) were compared with polycrystalline YBCO [81]. Both had junction conductance increasing linearly with junction bias. Gap structure of YBCO occurred more often during adjustment of the junctions than with HBCO. This may have been due to a lack of oxygen penetration in the single crystal. The results may have been affected by the fact that the HBCO fracture surfaces were not ideal. The V-I curves showed the square-law dependence of current seen in many tunneling measurements of polycrystalline YBCO.

Based on the fact that the anomalies in the break junction results may be microstructural in origin and not due to the electron coupling mechanisms, several models have been proposed. In the granular model [82], the superconductor is divided into grains isolated from each other by insulating tunneling junctions. A second model, the multiparticle model [83], assumes that the grains are oriented to form a series array of junctions near a primary tunneling contact. Moreland et al. have developed a third model to explain these results in perovskites [84]. In the laminar model, the microstructure consists of a complex tunneling matrix with parallel superconducting laminae connected to each other, the point contact, and the surrounding grains by tunneling junctions. This structure may be manifested in a layered perovskite single grain with superconducting layers separated by high dielectric insulating barriers. The individual laminae form a series-parallel network of superconducting junctions within a single grain of the material. Although there is some evidence that casts doubt upon the granular model, the exact model is still in question.

Tunneling measurements were also made on YBCO thin films [85] using the method of squeezable electron tunneling (SET) junctions developed by Moreland et al. [86]. In contrast to the break junction measurements of bulk samples where the spectra are often without energy gap features, SET spectra invariably contain such features. This implies that the film is superconducting near the surface, in contrast to results on bulk materials which indicate that only parts of the interior are superconducting. Improvement of surfaces by the addition of very thin noble metal films, which become superconducting by the proximity effect, is under investigation [87].

Measurement of the electronic structures of the high-temperature superconductors are important in providing supporting evidence for theoretical models of superconductivity. Kurtz [88] has written a review of the experimental measurements of the valence electronic structure of LSCO and YBCO. NIST's Synchrotron Ultraviolet Radiation Facility (SURF-II) was used to study these features. The electron structure of YBCO was measured using resonant photoemission, which is associated with the enhancement of valence photoelectron features resulting from the coupling of excitation and decay mechanisms at the core-electron photoabsorption onsets. Radiation in the 60-160 eV range was used [89], (fig. 19). The upper edge of the valence band was found to nearly coincide with the Fermi level and the density of states was small. There was no distinctive edge. The valence band did not resonate with the photon energy. Furthermore, there was no evidence of valence band structural changes as the temperature was lowered below the critical temperature. The copper oxide in the material was found to give spectra similar to CuO.

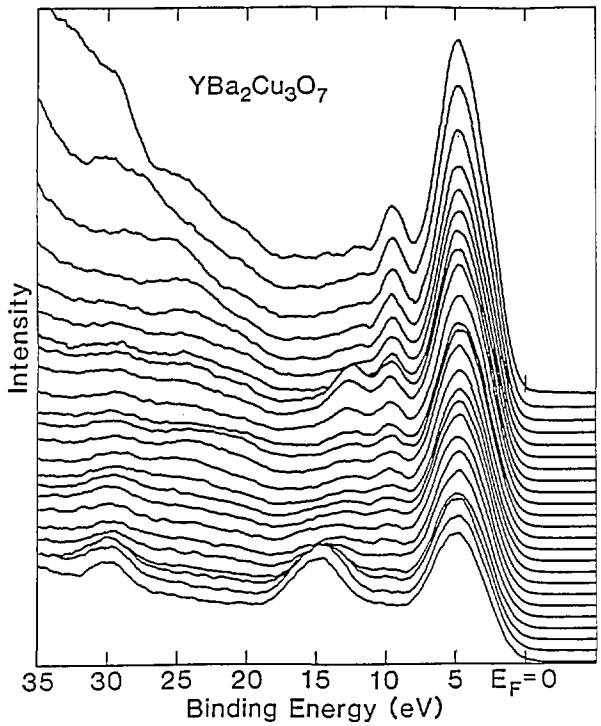

Figure 19. Ultraviolet photoemission spectra of fractured YBCO. The top curve is at h=60 eV, the bottom 106 eV, and each curve is separated by 2 eV. At 60 eV there are two valence band features—at binding energies of 5 and 9.4 eV. Increasing the photon energy, features become apparent at 12.4, 15.0, and 28.8 eV. The features at 9.4 eV are due to Y/Cu; at 12.4 eV to Cu, and at 15.0 and 28.8 eV, Ba [89].

Another study using SURF-II but at an energy range of 20-600 eV [90], confirmed the 2^+ valency of copper in YBCO. The National Synchrotron Light Source at Brookhaven was used to provide information on oxygen, barium, and yttrium. It was found that the p-type partial density of states is very small at the Fermi energy. The electronic structure observed in the photoemission measurements is associated with the oxygen $2p$ orbitals. This study also observed no change in the spectra as the temperature was lowered below the critical temperature.

Additional studies carried out by Kurtz, Stockbauer, and coworkers included photoemission of YBCO and LSCO, which revealed a resonance in the peak located at a binding energy of ~9.5 eV for photon energies spanning the onset of O–2s excitations. This feature is associated with oxygen excitations. The satellite is suppressed on surfaces that are superconducting within the probe depth of the spectroscopy [91]. Photoelectron spectroscopy of high-T_C superconductors, including the newer bismuth and thallium superconductors revealed that the materials have a highly hybridized Cu-O valence band and resonant satellites which imply that the materials are highly connected. No substantial changes were observed in the electronic structure as the materials were cooled from room temperature to below T_C. The materials reacted strongly with H_2O and CO_2, forming hydroxides and carbonates, but reacted more weakly with O_2 and CO [92, 93].

Photoemission measurements of YBCO revealed two constraints on any theoretical treatments of its electronic structure based on the observation of a 2.3 eV feature [94]. First, YBCO has a higher charge carrier concentration at the Fermi level than in related lower-T_C and non-superconducting compounds. Secondly, there is a large contribution from oxygen to the density of states near the Fermi level, mainly derived from oxygen in the Cu-O chains. The 2.3 eV feature is intense in the orthorhombic phase, but weak in the tetragonal.

9. Physical Properties

Current densities are a critical parameter for the successful application of high-temperature superconductors. A cryogenic bathysphere developed by Moreland et al. [95,96] for resistance measurements of high-T_C superconductors is shown in figure 20. This device thermally isolates an environmental chamber from surrounding cryogenic

fluids. The bathysphere has the advantages of (i) being compact enough to fit in the base of a high-field superconducting solenoid without the use of a re-entrant dewar; (ii) the sample remaining dry; (iii) being inexpensive; (iv) having no moving parts; and (v) having sufficient thermal contact between sample and thermometer provided by the ambient pressure exchange gas to maintain thermal equilibrium within ± 0.1 K while the temperature changes as fast as 3 K/min. It may also be possible to adapt this device to susceptibility, critical current, and electron tunneling measurements. The bathysphere has been successfully tested with NbTi in liquid helium and YBCO in liquid nitrogen.

As previously mentioned, current densities of the order of one million A/cm^2 will be required for most applications. While films with these current densities have been produced, bulk materials have had much lower current densities. Ekin et al. [97, 98] studied bulk sintered YBCO samples from several different laboratories. Using V-I characteristics, they found that while a field of over 30 T was needed to suppress all superconductivity, a field of only a few tesla could suppress the transport current (fig. 21). The measured transport current was significantly lower than that measured by magnetization. The superconducting transition in polycrystalline YBCO is very broad. This is consistent with a model of a weak-link region between high-current-density grains. At least part of the behavior is due to intrinsic conduction anisotropy. This anisotropy has been observed in YBCO single crystals with the weakest conduction along the c axis [99]. The low current density could be due to: (i) impurities or low-T_C phases at the grain boundaries or (ii) misalignment of the grains. Electron microscopy gives no evidence of the former [100]. The location of the weak links in YBCO could be at the grain boundaries, within the grains or between the Cu-O planes. Transport critical current densities have been measured at low magnetic fields in several kinds of high-T_C superconductors fabricated in many different laboratories, and fitted with a model which assumes that the barriers to current flow are Josephson weak links which have a statistical distribution of sizes and orientations [101-103]. The data were shown to follow the Airy current-field pattern. The fits of the data to theory are good for all the samples. The fitting parameter essentially gives the average dimension of the junctions, which in all instances is about equal to the grain size, thus furnishing convincing evidence that the barriers at low magnetic fields are at the grain boundaries. This finding indicates that a possible method for increasing the current density would be by processing in such a manner that the grains would be aligned.

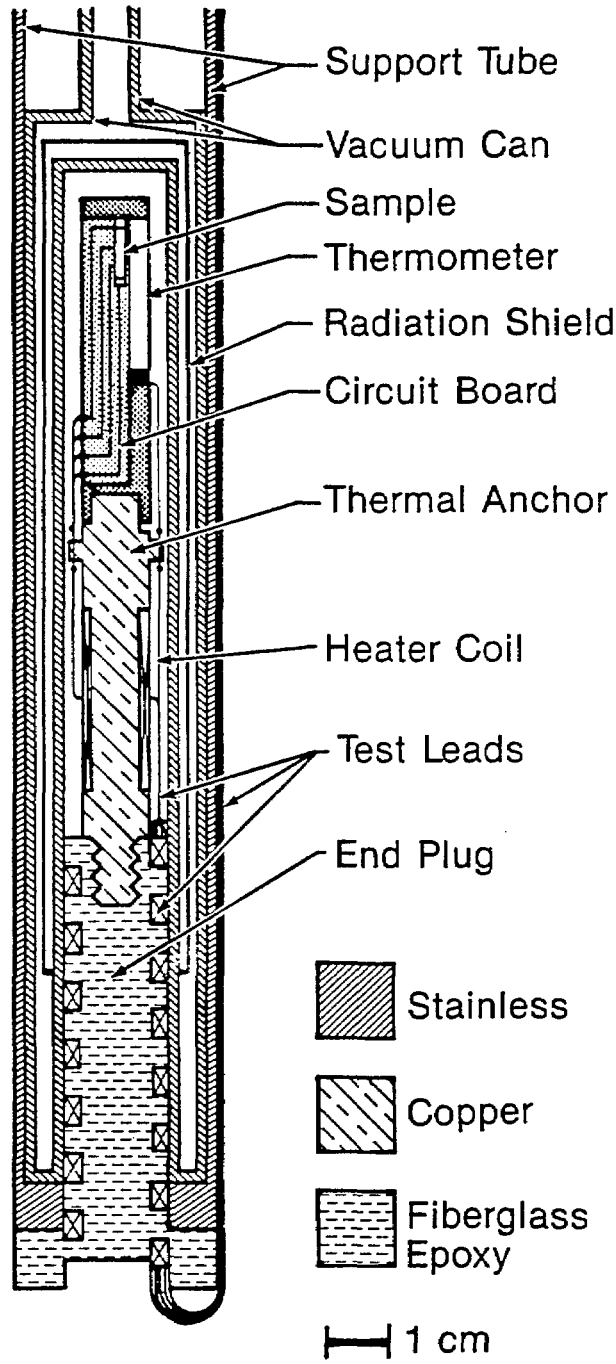

Figure 20. Cryogenic bathysphere for resistance measurements of high-T_c superconductors [95, 96].

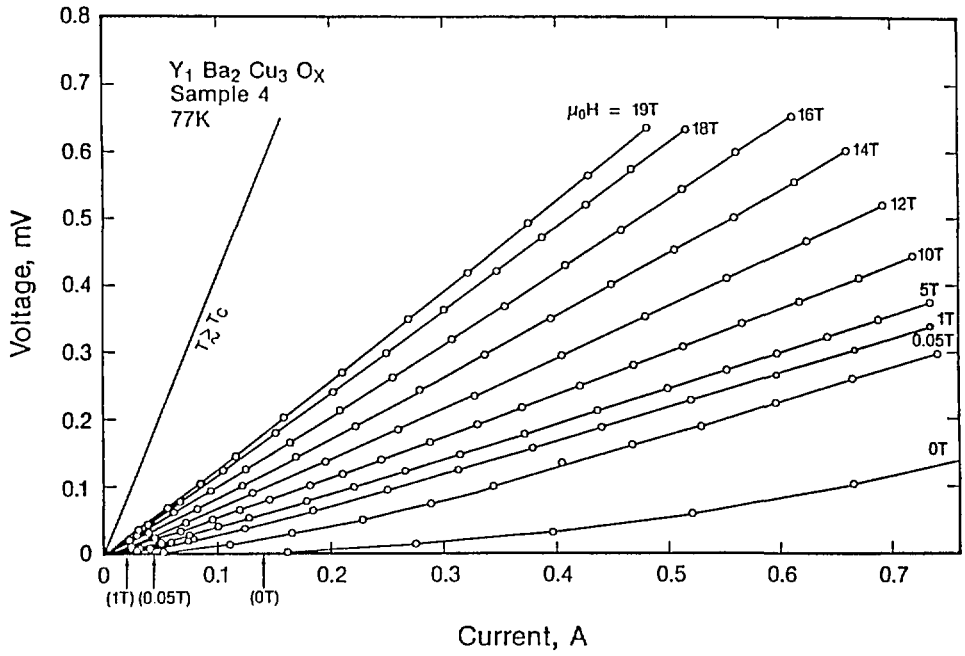

Figure 21. Voltage vs current characteristics for a YBCO sample in transverse magnetic fields in liquid nitrogen at 77 K. High magnetic fields were required to increase the slope to the normal resistance value at T_c, and the transport critical current is suppressed by very low fields. The curves are nearly linear at currents well above the critical currents indicated by the arrows [100].

Other physical properties of interest include the elastic constants, which have practical significance, such as in stress and fracture toughness, and are related to physical properties such as specific heat and hardness. Elastic constants relate strongly to interatomic potentials and force constants and can be used to calculate the Debye temperature which is used in the BCS calculation of the critical temperature. They also relate strongly to any phonon-mediated superconductivity mechanism. Values of elastic constants can be determined by ultrasonic methods and one of them, the bulk modulus, by x-ray diffraction. The elastic properties of metal-oxide superconductors have been reviewed by Ledbetter [104].

Ledbetter and coworkers have measured the elastic constants of YBCO using ultrasonic techniques. YBCO was compared to $BaTiO_3$ [105] and was found to have a lower elastic stiffness which could arise from oxygen vacancies or microcracks. The latter have a larger effect than a comparable fraction of spherical voids. Study of six YBCO specimens [106] showed that some specimens may be free from softening defects and their properties may reflect intrinsic behavior. A check on this is to compare elastic and thermal Debye characteristic temperatures. Elastic constants were measured as the specimens were cooled through the transition temperature [107-110]. Samples run in helium gave reproducible results suggesting that these measurements represented intrinsic material properties. Elastic constants showed irregularities above and below, but not at, the critical temperature. The shear-modulus results (fig. 22) departed from those expected for a simple second-order normal/superconducting transition, in agreement with the results for the dilation [111]. The value of the Poisson ratio behaved irregularly below the transition temperature indicating a change in interatomic forces supporting Geballe's view [87, 112] that a large fraction of electrons enter into Cooper pairs, the gap is approximately equal to the Fermi energy, and coupling is strong. During cooling from 160-70 K, YBCO behaved as if it underwent a sluggish phase transition. Two YBCO materials with different oxygen contents, $x=6.70$ and 6.92, showed similar ambient-temperature elastic-constant values, and similar temperature behavior [113], but the $x=6.92$ YBCO demonstrated a higher elastic stiffening during cooling to 4 K.

The behavior of the elastic constants can be described by a "reentrant softening" model [114, 115]. Softening occurs just above the critical temperature suggesting growing lattice instability with decreasing temperature. Premonitory behavior of this type is known to be associated with martensitic

or displacive structural transformations in various materials including the A15 superconductors [116]. The increased stiffness below the transition temperature is the result of the softening being offset by the increased stiffness associated with the developing superconducting phase. The calculation of the Debye temperature based on this model is in agreement with other experimental measurements. The model also predicts that the elastic constants will have a higher value in the normal state than in the superconducting state. The results of measurements on LSCO are also in agreement with this model. Strong thermal hysteresis, especially in the dilational modes, were found in subsequent studies by Ledbetter and Kim [117].

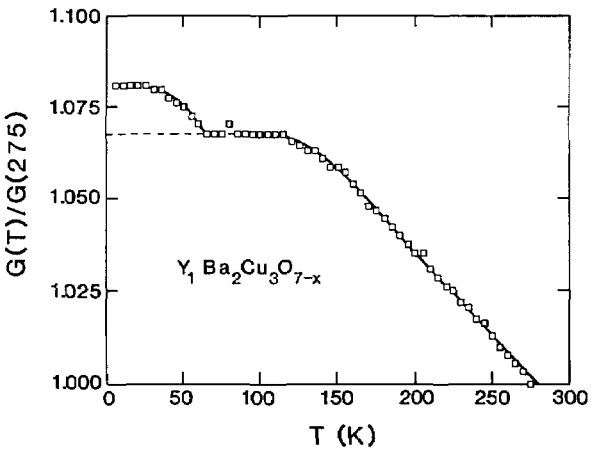

Figure 22. Relative shear modulus $G=\rho v_t^2$ between 275 and 4 K for YBCO. Above T_c (65 K for this material), behavior is normal. Below T_c, contrary to expectation, G apparently increases. However, a reentrant-softening model reconciles this apparent anomaly [107].

The bulk modulus of YBCO was determined by measurements in a diamond-anvil cell using an energy dispersive x-ray diffraction technique [118]. The least compression was observed within the perovskite layers because of the oxygen packing, and the largest was observed perpendicular to these layers. As seen in figure 23, the decrease in volume was essentially linear with applied pressure. The value of the bulk modulus was larger than that determined by ultrasonic techniques. Ledbetter and Lei [119] focused on this difference and its implication for the related Grüneisen parameter, supporting their measurements by ionic-bonding calculations.

Ultrasonics can also be used to provide additional information [120]. The ultrasonic velocity in YBCO was found to be different on warming than on cooling, with the greatest difference occurring in the first cycle. Three attenuation peaks were found on warming: I at 65-75 K, II at 134 K and III at 183 K. The hysteretic velocity changes and peak I appear related to a first-order phase transition involving magnetic superstructure in nonsuperconducting portions of the sample. Peak III appears to be consistent with a defect relaxation process. The origin of peak II, which was dependent on thermal history, could not be identified.

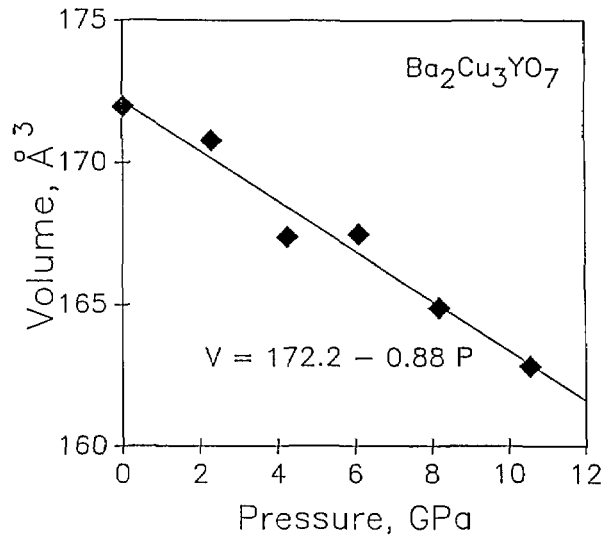

Figure 23. The pressure dependence of the volume of YBCO. The lattice parameters are determined from x-ray diffraction data. These data are used to calculate the isothermal bulk modulus [118].

Neutron inelastic scattering was used to measure the phonon density of states in an attempt to ascertain if any significant perturbations occurred in the phonon modes at the superconducting transition temperature [21]. A "softening" of such modes is a key aspect of conventional phonon-driven superconductivity. The normalized density of states at 120 K for $YBa_2Cu_3O_7$ is shown in figure 24. The spectra consist of a strong double peak near 20 meV and a second principal maximum at approximately 70 meV. Measurements below the transition temperature gave only negligible changes in the observed spectra which could be accounted for by anharmomic effects, and did not indicate any major changes in the overall phonon modes accompanying the superconducting transition. Oxygen-deficient $YBa_2Cu_3O_{7-x}$ showed a pronounced weakening of the 70 meV features in the density of states and a filling in and broadening of the lower

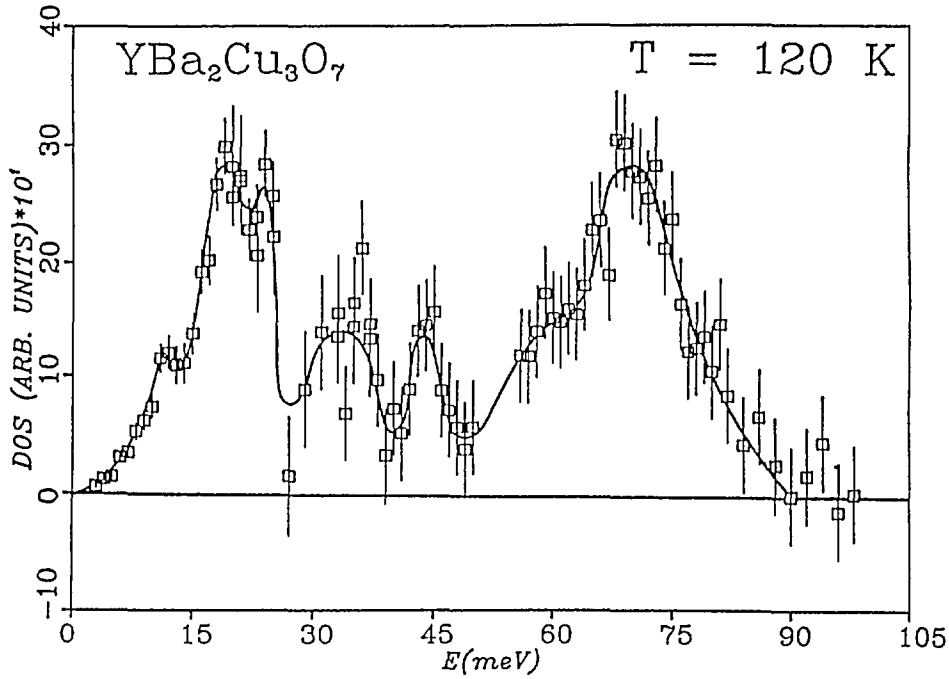

Figure 24. Vibrational density of states as measured with inelastic neutron scattering at 120 K. The largest spectral weight is contained in peaks involving oxygen vibrations [21].

energy features, reflecting a change in the harmonic modes associated with the absence of oxygen in the Cu-O "chain" structure. These features are equivalent to modes observed by Raman scattering [60].

The magnetic hysteresis loops of YBCO were also studied [121]. The shape of the loops well below T_C (fig. 25) brought to mind the constricted hysteresis loops observed in certain ferromagnetic materials which are usually associated with magnetic aftereffects. Similar dynamic effects with time constants on the order of 10 seconds at 40 K were found to be present in YBCO. This is in addition to flux creep (due to thermally activated jumping over flux-pinning sites) observed for longer time periods. When the measurement time is fast compared to both time constants, the hysteresis loops can be approximated by a critical-state (i.e., Bean-Kim) model [122-126]. The experimental hysteresis loops at higher temperatures are more pinched than the critical-state model because of the movement of fluxoids.

The critical-state model, which provides a method for calculating the energy losses in type II superconductors, has been extended by Peterson [127] to include the train of magnetization jumps often seen at low temperatures in moderate-to-high magnetic fields. Chen and Goldfarb [128] have developed an analytic method for using the critical-state model to determine critical currents from magnetization measurements on the sample shapes most often encountered in developmental studies.

10. Theory

The interaction between two test charges in a solid can be described in terms of a total dielectric function that includes electronic and lattice polarization. Stability requirements place restrictions on the dielectric function. Allen et al. [129] show that the eigenvalues of the inverse dielectric matrix, λ_i, satisfy $\lambda_i < 1$. As a result, the electron-electron interaction (as determined by test charges) which enters BCS theory is not restricted to positive values by general stability requirements. Casella [130] considered other intermediate bosons, besides phonons, mediating the superconducting interaction and carried out a semiphenomenological analysis of the effects of certain band-gap features on the gap ratios of high-temperature superconductors. Comparison with experiment suggests that the intermediate boson is not a phonon.

Melamud et al. [131] studied the near-neighbor environments and the bonding of atoms in lanthanum and yttrium based copper-oxide superconductors using Wigner-Seitz cell construction. Wigner-Seitz cells can identify the nearest neigh-

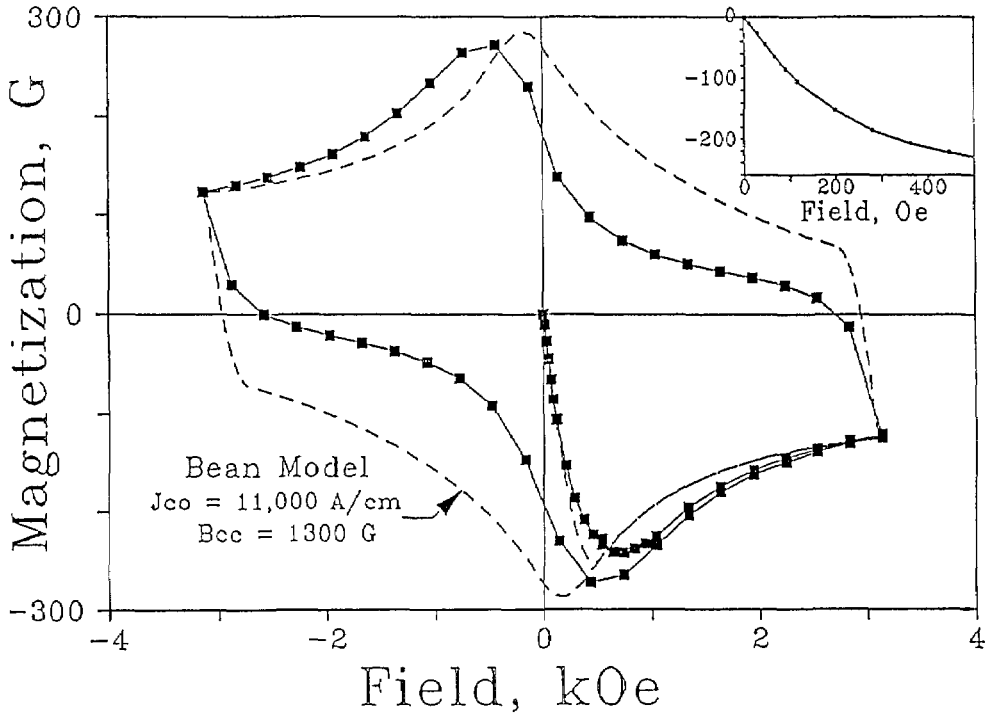

Figure 25. Experimental (solid line) and calculated (dotted line) hysteresis loops for YBCO at 38 K. The insert is an expanded view of the virgin curve [121].

bors, the site symmetry arising from the presence of these neighbors, and the number of nearest neighbors common to a near-neighbor pair. Different results were obtained depending on whether ionic or covalent/metallic bonding is assumed. Covalent/metallic bonding gave more reasonable chemical results and was consistent with known properties of these materials. The barium, lanthanum, and yttrium atoms all had large coordination numbers (see fig. 26) implying a three-dimensional chemical bonding scheme. The results are in agreement with the conclusion of Pauling [132] that the bonding at the important copper sites is not limited to oxygen but involves substantial interactions with large atoms such as lanthanum and barium.

11. Applications

Problems with current density and fabrication have hindered many applications of high-temperature superconductors. However, a successful prototype transition edge bolometer and a SQUID (*s*uperconducting *qu*antum *i*nterference *d*evice) made from YBCO have been developed [133, 134]. The breaking fixture used to form the Josephson contact for the SQUID is shown in figure 27. Variations in performance were found with different YBCO batches, and the first devices constructed showed considerable noise above 61 K, although quantum interference effects persisted up to 81 K. However, SQUIDs made from well-characterized, high-quality YBCO, operated in liquid nitrogen, with only a modest increase in noise over that found at 4 K. This provided the first demonstration that sensitive high-T_C SQUIDs operating at liquid nitrogen temperature are possible.

Many applications for high-temperature superconductivity depend on understanding and improving the critical current. To this end, a YBCO macrobridge (bridge dimensions are much greater than the coherence length) was fabricated [135] to understand not only J_C, but intra-film Josephson effects. Extremely noisy sections of the V-I curve were observed, always well below T_C. This behavior could have ramifications for potential low-noise applications of high-T_C superconductors. The noise depends on temperature, bias current, and the magnetic field. A very rapid change of switching rate with very small fields and small changes in bias current was observed, which suggests that the

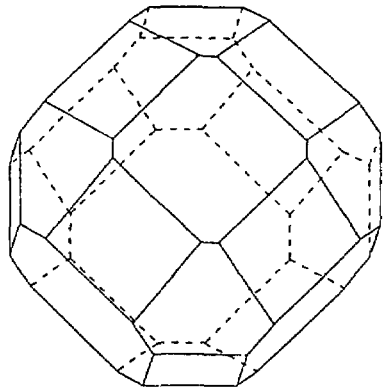

Figure 26. The (0 12 0 8 0 6) Wigner-Seitz polyhedron (coordination number=26) of the Ba, La or Y atom in the ideal ABO_3 perovskite structure, obtained with the use of metallic radii. In the high-temperature superconductors with distorted perovskite structure, the Wigner-Seitz cells for these sites are derivations from the ideal polyhedron [131].

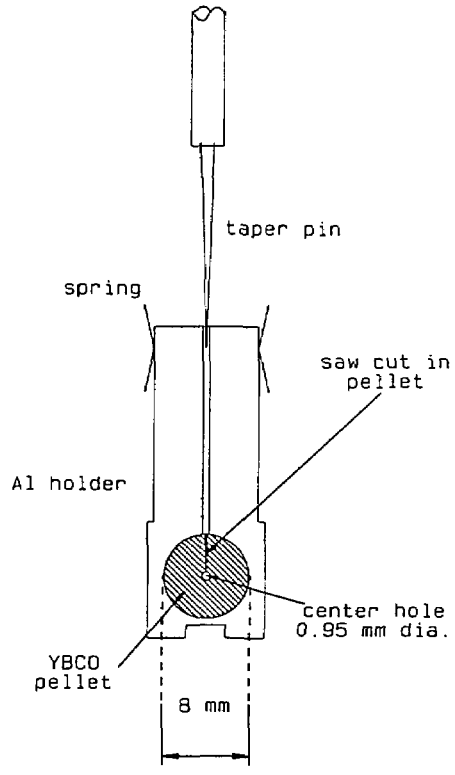

Figure 27. A SQUID made from a YBCO break junction. A YBCO pellet was secured with epoxy in an aluminum breaking fixture. A hole was drilled through the pellet and a saw cut made part way through so that the pellet would break along a diameter when the two arms of the fixture were spread apart by a thin tapered pin. Springs close the break as the taper is withdrawn [133].

noise may be due to the motion of vortices in and out of pinning sites.

The ability of a superconductor to levitate a magnet *above* its surface is well known, and for high-T_C superconductors it is often demonstrated. Recently, it has been realized [136, 137] that specially processed samples of a high-T_C superconductor can be levitated *below* a magnet. This unusual type of levitation involves "attraction" of the superconductor by a magnet rather than the Meissner effect "repulsion" seen for a levitated magnet. An important application for this effect would be in magnetic bearings (see table 1).

12. Other High-temperature Superconductors

Following the discovery of high-temperature superconductivity in Bi-Sr-Ca-Cu-O ceramics [138], $Bi_2Sr_2CaCu_2O_x$ was synthesized both chemically and by a solid state reaction [72]. ac susceptibility measurements showed transitions at 80 K and 110 K and a low H_{C1}. The appearance and amount of the 110 K superconductor was sensitive to the annealing procedure. Magnetic hysteresis loops constructed at 80 K were narrow, signifying a small amount of trapped flux. The loops were constricted in the center, indicating the probable existence of time effects similar to those seen in YBCO [121]. The bismuth superconductor was also studied by the magnetic-field-modulated-microwave-absorption (MAMMA) technique [65, 139]. Superconducting transitions were observed at 72, 100, and 110 K. An applied magnetic field broadened the microwave response peak much more than in the case of YBCO. Thin films of the bismuth superconductor were made [140] by laser ablation on ZrO_2 and characterized by MAMMA. The film quality was affected by substrate temperature and an annealing process. Unlike previous work [141], the films were not superconducting as deposited.

A classical test to determine the contribution of an electron-phonon interaction to the superconductivity is to measure the isotope shift [3, 4] in T_C. Substitution of ^{18}O for ^{16}O in the Bi-Sr-Ca-Cu-O system [142], the La-Sr-Cu-O system [143, 144], and the Y-Ba-Cu-O system [145, 146] has demonstrated a measurable, albeit small, isotope shift in T_C. Although this small effect indicates that the electron-phonon interaction contributes to the superconductivity, it is probably too small to account for the high values of T_C, and other mechanisms,

e.g., spin fluctuations must be operative. The possible role of various magnetic interactions have recently been addressed at a workshop held at NIST, Gaithersburg [147].

Magnetic measurements were made [148, 149] on chemically synthesized Bi-Pb-Sr-Ca-Cu-O. The lead substitution appears to encourage or stabilize the high-T_C Bi phase. The superconductor displayed extremely narrow hysteresis loops above liquid nitrogen temperatures, indicating a small number of effective flux pinning sites. Below 40 K, a dimpling was observed but only when the sample was a loosely packed powder. A flux depinning was observed, as illustrated in figure 28, for two temperatures. A plot of the flux-depinning field vs temperature appears to be linear (fig. 29).

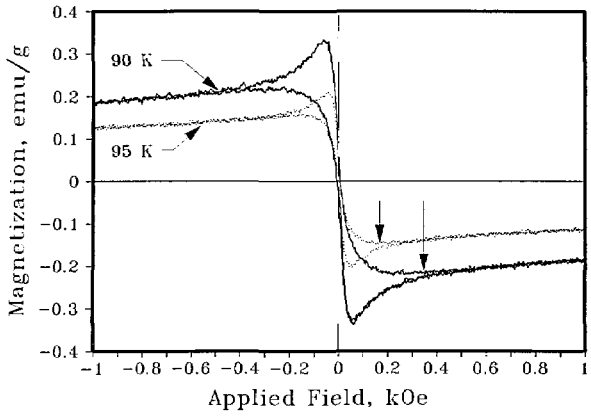

Figure 28. Hysteresis loops at two temperatures for a Bi-Pb-Sr-Ca-Cu-O superconductor, illustrating flux depinning [148].

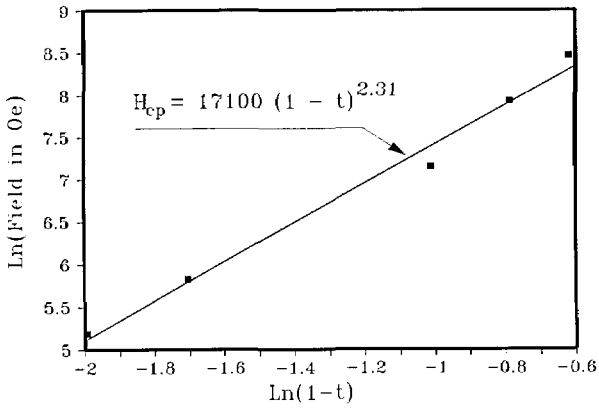

Figure 29. The flux-depinning field of the sample of figure 28 as a function of temperature [149].

Ultrasonic elastic-constant studies were carried out for Bi-Pb-Sr-Ca-Cu-O [150], with results similar to YBCO. There was stiffening during cooling, no measurable change at T_C, and hysteresis. However, the Bi-Cu-O is much softer than YBCO, with an elastic Debye temperature of 312 K vs 437 K.

Resonant photoemission has been used to study [151] the electronic states and electron-electron interactions in a bulk sample of Tl-Ba-Ca-Cu-O. The electron structure is similar to that of YBCO indicating that the electron states and interactions are similar. The surface of the Tl superconductor is not as reactive toward atmospheric gases as YBCO.

13. Low-Temperature Superconductors

Despite all the current interest in high-temperature superconductors, low-temperature superconductors will still be required in many applications. For example, the cost savings realized by switching from helium to nitrogen for cooling large magnets may be only a small part of the total operating cost. Additionally, much experience has been gained in learning how to fabricate these materials into practical conductors—in the shape of tapes or wires—that can support high current densities under realistic operating conditions. Therefore research on these materials is continuing, with the goal of optimizing their properties—e.g., current-carrying capabilities stability, ac losses, etc.

NIST is developing facilities and standards for the definition and measurement of superconductivity parameters [152, 153]. The facilities developed for this project enable critical currents up to 3000 A to be measured in fields up to 12 T in the presence of longitudinal or transverse stress. NIST is also involved in round robins on critical current measurements of Nb-Ti and Nb_3Sn with both domestic and foreign participants. Calibration techniques developed for the Nb-Ti study were used in the Nb_3Sn study. It was found that a small change in the mounting technique could result in a 40% change in the critical current density at 12 T. Mandrel material and geometry were also a source of error [154, 155].

The problem of current ripple on critical current measurement was studied [156, 157]. Ripple (the periodic departure from a dc output level) reduces the measured dc critical current, I_C, and causes noise at the input to the voltmeter used for measurements. A theoretical model of rippling was developed which was in good agreement with the experimental data and can be used to estimate the effects of current ripple on the measured dc I_C. It was also found that the effect of ripple should scale with its fraction of the I_C, and will depend upon the shape of the V-I curve.

At present, the material of choice in the windings for magnets is Nb-Ti. The effect of stress on current degradation has been studied by Ekin et al. Current degradation as a function of strand location and field angle on cable compacted into a keystone shape was evaluated [158]. It was found that cabling can lead to localized reductions in I_C within a single strand. The widest spread in local I_C along the cable strands was with the field perpendicular to the cable edge. Unfortunately, in the dipole magnet orientation, this orientation is near the critical orientation. The relevant I_C criteria may be a spatial average (the strand I_C). Therefore, both magnetic-field orientations, perpendicular and parallel to the cable width, need to be tested for I_C [159]. In addition, a large difference in current carrying capacity can exist between thick and thin cable edges, and thus, changing the direction of the test current can affect the measured I_C.

As illustrated in figure 30, the effects of various types of stress on I_C at 4 K also were studied [160]. It was found that I_C degradation from transverse compression was much less than from axial tension in terms of overall conductor stress but comparable in terms of stress on NbTi filaments. More stress can be developed in axial tension than in transverse compression because of the matrix. I_C is 95% reversible for both stresses indicating that the effects of stress will be seen only when the conductor is under stress. The primary source of degradation is a stress-induced reversible decrease in H_{C2}. It was found [161] that the effect on the critical current is independent of the temperature at which the stress is applied. Existing data obtained at 4 K can therefore be used to determine the degradation of T_C arising from room-temperature fabrication stress, cool-down stress, and 4 K stress due to the Lorentz force when the magnet is energized. Coupling losses in multifilamentary NbTi wire were studied [156] by vibrating sample magnetometry. Losses for wires with long twist lengths were up to twice the hysteresis losses. Using short twist lengths reduced these losses.

Non-uniformity of sample diameter (sausaging) of the filaments also degrades performance [152]. Sausaging causes a change in E-I response resulting in a significant electric field below I_C leading to heating and decreased stability. In the relationship $E \alpha I^n$, the value of n is related to the degree of sausaging with smaller values of n implying more necking. Therefore, the value of n can be used to estimate filament regularity (fig. 31).

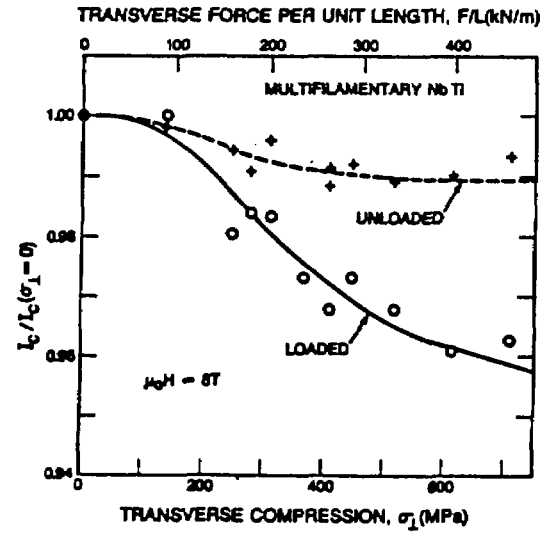

Figure 30. Effect of transverse compression force on the critical current of a NbTi conductor [160].

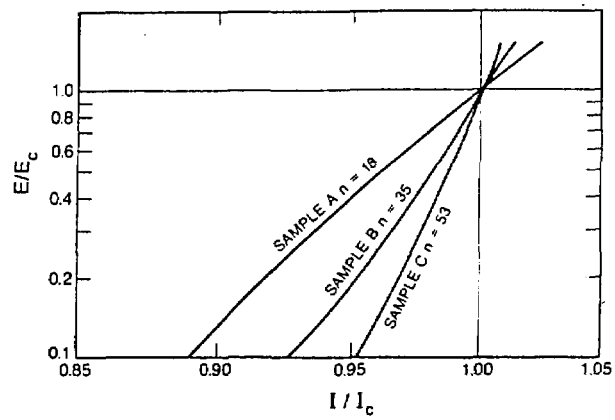

Figure 31. Logarithmic plot of electric field vs current for Nb-Ti samples with different n [152].

Another low-temperature superconductor which can be used for magnet applications is Nb_3Sn. A study of the effect of transverse stress on I_C degradation showed that the intrinsic effect on the upper critical field is about 10 times that of axial stress [162, 163]. This effect scales with conductor thickness and as a result places limits on conductor dimensions and the spacing between distributed reinforcements in large magnets. This is important in applications calling for larger conductors needed to limit inductance and keep induced quench voltages low in large magnet applications. Stress concentration at strand crossover points can significantly enhance the effects. This effect is reversible, but not totally. Hysteresis losses were

measured [156] on a series of fine filament Nb_3Sn superconductors made by the internal tin process. Hysteresis was measured as a function of filament diameter and interfilament separation. Losses were greater than predicted. This was due to interfilament bridging across the wires. The critical interfilament separation, for which the critical-state model would be accurate, was determined.

The cable matrix can also play a role in improving performance. The addition of manganese to a copper matrix of fine filament Nb-Ti wire was investigated by Goldfarb et al. [164]. Manganese additions had been shown to reduce proximity-effect coupling between closely-spaced filaments [165, 166]. The investigation found that as long as the manganese content was less than 4%, there were no adverse effects.

NIST has developed a wide variety of applications of superconductor electronics (which will be the subject of a future review). The most successful devices that NIST researchers have produced are array voltage standards (see fig. 32) containing as many as 19,000 Josephson junctions [167]. Such integrated circuits made at NIST using VLSI techniques are already in use in most national standards laboratories around the world and in two U.S. companies. Other devices made at NIST are ultra-high-speed analog-to-digital convertors, superconductor-insulator-superconductor mixers for radio astronomy at frequencies up to 300 GHz, SQUIDs with sensitivities approaching the uncertainty principle limit, samplers with response times of less than 10 ps, counters with rates above 100 GHz and sensitivity to pulses of 10^{-18} J, and an ultra-sensitive microwave and infrared detector based on the kinetic inductance of very thin superconducting films.

14. Conclusion

This review paper has attempted to show the breadth of NIST's work in superconductivity. Major contributions to the materials science, standardization, and engineering applications of superconductors are evident. To maintain a reasonable length, many topics have not been covered in the depth they deserve. Some of these, e.g., superconductive electronics, will be the subjects of future review articles. With all the world-wide attention on the new high-temperature superconductors and their potential economic impact, we can anticipate that NIST personnel will continue to make new and important contributions to this exciting field.

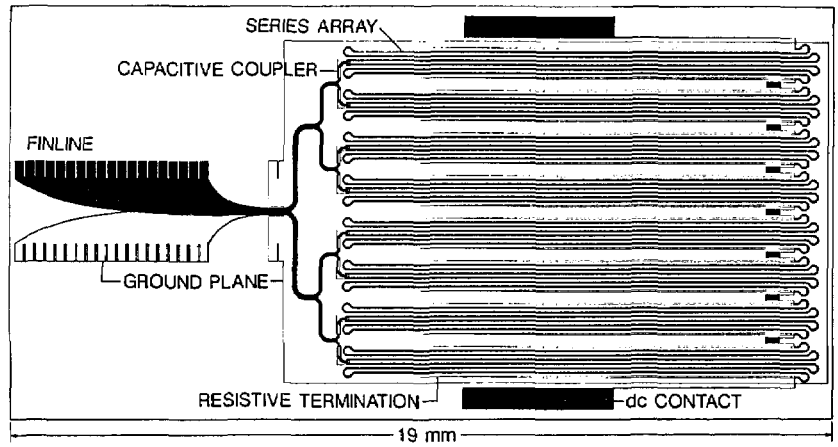

Figure 32. The layout for a Josephson junction array voltage standard chip fabricated using a seven-level photolithographic process [167].

15. Acknowledgements

We thank R. Powell for his aid in providing timely information on the NIST publications. R. A. Kamper, H. P. R. Frederikse, and K. Moorjani furnished extensive comments which have been incorporated in the manuscript. We are grateful to many of the referenced NIST authors for their aid in reducing our errors and omissions.

About the authors: All three authors are with the Magnetic Materials Group of the Metallurgy Division, Institute for Materials Science and Engineering, NIST, Gaithersburg. Donald R. Lundy is a Guest Scientist. Lydon J. Swartzendruber is a Research Metallurgist. Lawrence H. Bennett is a Physicist and the Group Leader.

16. References

* Papers authored or co-authored by NIST scientists.

*[1] Silsbee, F. B., J. Wash. Acad. Sci. **6**, 597 (1916).
[2] Meissner, W., and Oschenfeld, R., Naturwissenschaften **21**, 787 (1933).
*[3] Maxwell, E., Phys. Rev. **78**, 477 (1950).
[4] Reynolds, C. A., Serin, B., Wright, W. H., and Nesbitt, L. B., Phys. Rev. **78**, 487 (1950).
[5] Josephson, B. D., Phys Lett. **1**, 251 (1962); Rev. Mod. Phys. **36**, 216 (1964); Adv. Phys. **14**, 419 (1965).
[6] Bednorz, J. G., and Müller, K. A., Z. Phys. B-Condensed Matter **64**, 189 (1986); Müller, K. A., and Bednorz, J. G., Science **237**, 1133 (1987).
[7] Cohen, M. L., Phys. Rev. **134**, A442 (1964).
[8] Bardeen, J., Cooper, L. N., and Schrieffer, J. R., Phys. Rev., **108**, 1175 (1975).
*[9] Kahn, A. H., and Leyendecker, A. J., Phys. Rev., **135**, A1321 (1964).
*[10] Frederikse, H. P. R., Thurber, W. R., and Hosler, W. R., Phys. Rev. **134**, A442 (1964).
*[11] Schooley, J. F., Hosler, W. R., and Cohen, M. L., Phys. Rev. Lett. **12**, 474 (1964).
*[12] Ambler, E., Colwell, J. H., Hosler, W. R., and Schooley, J. F., Phys. Rev. **148**, 280 (1966).
*[13] Frederikse, H. P. R., Schooley, J. F., Thurber, W. R., Pfeiffer, E., and Hosler, W. R., Phys. Rev. **16**, 579 (1966).
[14] Michel, C., Er-Rakho, L., and Raveau, B., Mater. Res. Bull. **20**, 667 (1985).
[15] Tagaki, H., Uchida, S., Kitazawa, K., and Tanaka, T., Japn. J. Appl. Phys. **26**, L123 (1987).
[16] Wu, M. K., Ashburn, J. R., Torng, C. J., Hor, P. H., Meng, R. L., Gao, L., Huang, Z. J., Wang, Y. Q., and Chu, C. W., Phys. Rev. Lett. **58**, 908 (1987).
[17] Ginley, D. S., Kwak, J. F., Hellmer, R. P., Baughman, R. J., Venturini, E. L., and Morosin, B., Appl. Phys. Lett. **53**, 406 (1988).
[18] Cava, R. J., Batlogg, B., vanDover, R. B., Murphy, D. W., Sunshine, S., Siegrist, T., Remeika, J. P., Reitman, E. A., Zahurak, S., and Espinosa, G. P., Phys. Rev. Lett. **58**, 1676 (1987).
*[19] Beech, F., Miraglia, S., Santoro, A., and Roth, R. S., Phys. Rev. B **35**, 8778 (1987).
*[20] Santoro, A., Miraglia, S., and Beech, F., Sunshine, S. A., Murphy, D. W., Schneemeyer, L. F., and Waszczak, J. W., Mater. Res. Bull. **22**, 1007 (1987).
*[21] Rhyne, J. J., Neumann, D. A., Gotaas, J. A., Beech, F., Toth, L., Lawrence, S., Wolf, S., Osofsky, M., and Gubser, D. U., Phys. Rev. B **36**, 2294 (1987).
*[22] Miraglia, S., Beech, F., Santoro, A., Tran Qui, D., Sunshine, S. A., and Murphy, D. W., Mater. Res. Bull. **22**, 1733 (1987).
*[23] Cava, R. J., Santoro, A., Johnson, D. W., Jr., and Rhodes, W. W., Phys. Rev. B **35**, 6716 (1987).
*[24] Xiao, G., Cieplak, M. Z., Musser, D., Gavrin, A., Streitz, F. H., Chien, C. L., Rhyne, J. J., and Gotaas, J. A., Nature **332**, 238 (1988).
*[25] Miceli, P. F., Tarascon, J. M., Greene, L. H., Barboux, P., Griroud, M., Neumann, D. A., Rhyne, J. J., Schneemeyer, L. F., and Waszczak, J. V., Phys. Rev. B **38**, 9209 (1988).
*[26] Rubinstein, M., Harford, M. Z., Swartzendruber, L. J., and Bennett, L. H., J. Phys., Suppl., in press (1988).
*[27] Swartzendruber, L. J., Bennett, L. H., Harford, M. Z., and Rubinstein, M., J. Superconductivity **1**, 219 (1988).
*[28] Roth, R. S., Davis, K. L., and Dennis, J. R., Advanced Ceramic Mater.: Ceramic Superconductors, Vol. 2, 303 (1987).
[29] Frase, K. G., and Clarke, D. R., Adv. Cer. Mat. **8**, (313) 295 (1987).
[30] Wang, G., Hwu, S. J., Song, S. N., Ketteson, J. B., Marks, L. D., Poeppelmeir, K. R., and Mason, T. O., Adv. Cer. Mat. **2 (3B)**, 313 (1987).
*[31] Wong-Ng, W., McMurdie, H. F., Paretzkin, B., Hubbard, C. R., Dragoo, A. L., and Stewart, J. M., Powder Diffraction **2**, 106 (1987).
*[32] Wong-Ng, W., McMurdie, H. F., Paretzkin, B., Zhang, Y., Davis, K. L., Hubbard, C. R., Dragoo, A. L., and Stewart, J. M., Powder Diffraction **3**, (1987).
*[33] Wong-Ng, W., Roth, R. S., Beech, F., and Davis, K. L., submitted to Advances in X-Ray Analysis.
*[34] Wong-Ng, W., Kuchinski, M. A., McMurdie, H. F., and Paretzkin, B., submitted to Powder Diffraction.
*[35] Wong-Ng, W., McMurdie, H. F., Paretzkin, B., Kuchinski, M. A., and Dragoo, A. L., Powder Diffraction, to be published.
*[36] Wong-Ng, W., Davis, K. L., and Roth, R. S., J. Amer. Ceramic Soc. **71**, C64 (1987).
*[37] Roth, R. S., Rawn, C. J., Beech, F., Whitler, J. D., and Anderson, J. O., in Ceramic Superconductors II, Yan, M. F., Ed. (Am. Ceramic Soc., Westerville, OH, 1988) p. 13.
*[38] Roth, R. S., Rawn, C. J., Ritter, J. J., and Burton, B., submitted to the Journal of the American Ceramic Society, Communications.
*[39] Roth, R. S., Rawn, C. J., Whitler, J. D., Chiang, C. K., and Wong-Ng, W., submitted to the Journal of the American Ceramic Society.
*[40] Wong-Ng, W., and Cook, L. P., Advanced Ceramic Mater.: Ceramic Superconductors **2**, 624 (1987).
*[41] Wong-Ng, W., Cook, L. P., Chiang, C. K., Swartzendruber, L. J., Bennett, L. H., Blendell, J., and Minor, D., J. Mater. Res. **3**, 832 (1988).

*[42] Cook, L. P., Chiang, C. K., Wong-Ng, W., and Blendell, J., Advanced Ceramic Mater.: Ceramic Superconductors **2**, 656 (1987).
*[43] Chiang, C. K., Cook, L. P., Chang, S. S., Blendell, J. E., and Roth, R. S., Advanced Ceramic Mater.: Ceramic Superconductors **2**, 530 (1987).
*[44] Chiang, C. K., Cook, L. P., and Chang, S. S., submitted to the Proceedings of the Materials Research Society Symposium with the Japanese Materials Research Society.
*[45] Blendell, J. E., Handwerker, C., Vaudin, M. D., and Fuller, E. R., Jr., J. Crystal Growth **89**, 93 (1988).
*[46] Wong-Ng, W., Cook, L. P., Chiang, C. K., Swartzendruber, L. J., and Bennett, L. H., Adv. Cer. Materials, in press (1988).
*[47] Wong-Ng, W., Roth, R. S., Swartzendruber, L. J., Bennett, L. H., Chiang, C. K., Beech, F., and Hubbard, C. R., Advanced Ceramic Mater.: Ceramic Superconductors **2**, 565 (1987).
*[48] Zhang, Y., Wong-Ng, W., Morosin, B., Hubbard, C. R., Stewart, J. M., and Freiman, S. W., Physica C **152**, 130 (1988).
*[49] Ostertag, C. P., Beech, F., and Fuller, E. R., Jr., in Ceramic Powder Science II, Messing, G. L., Fuller, E. R., Jr. and Hausner, H., Eds. (Amer. Ceramic Soc., Westerville, OH, 1988) p.501.
*[50] Ritter, J. J., in Ceramic Powder Science II, Messing, G. L., Fuller, E. R., Jr. and Hausner, H., Eds. (Amer. Ceramic Soc., Westerville, OH, 1988) p.79.
*[51] Moorjani, K., Bohandy, J., Adrian, F. J., Kim, B. F., Shull, R. D., Chiang, C. K., Swartzendruber, L. J., and Bennett, L. H., Phys. Rev. B **36**, 4036 (1987).
*[52] Ono, R. H., Beall, J. A., Cromar, M. W., Mankiewich, P. M., and Howard, R. W., Proc. of 1988 Applied Superconductivity Conf., to be published in IEEE Trans. Magnetics.
*[53] Lindstrom, R. M., Trans. Amer. Nuclear Soc. **56**, 231 (1988).
*[54] Goldfarb, R. B., Clark, A. F., Panson, A. J., and Braginski, A. I., Materials Research Society, Vol. EA-11, 261 (1987).
*[55] Goldfarb, R. B., Clark, A. F., Braginski, A. I., and Panson, A. J., Cryogenics **27**, 475 (1987).
*[56] Chen, D.-X., Goldfarb, R. B., Nogues, J., and Rao, K. V., J. Appl. Phys. **63**, 980 (1988).
*[57] Blendell, J. E., Chiang, C. K., Cranmer, D. C., Freiman, S. W., Fuller, E. R., Jr., Drescher-Krasicka, E., Johnson, W. L., Ledbetter, H. M., Bennett, L. H., Swartzendruber, L. J., Marinenko, R. B., Myklebust, R. L., Bright, D. S., and Newbury, D. E., Advanced Ceramic Mater.: Ceramic Superconductors **2**, 512 (1987).
*[58] Blendell, J. E., Chiang, C. K., Cranmer, D. C., Freiman, S. W., Fuller, E. R., Jr., Drescher-Krasicka, E., Johnson, W. L., Ledbetter, H. M., Bennett, L. H., Swartzendruber, L. J., Marinenko, R. B., Myklebust, R. L., Bright, D. S., and Newbury, D. E., Chemistry of High Temperature Superconductors, Amer. Chem. Soc. Symp. 351, 240 (1987).
*[59] Marinenko, R. B., Newbury, D. E., Bright, D. S., Myklebust, R. L., and Blendell, J. E., Microbeam Analysis—1988, Newbury, D. E., Ed. (San Francisco Press, 1988) p. 37.
*[60] Etz, E. S., Wong-Ng, W., Blendell, J. E., and Chiang, C. K., in Microbeam Analysis 1988, Newbury, D. E., Ed. (San Francisco Press, San Francisco, CA 1988) p. 187.
*[61] Melmed, A. J., Shull, R. D., Chiang, C. K., and Fowler, H. A., Science **239**, 176 (1988).
*[62] Melmed, A. J., Shull, R. D., Chiang, C. K., and Fowler, H. A., Mater. Sci. Eng. **100**, L27 (1988).
*[63] Melmed, A. J., Shull, R. D., Chiang, C. K., and Fowler, H. A., J. Appl. Phys. **63**, 4232 (1988).
*[64] Melmed, A. J., Shull, R. D., and Chiang, C. K., J. Phys., in press (1988).
*[65] Bohandy, J., Adrian, F. J., Kim, B. F., Moorjani, K., Shull, R. D., Swartzendruber, L. J., Bennett, L. H., and Wallace, J. S., J. Superconductivity **1**, 191 (1988).
*[66] Blendell, J. E., and Stearns, L. C., in Ceramic Powder Science II, Messing, G. L., Fuller, E. R., Jr. and Hausner, H., Eds. (Amer. Ceramic Soc., Westerville, OH, 1988) p. 1146.
*[67] Stearns,L. C., Vaudin, M. D., Ostertag, C. P., Blendell, J. L., and Fuller, E. R., Jr., to be published in the Proceedings of the Superconductor Symposium, 90th Annual Meeting of the American Ceramic Society.
*[68] Ostertag, C. P., Shull, R. D., Vaudin, M. D., Blendell, J. E., Stearns, L. C., and Fuller, E. R., Jr., in Ceramic Superconductors II, Yan, M. F., Ed. (Amer. Ceramic Soc., Westerville, OH, 1988) p. 332.
*[69] Ekin, J. W., Panson, A. J., Blankenship, B. A., Appl. Phys. Lett. **52**, 331 (1988).
*[70] Ekin, J. W., Larson, T. M., Bergren, N. F., Nelson, A. J., Swartzlander, A. B., Kazmerski, L. L., Panson, A. J., and Blankenship, B. A., Appl. Phys. Lett. **52**, 1819 (1988).
*[71] Ekin, J. W., Panson, A. J., and Blankenship, B. A., in High Temperature Superconductors, Brodsky, M. B., Tuller, H. L., Dynes, R. C., and Kitazawa, K., Eds. (Materials Research Society Symposium Proceedings, Pittsburgh, Pa., 1988) Vol. 99.
*[72] Wallace, J. S., Ritter, J. J., Fuller, E. R., Jr., Bennett, L. H., Shull, R. D., and Swartzendruber, L. J., Phys. Rev. B. in press.
*[73] Moreland, J., and Goodrich, L. F., Proceedings of the Applied Superconductivity Conference, IEEE Transactions on Magnetics, in press.
*[74] Moreland, J., and Ekin, W. J., J. Appl. Phys. **58**, 3888 (1985).
*[75] Moreland, J., Clark, A. F., Ku, H. C., and Shelton, R. N., Cryogenics **27**, 227 (1987).
*[76] Moreland, J., Clark, A. F., Goodrich, L. F., Ku, H. C., and Shelton, R. N., Phys. Rev. B **35**, 8711 (1987).
*[77] Moreland, J., Ekin, J. W., Goodrich, L. F., Capobianco, T. E., and Clark, A. F., Materials Research Society, Vol. EA-11, 73 (1987).
*[78] Moreland, J., Ekin, J. W., Goodrich, L. F., Capobianco, T. E., Clark, A. F., Kwo, J., Hong, M., and Liou, S. H., Phys. Rev. B **35**, 8856 (1987).
*[79] Moreland, J., Goodrich, L. F., Ekin, J. W., Capobianco, T. E., Clark, A. F., Braginski, A. I., and Panson, A. J., Appl. Phys. Lett. **51**, 540 (1987).
*[80] Moreland, J., Goodrich, L. F., Ekin, J. W., Capobianco, T. E., and Clark, A. F., Japanese J. Appl. Phys. **26**, Supplement No. 26-3, 999 (1987).
*[81] Moreland, J., Clark, A. F., Damento, M. A., and Gschneider, K. A., Jr., Proc. Intern. Conf. on High Temperature Superconductivity Interlaken, Switzerland, (1988) p. 1383.
[82] Zeller, H. R., and Giaver, I., Phys. Rev. **181**, 789 (1969).
[83] Kapailtulnik, A., APS March Meeting 1987.

*[84] Moreland, J., Goodrich, L. F., Ekin, J. W., Capobianco, T. E., and Clark, A. F., Adv. Cryogenic Eng. **34**, 625 (1988).
*[85] Moreland, J., Beall, J. A., Ono, R. H., and Clark, A. F., Materials Research Society, EA-14, 351 (1987).
*[86] Moreland, J., Alexander, S., Cox, M., Sonnenfeld, R., and Hansen, P. K., Appl. Phys. Lett. **43**, 387 (1983).
[87] Geballe, T. H., in Novel Superconductivity (Plenum, N.Y. 1987) p. 1108.
*[88] Kurtz, R. L., AIP Proc. 165, Amer. Vac. Soc. Series 3: Thin Film Processing and Characteristics of High-T_c Superconductors, Harper, J. M. E., Colton, R. J., Feldman, L. C., Eds., NY (1988) p. 223.
*[89] Kurtz, R. L., Stockbauer, R. L., Mueller, D., Shih, A., Toth, L. E., Osofsky, M., and Wolf, S. A., Phys. Rev. B **35**, 8818 (1987).
*[90] Tsang, K.-L., Zhang, C. H., Callcott, T. A., Canfield, L. R., Ederer, D. L., Blendell, J. E., Clark, C. W., Wassdahl, N., Rubensson, J. E., Bray, G., Mortensson, N., Nordgren, J., Nyholm, R., and Cramm, S., Phys. Rev. B **37**, 2293 (1988).
*[91] Kurtz, R. L., Robey, S. W., Stockbauer, R. L., Mueller, D., Shih, A., and Toth, L., submitted to Phys. Rev. B.
*[92] Kurtz, R. L., Robey, S. W., Stockbauer, R. L., Mueller, D., Shih, A., Toth, L., Singh, A. K., and Osofsky, M., to be published in Vacuum as part of the Proceedings of 1st Iberian Vacuum Meeting.
*[93] Kurtz, R. L., Stockbauer, R., Madey, T. E., Mueller, D., Shih, A., and Toth, L. E., Phys. Rev. B **37**, 7936 (1988).
*[94] Mueller, D., Shih, A., Toth, L. E., Osofsky, M., Wolf, S. A., Kurtz, R. L., and Stockbauer, R. L., Phys. Rev. B **37**, 7936 (1988).
*[95] Moreland, J., Li, Y., Folsom, R., and Capobianco, T. E., Rev. Sci. Instruments, in press.
*[96] Moreland, J., Li, Y., Folsom, R. M., and Capobianco, T. E., to be published in the Proceedings of the Applied Superconductivity Conference, IEEE Transactions on Magnetics.
*[97] Ekin, J. W., Panson, A. J., Braginski, A. I., Janocko, M. A., Hong, M., Kwo, J., Liou, S. H., Capone, D. W., II, and Flandermeyer, B., Materials Research Soc., Vol. EA-11, 223 (1987).
*[98] Ekin, J. W., Advanced Ceramic Mater.: Ceramic Superconductors **2**, 586 (1987).
[99] Dinger, T. R., Wothington, T. K., Gallagher, W. J., and Sandstrom, R. L., Phys. Rev. Lett. **58**, 2687 (1987).
*[100] Ekin, J. W., Braginski, A. I., Panson, A. J., Janocko, M. A., Capone, D. W., II, Zaluzec, N. J., Flandermeyer, B., de Lima, O. F., Hong, M., Kwo, J., and Liou, S. H., J. Appl. Phys. **62**, 4821 (1987).
*[101] Peterson, R. L., and Ekin, J. W., Phys. Rev. B **37**, 9848 (1988).
*[102] Peterson, R. L., and Ekin, J. W., Physica C (to be published).
*[103] Ekin, J. W., Peterson, R. L., and Bray, S. L., Materials Research Society International Meeting on Advanced Materials, Tokyo, Japan, May 30-June 3, 1988.
*[104] Ledbetter, H., J. Metals **40**, 24 (1988).
*[105] Ledbetter, H. M., Austin, M. W., Kim, S. A., and Lei, M., J. Mater. Res. **2**, 786 (1987).
*[106] Ledbetter, H. M., Proc. MRS Int. Meeting on Advanced Mater. (Tokyo, June 1988).
*[107] Ledbetter, H. M., Austin, M. W., Kim, S. A., Datta, T., Violet, C. E., J. Mater. Res. **2**, 790 (1987).
*[108] Ledbetter, H. M., Kim, S. A., Datta, T., Estrada, J., and Violet, C. E., submitted to Phys. Rev. B.
*[109] Ledbetter, H. M., Kim, S. A., Datta, T., Estrada, J., and Violet, C. E., submitted to Physica C.
*[110] Ledbetter, H. M., Kim, S. A., and Capone, D. W., in High-Temperature Superconductors II (Materials Research Society Symposium Series, 1988) p. 293.
[111] Bishop, B. J., Ramirez, A. P., Gammel, P. L., Batlogg, B., Reitman, E. A., Cava, R. J., and Millis, R. J., Phys. Rev. B **36**, 2408 (1987).
[112] Geballe, T. H., and Hulm, J. K., Science **239**, 367 (1988).
*[113] Ledbetter, H. M., Kim, S. A., and Lei, M., in Cryogenic Materials 1988 (Int. Cryog. Mater. Conf., Boulder, CO, 1988).
*[114] Datta, T., Ledbetter, H. M., Violet, C. E., Almasan, C., and Estrada, J., Phys. Rev. B **37**, 7502 (1988).
*[115] Violet, C. E., Datta, T., Ledbetter, H. M., Almasan, C., and Estrada, J., in High Temperature Superconductors (Materials Research Society Symposium Series) **99**, 375 (1988).
[116] Testardi, L. R., Rev. Mod. Phys. **47**, 637 (1975).
*[117] Ledbetter, H. M., and Kim, S. A., Phys. Rev. B **38**, 11857 (1988).
*[118] Block, S., Piermarini, G. J., Munro, R. G., and Wong-Ng, W., Advanced Ceramic Mater.: Ceramic Superconductors, **2**, 601 (1987).
*[119] Ledbetter, H. M., and Lei, M., to be published; Ledbetter, H. M., to be published.
*[120] Drescher-Krasicka, E., Johnson, W. L., Blendell, J. E., Chiang, C. K., and Wadley, H. N. G., submitted to Physical Review Letters.
*[121] Atzmony, U., Shull, R. D., Chiang, C. K., Swartzendruber, L. J., Bennett, L. H., and Watson, R. E., J. Appl. Phys. **63**, 4179 (1988).
[122] Bean, C. P., Rev. Mod. Phys. **361**, 39 (1964).
[123] Bean, C. P., Phys. Rev. Lett. **8**, 250 (1962).
[124] Kim, Y. B., Hempstead, C. F., and Strnad, A. R., Phys. Rev. Lett. **9**, 306 (1962).
[125] London, H., Phys. Lett. **6**, 162 (1963).
[126] Kamper, R. A., Phys. Lett. **2**, 290 (1962).
*[127] Peterson, R. L., submitted to Physics Letters A, May 11, 1988.
*[128] Chen, D.-X., and Goldfarb, R. B., to be published.
*[129] Allen, P. B., Cohen, M. L., and Penn, D. R., Phys. Rev. B. **38**, 2513 (1988).
*[130] Casella, R. C., Nuovo Cimento **10D**, 1439 (1988).
*[131] Melamud, M., Bennett, L. H., and Watson, R. E., Phys. Rev. B **38**, 4624 (1988).
[132] Pauling, L., Phys. Rev. Lett. **59**, 225 (1987).
*[133] Zimmerman, J. E., Beall, J. A., Cromar, M. W., and Ono, R. H., Appl. Phys. Lett. **51**, 617 (1987).
*[134] Zimmerman, J. E., Beall, J. A., Cromar, M. W., and Ono, R. H., Japn. J. Appl. Phys. **26**, Suppl. 26-3, 2125 (1987).
*[135] Ono, R. H., Beall, J. A., Cromar, M. W., Mankiewich, P. M., Howard, R. W., and Skocpol, W., IEEE Trans. on Magnetics, MAG-25 (1989).
*[136] Huang, C. Y., Shapira, Y., McNiff, E. J., Jr., Peters, P. N., Schwartz, B. B., Wu, M. K., Shull, R. D., and Chiang, C. K., Mod. Phys. Lett. **B2**, 869 (1988).
*[137] Shull, R. D., Swartzendruber, L. J., Chiang, C. K., Wu, M. K., Peters, P. N., and Huang, C. Y., in High-T_c Superconductors: Magnetic Interactions, World Scientific Publishing Co. (1988).

[138] Cava, R. J., Batlogg, B., van Dover, R. B., Murphy, D. W., Sunshine, S., Siegrist, T., Remeika, J. P., Reitman, E. A., Zahurak, S., and Espinosa, G. P., Phys. Rev. Lett. **58**, 1676 (1987).

*[139] Adrian, F. J., Bohandy, J., Kim, B. F., Moorjani, K., Shull, R. D., Swartzendruber, L. J., and Bennett, L. H., Physica C **156**, 184 (1988).

*[140] Kim, B. F., Phillips, T. E., Green, W. J., Agostinelli, E., Adrian, F. J., Moorjani, K., Swartzendruber, L. J., Shull, R. D., Bennett, L. H., and Wallace, J. S., Appl. Phys. Lett., **53**, 321 (1988).

*[141] Moorjani, K., Bohandy, J., Adrian, F. J., Kim, B. F., Atzmony, U., Shull, R. D., Chiang, C. K., Swartzendruber, L. J., and Bennett, L. H., J. Appl. Phys. **63**, 4199 (1988).

*[142] Katayama-Yoshida, H., Hirooka, T., Oyamada, A., Okabe, Y., Takahashi, T., Sasaki, T., Ochiai, A., Suzuki, T., Mascarenhas, A. J., Pankove, J. I., Ciszek, T. F., Deb, S. K., Goldfarb, R. B., and Li, Y., Physica C **156**, 481 (1988).

[143] Batlogg, B., Kourouklis, G., Weber, W., Cava, R. J., Jayaraman, A., White, A. E., Short, K. T., Rupp, L. W., and Rietman, E. A., Phys. Rev. Lett. **59**, 912 (1987).

[144] Faltens, T. A., Ham, W. K., Keller, S. W., Leary, K. J., Michaels, J. N., Stacy, A. M., zur Loye, H. C., Barbee, T. W., III, Bourne, L. C., Cohen, M. L., Hoen, S., and Zettl, A., Phys. Rev. Lett. **59**, 915 (1987).

[145] Leary, K. J., zur Loye, H. C., Keller, S. W., Faltens, T. A., Ham, W. K., Michaels, J. N., and Stacy, A. M., Phys. Rev. Lett. **59**, 1236 (1987).

[146] Morris, D. E., Kuroda, R. M., Marketz, A. G., Nickel, J. H., and Wei, J. Y. T., Phys. Rev. B **37**, 5936 (1988).

*[147] High-T_C Superconductors: Magnetic Interactions, Bennett, L. H., Vezzoli, G., and Flom, Y., Eds. (World Scientific Publishing Co., Teaneck, NJ, 1989).

*[148] Lundy, D. R., Ritter, J., Swartzendruber, L. J., Shull, R. D., and Bennett, L. H., J. Superconductivity in press, 1989.

*[149] Lundy, D. R., Ritter, J., Swartzendruber, L. J., Shull, R. D., and Bennett, L. H., in High-T_C Superconductors: Magnetic Interactions, (World Scientific Publishing Co., Teaneck, NJ, 1989).

*[150] Ledbetter, H. M., Kim, S. A., Goldfarb, R. B., and Togano, K., to be published.

*[151] Stockbauer, R. L., Robey, S. W., Kurtz, R. L., Mueller, D., Shih, A., Singh, A. K., Toth, L., and Osofsky, M., AIP Conference Proceedings of AVS Topical Conference on Thin Film Processing and Characterization of High-Temperature Superconductors, Atlanta, Georgia (October, 1988).

*[152] Ekin, J. W., Cryogenics 1987 **27**, 603 (1987).

*[153] Bray, S. L., Goodrich, L. F., Dubé, W. P., submitted to RSI, May 12, 1988.

*[154] Goodrich, L. F., and Bray, S. L., submitted to Cryogenics, July 7, 1988.

*[155] Goodrich, L. F., Bray, S. L., and Stauffer, T. C., Proceedings of the Applied Superconductivity Conference, IEEE Transactions on Magnetics.

*[156] NBSIR 88-3088, Goodrich, L. F., Editor, published by the National Bureau of Standards, 75 pages (1988).

*[157] Goodrich, L. F., Bray, S. L., and Clark, A. F., Advances in Cryogenic Engineering Mater. **34**, 1019 (1988).

*[158] Goodrich, L. F., Pittman, E. S., Ekin, J. W., and Scanlan, R. M., IEEE Trans. on Magnetics, **MAG-23**, 1642 (1987).

*[159] Goodrich, L. F., and Bray, L. S., to be published in the Proceedings of the Applied Superconductivity Conference, IEEE Transactions on Magnetics.

*[160] Ekin, J. W., IEEE Trans. on Magnetics, **MAG-23**, 1634 (1987).

*[161] Bray, S. L., and Ekin, J. W., Journal of Applied Physics, in press.

*[162] Ekin, J. W., Advances in Cryogenic Engineering Mater. **34**, 547 (1988).

*[163] Ekin, J. W., J. Appl. Phys. **62**, 4829 (1987).

*[164] Goldfarb, R. B., Ried, D. L., Kreilick, T. S., and Gregory, E., to be submitted to Applied Superconductivity Conference—1988 for publication in IEEE Transactions on Magnetics.

[165] Collings, E. W., Adv. Cryoeng. (Materials) **34**, 817 (1988)

[166] Kreilick, T. S., Gregory, E., Wong, J., Scanlan, R. M., Ghosh, A. K., Sampson, W. B., and Collings, E. W., Adv. Cryoeng. (Materials) **34**, 895 (1988).

*[167] Lloyd, F. L., Hamilton, C. A., Beall, J. A., Go, D., Ono, R. H., and Harris, R. E., IEEE Electron Device Letters, **EDL-8**, 449 (1987).

The following additional papers authored or co-authored by NIST personnel were not received in time for inclusion in the review:

Moreland, J., Ono, R. H., Beall, J. A., Madden, M., and Nelson, A. J., submitted to Applied Physics Letters.

Chaillout, C., Santoro, A., Remeika, J. P., Cooper, S. A., Espinosa, G. P., and Marezio, M., Solid State Communications **65**, 1363 (1988).

Bordet, P., Hodeau, J. L., Strobel, P., Marezio, M., and Santoro, A., Solid State Communications **66**, 435 (1988).

Chang, K. J., Cohen, M. L., and Penn, D. R., Phys. Rev. B **38**, 8691 (1988).

Goldfarb, R. B., Cizek, T. F., and Evans, C. D., J. Appl. Phys. **64**, 5914 (1988).

Nikolo, M., and Goldfarb, R. B., submitted for publication.

Moreland, J., Goodrich, L. F., Ekin, J. W., Capabianco, T. E., and Clark, A. F., National Institute of Standards and Technology, NISTIR 88-3090 (May 1988).

Zhang, C. H., Callcott, T. A., Tsang, K.-L., Ederer, D. L., Blendell, J. E., Clark, C. W., Scimeca, T., and Liu, Y.-W., Phys. Rev. B (March 1, 1989).

Callcott, T. A., Tsang, K.-L., Zhang, C. H., Ederer, D. L., Clark, C. W., Wassdahl, N., Rubensson, J. E., Bray, G., Mortensson, N., Nordgren, J., Nyholm, R., and Cramm, S., Extended Abstracts, High-Temperature Superconductors II, April 5-9, 1988, Reno, NY.

Tsang, K.-L., Zhang, C. H., Callcott, T. A., Canfield, L. R., Ederer, D. L., Blendell, J. E., and Clark, C. W., Drexel High-T_c Conference Proceedings (July 1987).

Ederer, D. L., Canfield, L. R., Callcott, T. A., Tsang, K.-L., Zhang, C. H., Arakawa, E. T., SPIE, 911, X-Ray and VUV Interaction Data Bases, Calculations and Measurements, p. 75 (1988).

Tsang, K.-L., Zhang, C. H., Callcott, T. A., Canfield, L. R., Ederer, D. L., Blendell, J. E., Clark, C. W., Wassdahl, N., Rubensson, J. E., Bray, G., Mortensson, N., Nordgren, J., Nyholm, R., and Cramm, S., J. Phys., Colloque C9 supplement au n°12, **48** (December 1987).

Peterson, R. L., submitted to Phys. Rev. B.

Katayama-Yoshida, H., Hirooka, T., Oyamada, A., Okabe, Y., Takahashi, T., Sasaki, T., Ochiai, A., Suzuki, T., Mascarenhas, A. J., Pankove, J. I., Ciszek, T. F., Deb, S. K., Goldfarb, R. B., and Li, Y., Physica C **156**, 481 (1988).

Chen, D.-X., and Goldfarb, R. B., submitted to the Proceedings of the March 1989 Meeting of the American Physical Society.

Peterson, R. L., and Ekin, J. W., Physica C (1989).

Casella, R. C., Solid State Communications (in press) 1989.

De Reggi, A. S., Chiang, C. K., Swartzendruber, L. J., and Davis, G. T., High-T_c Superconductors: Magnetic Interactions (World Scientific Publishing Co., Teaneck, N. J. 1989).

Swartzendruber, L. J., Bennett, L. H., and Gallo, C. F., High-T_c Superconductors: Magnetic Interactions (World Scientific Publishing C., Teaneck, N. J. 1989).

Rubinstein, M., Swartzendruber, L. J., Bennett, L. H., Chaki, T. K., Harford, M. Z., Wolf, S. A., and Edelstein, A. E., High-T_c Superconductors: Magnetic Interactions (World Scientific Publishing Co., Teaneck, N. J. 1989).

Wu, M. K., Shull, R. D., Swartzendruber, L. J., Chiang, C. K., Peters, P. N., and Huang, C. Y., High-T_c Superconductors: Magnetic Interactions (World Scientific Publishing Co., Teaneck, N. J. 1989).

Kaiser, D. L., Gayle, F. W., Roth, R. S., and Swartzendruber, L. J., J. Materials Res., submitted 1989.

Swartzendruber, L. J., and Bennett, L. H., J. Phys., in press 1988.

Swartzendruber, L. J., and Bennett, L. H., J. Superconductivity, in press 1988.

Wong-Ng, W., Cook, L. P., Chiang, C. K., Swartzendruber, L. J., and Bennett, L. H., Mater. Res. Soc., in press 1989.

Volume 94, Number 3, May-June 1989
Journal of Research of the National Institute of Standards and Technology

Calibration of Voltage Transformers and High-Voltage Capacitors at NIST

Volume 94 Number 3 May-June 1989

William E. Anderson

National Institute of Standards and Technology,
Gaithersburg, MD 20899

The National Institute of Standards and Technology (NIST) calibration service for voltage transformers and high-voltage capacitors is described. The service for voltage transformers provides measurements of ratio correction factors and phase angles at primary voltages up to 170 kV and secondary voltages as low as 10 V at 60 Hz. Calibrations at frequencies from 50–400 Hz are available over a more limited voltage range. The service for high-voltage capacitors provides measurements of capacitance and dissipation factor at applied voltages ranging from 100 V to 170 kV at 60 Hz depending on the nominal capacitance. Calibrations over a reduced voltage range at other frequencies are also available. As in the case with voltage transformers, these voltage constraints are determined by the facilities at NIST.

Key words: calibration; capacitors; dissipation factor; electric power; electrical standards; NIST services; voltage transformers.

Accepted: February 15, 1989

1. Introduction

This paper describes the National Institute of Standards and Technology (NIST) methodology for calibrating high-voltage capacitors and transformers. This should benefit NIST clients in several ways. First, by understanding how NIST makes these measurements, the clients might be able to define weaknesses in their own measurement procedures and correct them. Second, the clients should be able to make better use of the data in the calibration report (e.g., to understand what is meant by the uncertainty statement). Third, the clients should be able to better specify the required test conditions so that information more pertinent to their needs can be obtained at a lower cost.

This paper describes two different calibration services: high-voltage capacitors and voltage transformers. At NIST these two services are performed using the same equipment. In fact, in order to calibrate a voltage transformer, one of the steps is to measure the ratio of two capacitors. The two services are therefore discussed in parallel.

There are several different ways to measure the ratio and phase angle of a voltage transformer. Harris [1] categorizes them as the direct versus comparative methods and within these two classifications either the deflection or null measurement technique. A direct measurement is defined here as a measurement in which the quantity of interest can be determined without a comparison to some absolute standard.

In the "direct deflection method" the primary and secondary voltage vectors are each directly measured. This approach is, in general, of most value for lower voltage transformers (i.e., primary voltages of order 100 V). Even then more accurate, less difficult measurements can be made using one of the other techniques.

In the past NIST had used a "comparative null method" to calibrate voltage transformers. The unknown transformer was compared to a NIST reference transformer using a voltage comparator consisting of a variable resistive divider and a mutual inductor. Reference transformers were available with ratios ranging from 1/1 up to 2000/1. Measurement uncertainties in the comparison of the unknown transformer with the reference transformer were ±0.01% for ratio and ±0.3 minutes for phase angle. The ratio and phase angle of the reference transformers were known to about the same accuracy. There are several disadvantages to this approach. Since the comparator has a limited range, several reference transformers must be available to cover the anticipated users' needs. The ratio and phase angles of each one of these transformers must be carefully determined over the secondary voltage range of interest. These transformers then have to be rechecked at regular intervals to determine if the ratios and phase angles have changed.

If a direct measurement method were available that was sufficiently accurate and straightforward to make the calibration of these reference transformers a simple task, then that method could be used to measure the client's transformer directly. At NIST, the "direct null method" in use originally involved balancing the secondary of the reference transformer against the output of a resistive divider used in conjunction with a variable mutual inductor to provide phase angle balance. Such a measurement was difficult because the resistive divider ratio changed with heating. Since the late 1960s a "direct null method" has been available that is straightforward and accurate and is now used at NIST in place of comparative methods using reference transformers.

Capacitors are invariably measured by balancing the unknown capacitor against a known standard using some type of bridge arrangement. There are a variety of such bridges described in the literature [2]. The one most used in high-voltage applications in the last 60 years is the Schering bridge (fig. 1). The two high-voltage arms of this bridge consist of the standard and unknown capacitors. The two low voltage arms are resistors (one has a parallel capacitor for phase angle balance).

The main limitation of the Schering bridge is that the low side of the unknown and standard capacitors are not at ground potential at bridge balance. Therefore, without carefully guarding the bridge components, stray currents can affect the bridge accuracy. The voltage applied to the shields to eliminate these stray currents must be adjusted for both magnitude and phase. Unfortunately this procedure is not perfect and bridge accuracy is consequently affected. Another limitation of the Schering bridge is the inherent inaccuracy of the resistance ratio of the two low-voltage arms.

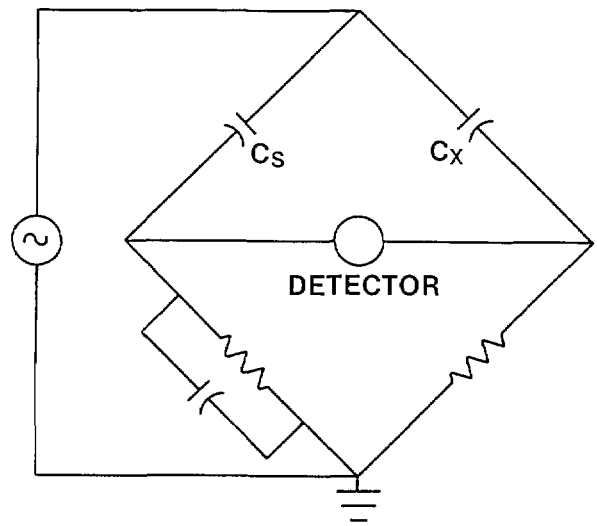

Figure 1. Schering bridge.

The current comparator bridge developed by Kusters and Petersons [3] allows the intercomparison of two capacitors with their low-voltage terminals at ground potential, thereby eliminating the main objection in using the Schering bridge. This bridge, used in both voltage transformer and capacitor calibrations, will be described in some detail in section 4. There is an important distinction between the calibration of voltage transformers and capacitors at NIST. The voltage transformer calibration is of the direct null type, and the capacitor calibration is of the comparative null type. In other words, the accuracy of the capacitance measurements ultimately depends on the uncertainty in assigning a value to a standard capacitor. The standard capacitor used in this service is directly traceable to the calculable cross capacitor [4] which, in turn, is known in terms of the fundamental unit of length.

The remainder of this paper is divided into the following subject areas: voltage transformers and capacitors covered by the service, measurement methodology, measurement instrumentation, and analysis of uncertainties. The contents of this paper plus the cited references should provide the reader with a fairly complete description of the voltage transformer and high-voltage capacitor calibration services at NIST.

2. Range of Services

The NIST measurement capabilities are summarized in table 1 and discussed in more detail below.

Table 1. Measurement capability

Voltage transformers—60 Hz		
Primary voltage	Secondary voltage	Phase angle
50–170,000 V rms	>50 V rms	<11 mrad
Capacitors—60 Hz		
Applied voltage[a]	Capacitance	Dissipation factor
50–170,000 V rms	10 pF–0.001 F	<0.011

[a] Total power must be less than 50 kVA.

2.1 Voltage Transformers

Presently, voltage transformers (assuming they are of sufficient quality to be used as laboratory standards) with primary voltages up to 170 kV at a frequency of 60 Hz can be calibrated at NIST. This maximum voltage is imposed by the supply transformer and not by limitations in the measurement instrumentation. Therefore, this constraint should not be considered rigid and clients should contact the NIST about present physical limitations.

The largest portion of the voltage transformers submitted to NIST are calibrated with total estimated uncertainties of ±300 parts per million (ppm) in ratio, and ±0.3 mrad in phase angle. These transformers are of sufficient quality to be considered transfer standards. Historically these transformers have shown excellent long-term stability, rarely changing by more than 100 ppm in ratio or 0.1 mrad in phase (at or below rated burden) for periods as long as 30 years or more. In general, the voltage and burden dependence of these transformers are the major contributors to the measurement uncertainties. These uncertainties (±300 ppm for ratio, ±0.3 mrad for phase angle) meet the accuracy requirements of most NIST clients.

Voltage transformers of a higher accuracy class often serve as transfer standards for manufacturers of voltage transformers and voltage transformer test sets (voltage comparators). The estimated uncertainties for these transformers are ±100 ppm in ratio, and ±0.1 mrad in phase angle. They are generally designed for use with very small burdens (<15 volt-amperes).

The above discussion for voltage transformers assumes a voltage at a frequency of 60 Hz. The National Institute of Standards and Technology has some capability to calibrate voltage transformers from about 50 Hz to 400 Hz (at the lower voltage and power ranges). Such calibrations are infrequent and clients interested in these voltage ranges and measurement uncertainties should contact NIST directly.

2.2 Capacitors

The maximum voltage for capacitor calibrations is presently 170 kV at 60 Hz. The restrictions are imposed by the supply transformer and not by limitations in the measurement instrumentation. Therefore, this constraint should not be considered time invariant and clients should contact NIST about present physical limitations.

The maximum power available is 50 kVA (i.e., $C<50{,}000/\{2\pi 60V^2\}$ where V is the applied voltage and C is the capacitance). In order to energize the capacitors a resonant circuit is often required to couple the necessary energy into the client's capacitor. Since this requires the availability of an assortment of series and parallel inductors and capacitors, there are undoubtedly some capacitors that, despite having a burden of less than 50 kVA, cannot be calibrated. The client should contact NIST before submitting a capacitor for calibration. As with voltage transformers, NIST restricts its calibration services to those devices of sufficient quality to be used as transfer standards. This in general depends upon the stability of the capacitor (i.e., whether the measured capacitance and dissipation factor are intrinsic properties of the device itself or instead are largely a function of conditions at the time of the calibration). For example, small two-terminal capacitors (less than 10,000 pF) may be significantly influenced by stray capacitance in the measurement circuit. There are cases, however, where one component (capacitance or dissipation factor) is stable and the other is not. For example, power factor capacitors often have relatively stable dissipation factors but have capacitances that vary significantly with applied voltage (even demonstrating hysteresis effects) and temperature. In this case a calibration of dissipation factor would be meaningful. It also is important that the capacitors have connectors[1] that are generally available, e.g., BNC, GR, UHF, BPO, or Type N.

[1] Certain commercial products are identified to adequately specify the experimental procedure. In no case does such identification imply recommendation by NIST, nor does it imply the products are the best available.

The most accurate capacitor calibrations have an uncertainty of ±25 ppm for capacitance and an uncertainty of $\pm 5 \times 10^{-6}$ for dissipation factor. For capacitors with large dissipation factors, the dissipation factor uncertainty is generally at least ±1% of the measured value $\pm 5 \times 10^{-6}$. The uncertainty in the capacitance value and the dissipation factor can be largely a function of the stability of the capacitor.

3. Measurement Methodology

3.1 Basic Measurement Circuits

The current comparator bridge used to calibrate voltage transformers and high-voltage capacitors will be discussed in considerable detail in section 4. A brief discussion of this bridge will be presented here in order to facilitate understanding of the NIST measurement methodology. A simplified circuit for measuring the ratio of two capacitors is shown in figure 2. (The active circuitry to achieve dissipation factor balance is not included.) At balance

$$\frac{V 2\pi f C_x N_x}{N_D} = \frac{V 2\pi f C_s N_s}{N_D}, \tag{1}$$

where f is the frequency. This can be rewritten

$$C_x = \frac{N_s}{N_x} C_s . \tag{2}$$

The simplified circuit for measuring the ratio of voltage transformers is shown in figure 3. At balance

$$\frac{V_p 2\pi f C_p N_x}{N_d} = \frac{V_s 2\pi f C_s N_s}{N_d} \tag{3}$$

or,

$$\frac{V_p}{V_s} = \frac{N_s C_s}{N_x C_p} . \tag{4}$$

The ratio of the two capacitors in eq (2) can be measured using the circuit of figure 2.

The measurement of a voltage transformer or a capacitor both involve the measurement of the ratio of two standard capacitors. The measurement of capacitors will be discussed below followed by a discussion on the measurement of voltage transformers.

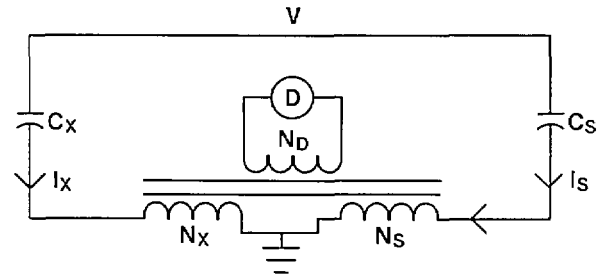

Figure 2. Basic measurement circuit for the calibration of a high-voltage capacitor.

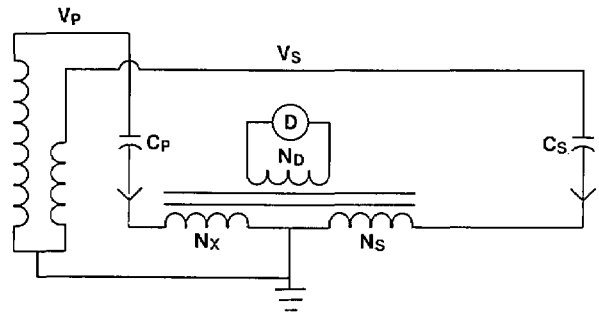

Figure 3. Basic measurement circuit for the calibration of a voltage transformer.

3.2 Capacitors

3.2.1 General Measurement Technique Capacitors are measured by balancing the current through the capacitor under test against the current through a standard air or compressed gas capacitor as shown in figure 2. Large capacitors (>1 μF) necessitate a four-terminal measurement as shown in figure 4. This measurement will be discussed in section 4. The four-terminal measurement eliminates the effect of leads in the measurement of capacitance and dissipation factor.

3.2.2 Information Necessary to Initiate Calibration The client usually only needs to specify the voltage and the frequency. For small capacitors (10,000 pF or less), it is essential that the low-voltage electrode and the conductor leading to the measurement instrumentation be shielded by a grounded conductor. Otherwise, the stray capacitance may cause significant measurement error. The National Institute of Standards and Technology requires some sort of standard connector (BNC, UHF, GR, BPO, or Type N) at the low-voltage terminal in order to connect to the measurement system. Larger capacitors do not need to

be shielded but must be measured as a four terminal admittance because of the non-negligible lead impedance. A description of how this measurement is done will be covered in section 4. Capacitors must be stable and reproducible in order to be considered standards and hence warrant a NIST calibration. Power factor capacitors (large capacitors used to tune distribution lines, etc.) are often special cases. Their dissipation factors (in-phase component of the current divided by quadrature component) are often quite stable but their capacitance values are often not. Because of the importance of these capacitors to the electrical industry, they are often acceptable for calibration even though they do not meet normal stability requirements.

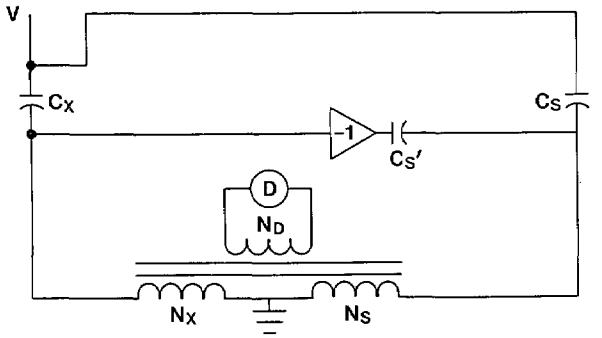

Figure 4. Basic measurement circuit for the four-terminal calibration of large capacitors.

Although the instrumentation has been used to calibrate a million-volt standard capacitor at rated voltage, the instrumentation does impose some limitations on the voltage applied to the capacitor. The only limitation on the maximum voltage is that the current through the standard capacitor should be no larger than 10 mA. In order to have reasonable sensitivity, the current should be at least 10 μA. The current through the client's capacitor can range from 10 μA to 1000 A.

3.2.3 Voltage Dependence For the calibration of both capacitors and voltage transformers, the voltage coefficient of the standard capacitor is important. The unit of capacitance at NIST is maintained at low voltage. This value must be transferred to the high-voltage standard capacitors at their working voltages. At NIST, considerable work was done to modify a commercial high-voltage standard capacitor to minimize its voltage coefficient and to determine the magnitude of that voltage coefficient [5]. The National Institute of Standards and Technlogy was able to demonstrate that, if care is taken, a well-designed standard capacitor should change capacitance by only a few ppm from 0 to 300 kV. A more recent paper also discusses the problem of the voltage dependence of standard capacitors and describes an international comparison of high-voltage capacitor measurements [6]. (This paper also discusses the effect of shipping and handling on the measured capacitance of a commercial standard capacitor.) The voltage dependence of a compressed gas capacitor principally arises from the coulombic attraction of the two electrodes and is hence quadratic in nature. The capacitor should be expected to vary only slightly at lower voltages. Therefore, a capacitor rated at 200 kV should be quite effective in measuring the voltage dependence of another capacitor rated at 20 kV.

3.2.4 Temperature Dependence Another concern is the temperature dependence of the high-voltage standard capacitor. The typical dependence is about +20 ppm/°C. This dependence arises solely from the thermal expansion of the components of the capacitor. Since C is directly proportional to the electrode area and inversely proportional to the electrode separation, the thermal coefficient of the standard capacitor is proportional to the linear coefficient of expansion. Although the laboratories at NIST are fairly stable in temperature, the comparison of the high-voltage standard capacitor to the low-voltage standard (which has a thermal coefficient of 2 ppm/°C) is done at the beginning and conclusion of the measurement process. The average value is then used in order to minimize the problem associated with this thermal drift.

3.2.5 Gas-Density Dependence Compressed gas standard capacitors can have an additional source of error associated with gas leakage. Values of $\partial C/\partial P$ (to first order in pressure) measured at a temperature of 22.8 °C are shown in table 2 for three different gases [6].

Table 2. Gas density dependence

Gas	$\partial C/\partial P$ at T=22.8 °C (units of picofarads/pascal)
SF_6	$(2.012\pm0.022)\times10^{-6}+[(5.1\pm0.6)\times10^{-13}]P$
CO_2	$(0.903\pm0.015)\times10^{-6}+[(1.4\pm0.4)\times10^{-13}]P$
He	$(0.075\pm0.004)\times10^{-6}+[(0.2\pm0.1)\times10^{-13}]P$

The gas pressure, P, is in units of pascals and the capacitance in picofarads. For a 100-pF capacitor with SF_6 as the dielectric gas, a 1-psi (6900-Pa)

leak would cause the capacitance to decrease by about 140 ppm. It must be stressed that this change is valid only if the pressure change is caused by the loss of gas and not by the lowering of the gas temperature. As can be seen in table 2, the gas density coefficient is largest for SF_6. Clients using compressed gas capacitors for standards might be advised to monitor the gas pressure with a good quality pressure gauge. Leaking SF_6-filled capacitors should be checked often against a good low-voltage standard.

3.3 Voltage Transformers

3.3.1 Information Necessary to Initiate Calibration In order to calibrate a voltage transformer, several different parameters must be specified: frequency; windings and/or range; secondary voltage; and burden or impedance across the secondary winding. In some cases, for example when there is a tertiary winding, additional parameters may be required.

3.3.2 Labeling of Terminals There are some standard conventions as to which of the primary and secondary taps are to be at low or ground potential and which are to be at rated voltage. Some transformers have one tap of the secondary and one tap of the primary winding marked by a "±". These two taps are connected together and to ground potential. Some transformers use the designators H1, H2 for the primary taps, and X1, X2 (and Y1 and Y2 for the transformers with two secondaries) for the secondary taps. Sometimes the secondary winding has a third tap, X3. By convention the primary and secondary taps with the largest number are connected together and to ground. If the client wants some other arrangement, NIST should be notified prior to the calibration.

3.3.3 Load Imposed by NIST Measurement System The basic measurement circuit is shown in figure 5. The two capacitors shown are three-terminal standard capacitors. Their dissipation factors are typically less than 5×10^{-6}. The capacitor connected to the secondary usually has the nominal value of 1000 pF. Therefore, for 60-Hz measurements, the capacitor imposes a negligible load (2.7 MΩ or 0.005 volt-amperes at 120 V) on the voltage transformer. Negligible in this case means that the effect of this burden on the measured ratio and phase angle can not be observed at the ppm level. The digital voltmeter (DVM) in figure 5 has an estimated uncertainty of less than ±0.5% of the reading and measures true-rms ac volts. The internal impedance of the DVM is equal to or greater than one megohm.

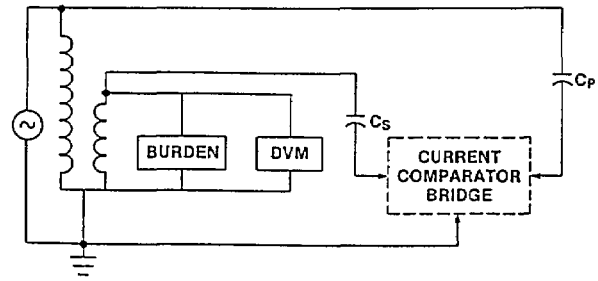

Figure 5. Basic measurement circuit for the calibration of a voltage transformer with a digital voltmeter (DVM) and secondary burden.

3.3.4 Possible Errors Caused by Improper Wiring The wiring of the circuit shown in figure 5 is critical. For example, it is important that the two capacitors be connected directly to the primary and secondary terminals of the transformer. Consider instead figure 6. The capacitor C_s is connected to the burden and the DVM instead of directly to the secondary terminal of the transformer. If the secondary burden were an ANSI standard burden ZZ (36 Ω at 120 V, see table 3) and the resistance of the lead connecting the burden to the transformer were 10 mΩ, the incorrect wiring shown in figure 6 would cause a error in the transformer ratio measurement of about 0.03%. For higher impedance burdens this becomes less of a problem but, in general, one must take precautions to avoid including the voltage drop in the lead connecting the transformer to the burden as part of the voltage on the transformer secondary winding to be measured.

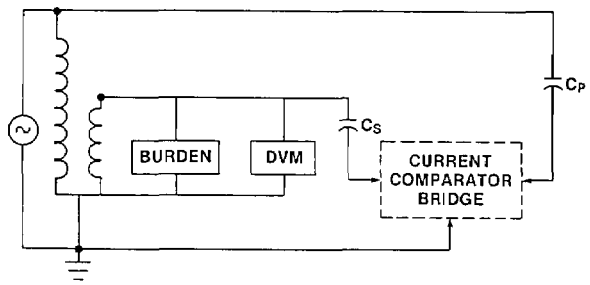

Figure 6. Measurement circuit for the calibration of a voltage transformer. Connection of low-voltage capacitor as shown is incorrect.

Table 3. ANSI standard burdens

ANSI burden	Volt-amperes	Power factor (lagging)
W	12.5	0.10
X	25	0.70
M	35	0.20
Y	7	0.85
Z	200	0.85
ZZ	400	0.85

Another major concern in the measurement of the ratio and phase angle of a voltage transformer is the proper definition of the ground point and the avoidance of ground loops. This can best be illustrated by a few examples. In figure 7, some common mistakes are shown. The transformer is energized in such a manner that significant current is forced to flow between the transformer ground and the circuit ground. The resulting voltage drop in the lead connecting the transformer and ground will be part of the ratio and phase angle measured. The high-voltage capacitor is not connected directly to the primary of the transformer under test. The measurement of the ratio and phase angle, therefore, includes the effect of the voltage drop in the lead between the point where the capacitor is connected to the power source and the transformer. In addition, as there are three different "ground" points in the circuit and it is not, in general, possible to know the voltages and impedances between these points, a measurement error is probable.

In figure 8 the problem has been eliminated by defining the low-voltage terminal of the transformer as ground. Although this point may significantly differ from the building or utility ground, from the measurement point of view this is the correct ground. It is important that the shields of the three-terminal capacitors, the bridge detector ground, and all other measurement grounds each be connected directly to this point.

In figure 5 the preferred method of wiring a voltage transformer calibration circuit is shown. The client's transformer is connected in such a way that the energizing current does not flow between the transformer and the measurement ground. All measurement grounds are connected to the transformer ground point. The two capacitors are connected directly to the primary and secondary terminals of the transformer. Only one ground is used in the circuit. While it is not always possible to connect the transformer as in figure 5, this is the best choice. Otherwise tests are required to ensure that systematic errors are not compromising the measurement results.

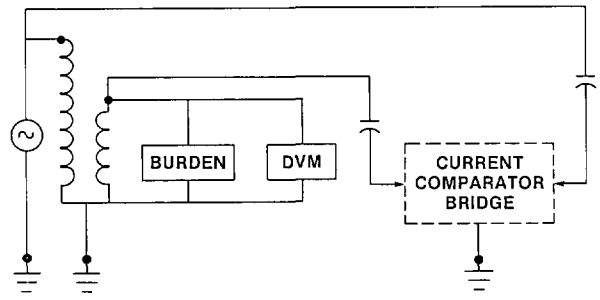

Figure 7. Measurement circuit for the calibration of a voltage transformer. Grounds are poorly defined.

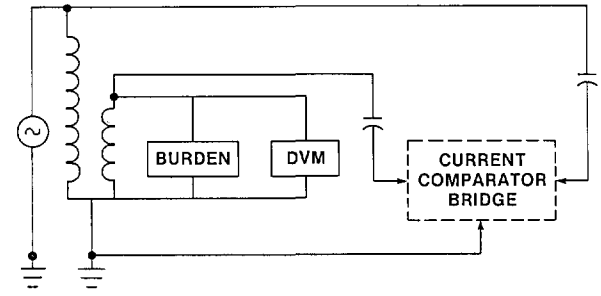

Figure 8. Measurement circuit for the calibration of a voltage transformer. Measurement ground is defined. Transformer excitation current flows from the measurement ground to building ground.

3.3.5 Burdens The burden attached to the secondary of the client's transformer (as shown in fig. 5) is specified by the client. In general this would not be the burden corresponding to the maximum volt-ampere rating of the transformer but instead would be equal to the burden attached to the transformer in its intended use. For example, if the transformer will only have a digital voltmeter attached to its secondary, a calibration with a secondary impedance of one megohm would be more useful than one with an ANSI ZZ burden attached. Since the ANSI burdens are often requested, they are summarized in table 3 [7]. By convention these burdens are defined for a frequency of 60 Hz only.

3.3.6 Substitute Burdens If the client of the service does not send the secondary burden with the transformer, the National Institute of Standards and Technology will provide the burden. It is not practical to have available and adequately characterized all of the anticipated burdens. Fortunately this is not necessary. If the ratio and phase angle of a transformer is known for two different burden values, the ratio and phase angle at any other burden can be calculated (with certain limitations) [8]. A derivation of the formulas relating the ratios and phase angles at zero and some other known burden value are given in the appendix and presented in abbreviated form below.

The voltage transformer will be represented as an ideal transformer with some unknown series output impedance Z_0, as shown in figure 9. The model has been shown to be sufficiently accurate experimentally. The relationship between the input voltage E_i, and the output voltage with zero burden E_0, is:

$$\frac{E_i}{E_0} = N\,RCF_0 e^{-j\Gamma_0} = \left|\frac{E_i}{E_0}\right| e^{-j\Gamma_0}, \qquad (5)$$

where N is the nominal (or turns) ratio of the transformer, RCF is the ratio-correction factor ($N \times RCF$ = actual ratio) at zero burden, Γ_0 is the angle by which the secondary voltage vector leads the primary voltage vector and $j=\sqrt{-1}$. A similar relationship exists between the input voltage E_i, and the output voltage E_c, with secondary burden C (having impedance Z_c) shown in figure 10:

$$\frac{E_i}{E_c} = N\,RCF_c e^{-j\Gamma_c}, \qquad (6)$$

where RCF_c is the ratio correction factor with secondary burden C and Γ_c is the corresponding phase angle. If the transformer is measured at zero burden (RCF_0 and Γ_0) and at burden T (RCF_t and Γ_t), the ratio correction factor and phase angle at burden C are approximately given by:

$$RCF_c \approx RCF_0 + \frac{B_c}{B_t}[(RCF_t - RCF_0)\cos(\theta_t-\theta_c) + (\Gamma_t-\Gamma_0)\sin(\theta_t-\theta_0)], \qquad (7)$$

where $B_c = 1/Z_c$ is the burden in Ω^{-1} of the impedance Z_c, and

$$\Gamma_c \approx \Gamma_0 + \frac{B_c}{B_t}[(\Gamma_t-\Gamma_0)\cos(\theta_t-\theta_c) - (RCF_t - RCF_0)\sin(\theta_t-\theta_c)]. \qquad (8)$$

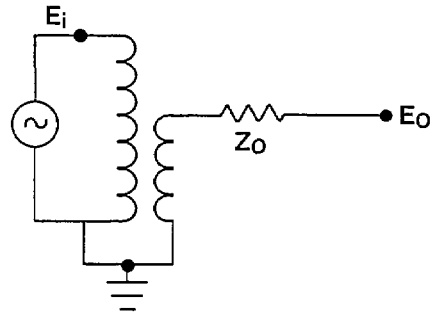

Figure 9. Equivalent circuit of a voltage transformer.

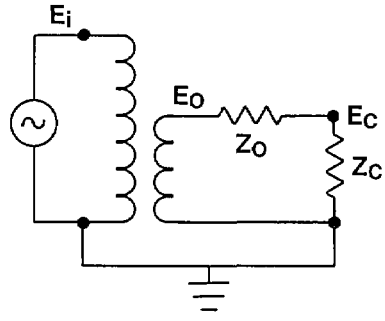

Figure 10. Equivalent circuit of a voltage transformer with secondary burden Z_c.

The power factor of burden C is $\cos\theta_c$, RCF_c is the ratio correction factor calculated for burden C, and Γ_c is the angle by which the secondary voltage leads the primary voltage for burden C.

Equations (7) and (8) can be used to calculate the RCF and phase angle for some secondary burden, C, if the ratio correction factors and phase angles are known at some other burden T, and at zero burden. In practice, at NIST, capacitive burdens are used for the "T" or known burdens in eqs (7) and (8). The main reason is their stability. The heat generated in a large resistive burden, for example, is likely to cause the burden's impedance value to vary. Capacitors, in addition, are compact so even the ZZ burden in table 3 is easy to handle. At NIST, capacitive burden boxes have been constructed in a binary layout (fig. 11) so that capacitors from 1 to 32 μF can be switched in and out allowing any capacitance value from zero to 63 μF. Since a ZZ burden is equivalent to a 74 μF capacitor at 120 V, two such burden boxes are sufficient for nearly all the calibrations at NIST.

Several approximations were made to derive eqs (7) and (8). The approximations relate to the relative ratio of the transformer's output impedance Z_0 to the impedance of the secondary burden Z_t or Z_c.

The smaller this ratio, the more accurate are eqs (7) and (8). This ratio also affects the differences, $RCF_t - RCF_0$ and $\Gamma_t - \Gamma_0$. If the ratio correction factor difference is 0.001 or less, and if the phase angle difference is 1 mrad or less than eqs (7) and (8) should be accurate to within ± 10 ppm for the ratio correction factor and to within ± 10 μrad for the phase angle if it is assumed that the ratio of the burdens is known with no more than ± 1 percent uncertainty. Data over the years has indicated that eqs (7) and (8) are always at least that accurate. In order to identify any problems, an extra measurement is made at a different secondary burden to test the predictive capabilities of eqs (7) and (8) for the transformer under test. If a problem is discovered, the error budget is adjusted accordingly.

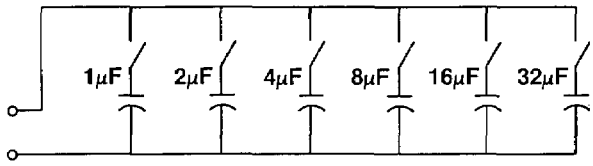

Figure 11. Capacitive burden box.

The above discussion might enable clients of the voltage transformer calibration service to better design their calibration requests. Using eqs (7) and (8), the client might be able to reduce the number of measurements required. A note of caution is in order. It is likely that using a zero burden result and a 10 volt-ampere burden result to predict the transformer's behavior at a ZZ burden may lead to large inaccuracies. The reasons are twofold. First, the differences $RCF_t - RCF_0$ and $\Gamma_t - \Gamma_0$ are likely to be small for a burden as small as 10 volt-amperes and extrapolations can cause large errors. The second reason can be seen from figure 10. The higher current of the ZZ burden will cause Z_0 to heat up and increase in value, leading to errors if eqs (7) and (8) are used. Somewhat better results are likely if one uses a ZZ burden result to predict a transformer's behavior at 10 volt-amperes. However, it is best to choose burden T to have a volt-ampere rating the same order of magnitude as the burden of interest C. Also, the values in eqs (7) and (8) are all to be measured at the same frequency and at the same secondary voltage.

3.3.7 Harmonic Effects The measurement of the ratio and phase angle of a voltage transformer can be affected by the presence of harmonics in the voltage waveform. If a tuned null detector is not used, the balance of a bridge circuit can be difficult in the presence of harmonics and often a precise balance is not possible resulting in increased measurement uncertainties. Harmonics can also lead to errors in measuring the magnitude of the secondary voltage. For example, if an average reading, rms scaled voltmeter measured a 100-V rms fundamental with an in-phase 3-V rms third harmonic, the meter would read 101 V. Setting the voltage to read 100 V on the meter would result in a 1-V discrepancy between the intended and actual voltage. Many transformers have large enough voltage coefficients for this 1-V error in the voltage setting to have a non-negligible effect on the measured ratio correction factor and phase angle. If instead, a true rms voltmeter were used to measure this signal, the measured voltage would be 100.045 V and the resulting error would be negligible. At NIST three different steps are taken to lessen the effects of harmonics. The first is to try to minimize the harmonic content of the power supply. The supply used for most of the calibrations has a total harmonic distortion of order 0.2% of the fundamental. Second, a tuned detector is used to assure that the balance conditions are for the fundamental component of the voltage waveform. And third, all voltage measurements are made with true-rms voltmeters.

3.3.8 Voltage Dependence of Standard Capacitor An additional measurement concern is the voltage coefficient of the high-voltage standard capacitor shown in figure 5. Although no absolute measurements are required to calibrate a voltage transformer, the ratio of the two standard capacitors must be known. The problem is that the low-voltage standard capacitor typically has a maximum voltage rating of 500 V, and both the primary of the transformer and the high-voltage standard capacitor might be energized to 100 kV. Since the capacitor ratio measurement must be done at less than 500 V, the voltage dependence of the high-voltage capacitor is important. This problem was discussed in section 3.2.

4. Measurement Instrumentation

The calibration of voltage transformers and high-voltage capacitors at NIST requires the combined use of standard capacitors and the current comparator bridge. Standard capacitors have been thoroughly discussed in the literature [5, 6, 9,]. The care that must be taken with their use in these types of measurements has been discussed above. The current comparator bridge will be discussed in this section.

The current comparator bridge can be thought of as a voltage comparator transformer arm bridge in which the detector and power source have been interchanged. Traditionally, the disadvantage of the current comparator bridge versus the voltage comparator bridge is the signal-to-noise level. For high-voltage measurement applications, this is no longer a problem. Kusters and Petersons were the first to develop this bridge for the comparison of two capacitors at high voltage [3]. A basic current comparator bridge is shown in figure 12. The current in the unknown capacitor, C_x, is balanced against the current in the standard capacitor, C_s, by varying the turns ratios, N_s and N_x.

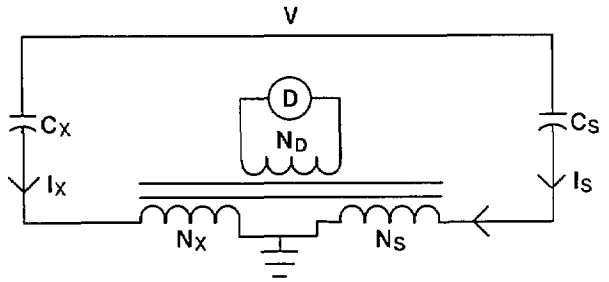

Figure 12. Basic current comparator bridge.

Balance is achieved when the signal at the detector D is equal to zero. At balance $I_xN_x=I_sN_s$ or:

$$V2\pi fC_xN_x=V2\pi fC_sN_s, \qquad (9)$$

where f is the frequency. This balance equation can also be expressed as:

$$C_x=\frac{N_s}{N_x}C_s \qquad (10).$$

The bridge shown in figure 12 has no means of balancing the in-phase current resulting from a non-ideal unknown capacitor C_x. The current comparator in figure 13 does have the capability of balancing both the in-phase and quadrature components of the capacitive current. The difficulty with the approach used in figure 13 is that the applied high voltage is across the variable resistance R_s. It is nearly impossible to design a stable high-voltage variable resistor with negligible phase angle. Another means is necessary to balance the in-phase current, preferably at low voltage using well-characterized components.

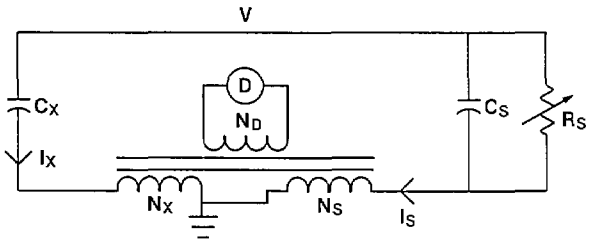

Figure 13. Current comparator bridge with high-voltage resistor for in-phase current balance.

The current comparator shown in figure 14 provides a satisfactory means of achieving both the in-phase and quadrature current balances. The quadrature current balance is identical to that in figures 12 and 13 above. The in-phase current balance is accomplished at low voltage with the aid of an operational amplifier. The current from the standard capacitor, after passing through the N_s winding, goes to the inverting input of the operational amplifier. This point is at virtual ground so the capacitive current balance, eq (10), is not affected. The feedback capacitor C_f causes the output voltage of the operational amplifier to be a small fraction (C_s/C_f where C_f is approximately 10 μF) of the applied voltage and π radians out of phase with it. The inductive voltage divider allows a known fraction, α, of this output signal to be applied across a standard resistor R. As can be seen from figure 14, the signal is first inverted before the resistor in order to have the correct phase relationship with the unknown in-phase current.

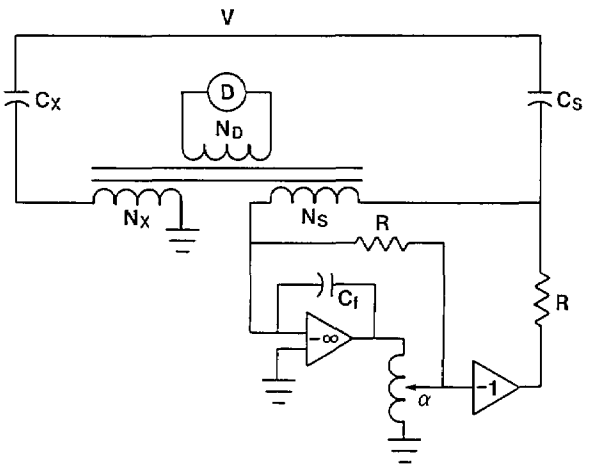

Figure 14. Current comparator with superior in-phase current balance.

It is necessary that the non-inverted signal be applied to an identical standard resistor as shown in figure 14 so that the current from the standard winding N_s reaching the operational amplifier has no phase defect. The in-phase current into the standard winding N_s is then equal to:

$$I_{in} = \frac{(\alpha V C_s / C_f)}{R} \tag{11}$$

Since the quadrature current $I_{out} = V 2\pi f C_s$, the dissipation factor is:

$$DF = \frac{I_{in}}{I_{out}} = \frac{\alpha V C_s}{2\pi f R V C_f C_s} \tag{12}$$

or

$$DF = \frac{\alpha}{2\pi f R C_f}. \tag{13}$$

The resistor R can be chosen so that α is direct reading in percent or milliradians.

In some cases, particularly for larger capacitors, it is necessary to make a four-terminal measurement. This is required when the lead and winding impedances become a significant fraction of the impedance to be measured. Figure 15 shows a current comparator bridge with this capability. Because of the non-negligible lead and winding impedance, there is some voltage e at the low-voltage terminal of the capacitor. This voltage signal is inverted as shown in figure 15 and connected to the N_s winding through a capacitor $C_{s'}$. The current through the unknown capacitor is:

$$I_x = j2\pi f(V-e)C_x. \tag{14}$$

The current reaching the N_s winding is:

$$I_s = j2\pi V C_s - j2\pi f e C_{s'}. \tag{15}$$

If $C_{s'}$ is adjusted prior to the measurement to be equal to C_s then eq (15) reduces to:

$$I_s = j2\pi f(V-e)C_s. \tag{16}$$

Comparing this with eq (14), the effect of the compensation circuit has been to place the same voltage across both the standard and unknown capacitors. This is exactly what is required for lead compensation.

Figure 16 shows the last enhancement of the bridge to be discussed. The National Institute of Standards and Technology's current comparator bridge has an internal range of 1000:1 (i.e., the maximum value of N_d/N_x is 1000). The external current transformer shown in figure 16, referred to as a range extender, increases the measurement range by a factor of 1000 allowing the comparison of two currents differing in magnitude by as much as a factor of a million. As with the transformers internal to the current comparator bridge, the accuracy requirements on the range extender are quite stringent. Further details on the design of a ppm current comparator and the specifics of NIST's current comparator bridge are available in the literature [10, 11].

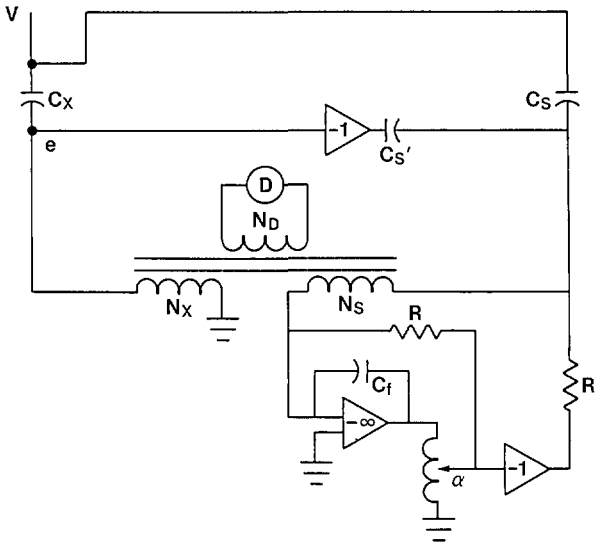

Figure 15. Current comparator bridge modified for four-terminal capacitance measurements.

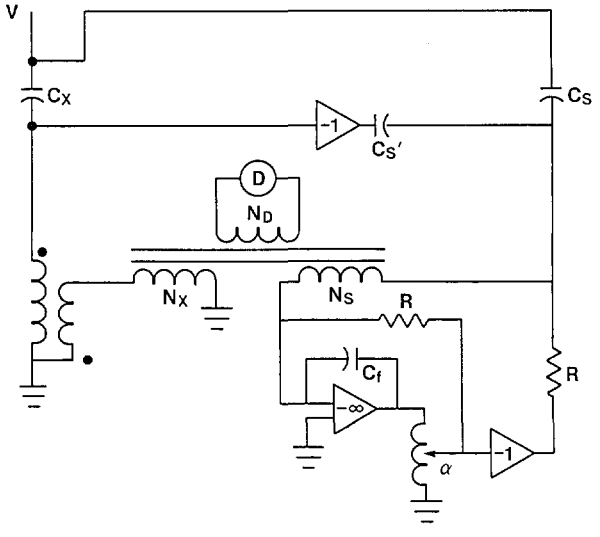

Figure 16. Current comparator bridge with external range extender.

The current comparator bridge is quite straightforward to use and has proven to be rugged in practice. In order to monitor the behavior of NIST's current comparator bridge, a check standard is maintained. In this case, the check standard consists of two high quality standard capacitors. The ratio of the two capacitors is measured quarterly. For the last 8 years, this ratio has been stable to within about 20 ppm as can be seen in table 4.

Table 4. Check standard history

Date	Capacitance ratio	Date	Capacitance ratio
6/80	1.000025	10/84	1.000032
6/81	1.000028	4/85	1.000041
9/81	1.000027	6/85	1.000042
1/82	1.000027	10/85	1.000041
4/82	1.000026	12/85	1.000042
7/82	1.000026	1/86	1.000041
9/82	1.000028	5/86	1.000044
1/83	1.000030	7/86	1.000044
3/83	1.000031	10/86	1.000044
6/83	1.000033	2/87	1.000044
8/83	1.000031	7/87	1.000046
12/83	1.000031	12/87	1.000044
1/84	1.000032	4/88	1.000040
5/84	1.000033	11/88	1.000046

The drift can readily be attributed to the two capacitors. The 9 ppm change between 10/84 and 4/85 occurred apparently after one of the capacitors had been used for another purpose. An independent measurement of that capacitor verified the change. While the use of this check standard cannot prove that the bridge is still working to the ppm level, it can alert the user of changes large enough to affect calibration results. Of course, since the two capacitive currents are largely balanced using stable passive components (i.e., transformer windings), one expects that the bridge should be stable. It should be noted that if a transformer winding were to become open or short circuited the result would be dramatic and readily observed by the operator.

The situation with the dissipation factor (or in-phase current) balance is different as active components play an important role. Also, it is difficult to design a stable dissipation factor standard to act as a check standard. This problem has been overcome by using the circuit in figure 17. Standard capacitors are connected to the standard and unknown sides of the bridge. The known in-phase current is applied with the use of the inductive voltage divider and a resistor as shown. The advantage of this circuit is that the voltage across the resistor is small (~0.3 V). However, because of the small voltage, any error voltage, ϵ, at the low side of the resistor, R, becomes important. The in-phase current entering the N_x winding is:

$$I_{in} = \frac{\alpha V - \epsilon}{R}, \tag{17}$$

where α is the ratio of the inductive voltage divider ($\alpha \ll 1$). The dissipation factor I_{in}/I_{out} is then equal to:

$$DF = \left[\frac{\alpha V - \epsilon}{(V-\epsilon) R 2\pi f C_x} \right]. \tag{18}$$

The effect of ϵ can be significant at the ppm level and needs to be eliminated. The circuit in figure 18 is identical to that in figure 17 except that the input of the inductive voltage divider is grounded. The dissipation factor in this case is then:

$$DF_0 = \left[\frac{-\epsilon}{(V-\epsilon) R 2\pi f C_x} \right]. \tag{19}$$

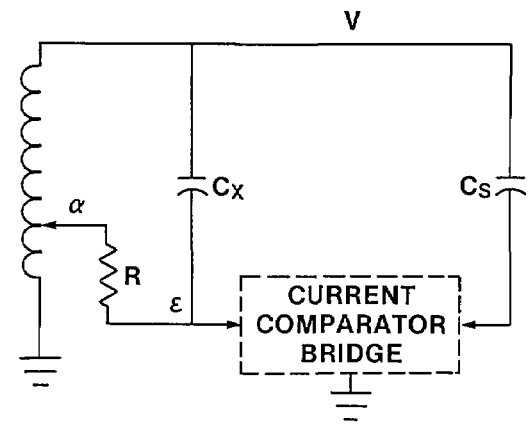

Figure 17. Circuit for checking operation of dissipation factor measurement of current comparator bridge.

Since $\epsilon \ll V$ subtracting eq (19) from eq (18) one obtains:

$$DF_m = DF - DF_0 = \frac{\alpha}{2\pi f R C_x}. \tag{20}$$

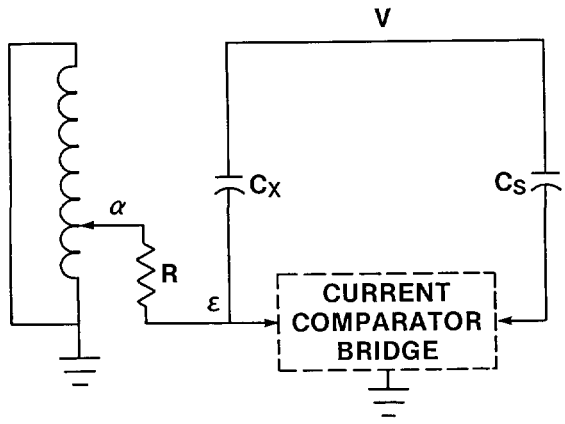

Figure 18. Circuit for checking operation of dissipation factor measurement of current comparator bridge. Input is grounded in order to measure ε in eq (18).

At NIST typical values of α are 0.003, 0.0003, −0.0003, −0.003. With a 1 MΩ resistor and a 1000-pF standard capacitor this enables a near full scale test of the dissipation factor on its four ranges. Recent results are shown in table 5. The dissipation factor values are all in units of percent.

Agreement between the calculated values in eq (20) and the corrected measurement DF_m (the last two columns) are well within ±0.2% of the measured value. This check is performed at approximately 6-month intervals.

It is further proposed that an additional check standard be obtained and measured quarterly. Specifically, a voltage transformer measured regularly at a ratio of 10:1 would give an additional check on the phase angle circuitry and on the bridge windings at something other than a 1:1 ratio.

5. Measurement Uncertainties

5.1 Voltage Transformers

The records of the National Institute of Standards and Technology show examples of voltage transformers that have been calibrated at 5-year intervals over a period of 30 to 40 years. Invariably the original uncertainty statement covers any variation in ratio correction factor and phase angle observed over this period of time. Voltage transformers are often used by the client in conjunction with other equipment to measure some quantity. For example, used with a current transformer and watthour meter, a voltage transformer can help provide a measure of the energy consumed by a large power transformer. Thus it is important to the clients of this calibration service to

Table 5. Dissipation factor check standard

Date	α	Measured (DF)	Correction (DF_0)	Corrected (DF_m)	Theoretical ($\alpha/2\pi fRC_x$)
7/82	0.0003	0.08003	0.0002	0.07983	0.07977
	0.003	0.7982	0.0002	0.7980	0.7977
	−0.003	−0.7979	0.0002	−0.7981	−0.7977
	−0.0003	−0.07959	0.0002	−0.07979	−0.07977
3/83	0.0003	0.08135	−0.00014	0.08149	0.08147
	0.003	0.81455	−0.00015	0.8147	0.8147
	−0.003	−0.81475	−0.00015	−0.8146	−0.8147
	−0.0003	−0.08160	−0.00014	−0.08146	−0.08147
10/83	0.0003	0.07952	−0.0001	0.07962	0.07959
	0.003	0.7959	−0.0001	0.7960	0.7959
	−0.003	−0.7960	−0.0001	−0.7959	−0.7959
	−0.0003	−0.07965	−0.0001	−0.07955	−0.07959
1/84	0.0003	0.08174	0.00029	0.08145	0.08143
	0.003	0.8148	0.00029	0.8145	0.8143
	−0.003	−0.8140	0.00029	−0.8143	−0.8143
	−0.0003	−0.08110	0.00029	−0.08139	−0.08143
5/84	0.0003	0.08090	0.0002	0.08070	0.08071
	0.003	0.8076	0.0002	0.8074	0.8071
	−0.003	−0.8071	0.0002	−0.8073	−0.8071
	−0.0003	−0.08050	0.0002	−0.08070	−0.08071
11/84	0.0003	0.08000	0.0000	0.08000	0.07997
	0.003	0.8000	0.0000	0.8000	0.7997
	−0.003	−0.8000	0.0000	−0.8000	−0.7997
	−0.0003	−0.08000	0.0000	−0.08000	−0.07997
4/85	0.0003	0.08060	0.0000	0.08060	0.08059
	0.003	0.8056	0.0000	0.8056	0.8059
	−0.003	−0.8055	0.0000	−0.8055	−0.8059
	−0.0003	−0.08050	0.0000	−0.08050	−0.08059
12/85	0.0003	0.08070	−0.0001	0.08080	0.08071
	0.003	0.8076	−0.0001	0.8077	0.8071
	−0.003	−0.8076	−0.0001	−0.8075	−0.8071
	−0.0003	−0.08070	−0.0001	−0.08060	−0.08071
11/86	0.0003	0.08029	−0.00022	0.08051	0.08046
	0.003	0.8049	−0.00022	0.8051	0.8046
	−0.003	−0.8054	−0.00022	−0.8052	−0.8046
	−0.0003	−0.08067	−0.00022	−0.08045	−0.08046
7/87	0.0003	0.08031	−0.0002	0.08051	0.08045
	0.003	0.8051	−0.0002	0.8053	0.8045
	−0.003	−0.8055	−0.0002	−0.8053	−0.8045
	−0.0003	−0.08071	−0.0002	−0.08051	−0.08045
12/87	0.0003	0.08060	0.0001	0.08050	0.08039
	0.003	0.8053	0.0001	0.8052	0.8039
	−0.003	−0.8051	0.0001	−0.8052	−0.8039
	−0.0003	−0.08040	0.0001	−0.08050	−0.08039
8/88	0.0003	0.08010	−0.0003	0.08040	0.08030
	0.003	0.8037	−0.0003	0.8040	0.8030
	−0.003	−0.8043	−0.0003	−0.8040	−0.8030
	−0.0003	−0.08070	−0.0003	−0.08040	−0.08030
11/88	0.0003	0.08142	0.0000	0.08142	0.08128
	0.003	0.8140	0.0000	0.8140	0.8128
	−0.003	−0.8140	0.0000	−0.8140	−0.8128
	−0.0003	−0.08135	0.0000	−0.08135	−0.08128

obtain a meaningful uncertainty statement that reflects the contribution the voltage transformer would make to their total error budget.

As mentioned earlier in this paper, voltage transformers calibrated at NIST generally fall into two accuracy classes: ±0.03% uncertainty for ratio correction factor, ±0.3 mrad for phase angle; and ±0.01% for ratio correction factor, ±0.1 mrad for phase angle. While it would be possible in some cases to report smaller uncertainties to the clients by more thorough determinations of such parameters as voltage coefficients, proximity effects, and burden dependencies, the present service provides an economical way to present meaningful error statements to the clients and meets their needs.

The analysis of the uncertainties for the ratio correction factor measurements are summarized in table 6. The units are in ppm. The values in parentheses apply to the higher accuracy voltage transformers described in section 2.1. The uncertainties for the phase angle measurement of voltage transformers are the same as is shown in table 6 except the units are microradians instead of ppm.

Table 6. Contributions to uncertainty

	Uncertainties	
	Random	Systematic
Bridge measurement	±2 (±2)	±75 (±25)
Secondary voltage setting		±50 (±10)
Burden setting		±50 (±10)
Transformer self-heating		±75 (±20)
Capacitance ratio measurement	±2 (±2)	± 5 (± 5)

To calculate the uncertainties reported to the client, the systematic uncertainties tabulated above are algebraically summed and added to three times the root sum of squares of the random uncertainties. The results are shown in table 7.

Table 7. Total estimated uncertainties

Ratio correction factor	±0.03%	(±0.01%)
Phase Angle	±0.3 mrad	(±0.1 mrad)

The values in table 6 are approximate. Some transformers demonstrate stronger voltage dependences than others or stronger burden dependences. In some cases the values in table 7 must be adjusted for such transformers. The purpose of the above tables is to give the users an idea of the sources of errors and how they are used to calculate an uncertainty statement.

Since most of the sources of uncertainty presented in table 6 originate from the transformer under test, NIST could in principle measure a nearly ideal voltage transformer to much better accuracy than shown in table 7. Such a test would be expensive because of the time-consuming care that would be required.

5.2 Capacitors

The National Institute of Standards and Technology has the capability to measure the ratio of two capacitors to an estimated systematic uncertainty of ±1 ppm and $\pm 1\times10^{-6}$ ±1% of the measured value for the relative dissipation factor. The values of the standard capacitors used for these comparisons are known to ±10 ppm for capacitance ($\pm 1\times10^{-6}$ for dissipation factor). The random uncertainty associated with the capacitance measurement is ±1 ppm and $\pm 1\times10^{-6}$ for dissipation factor. Conservatively then, NIST could calibrate a client's capacitor to an overall uncertainty of ±15 ppm in capacitance and $\pm 5\times10^{-6}$ ±1% of the value for dissipation factor. In general, the quoted uncertainty is always larger than this except for low-voltage standard capacitors similar to those used at the National Institute of Standards and Technology. (Low-voltage standard capacitors are in general calibrated elsewhere at NIST. The service described here provides higher voltage calibration of these same capacitors.)

The uncertainty statements for high-voltage standard capacitors and power-factor capacitors depend on the stability of these devices during the course of the NIST measurements. The stability is influenced by both the voltage dependence of the device and self-heating (i.e., the capacitance and dissipation factors vary as the internal energy dissipated heats the device). Self-heating effects are more important for power-factor capacitors. Some power-factor capacitors demonstrate significant hysteresis effects. Assigning an uncertainty statement to these measurements depends on the specific behavior of the capacitor. If self-heating is a problem the calibration report clearly must specify the amount of time the capacitor was energized before the measurement was made. If hysteresis effects are detected they are so noted. Because of the nature of most of these devices, the calibration reports for capacitors usually include a statement of the form: "the estimated uncertainties quoted apply to the above tabulated values and should not be construed as being indicative of the long-term stability of the device under test." This

statement is also important for the compressed gas insulated capacitors whose values might change significantly by handling during shipping.

The actual uncertainty quoted to the client is derived by algebraically summing the systematic uncertainties and adding three times the root mean sum of squares of the random uncertainties. For the capacitance measurement of compressed gas insulated capacitors, the measurement uncertainty will include a 20 ppm contribution because of the possible 1 K variation in temperature of the NIST voltage transformer laboratory. For power-factor capacitors the self-heating variations will dominate ambient temperature effects.

6. Appendix

The voltage transformer will be represented as an ideal transformer with some unknown series output impedance Z_0, as shown in figure 9. The model has been shown to be sufficiently accurate experimentally. The relationship between the input voltage E_i and the output voltage with zero burden E_0 is:

$$\frac{E_i}{E_0} = N\,RCF_0 e^{-j\Gamma_0}, \tag{21}$$

where N is the nominal (or turns) ratio of the transformer, RCF_0 is the ratio-correction factor ($N \times RCF_0$=actual ratio) at zero burden, Γ_0 is the angle by which the secondary voltage vector leads the primary voltage vector, and $j=\sqrt{-1}$. A similar relationship exists between the input voltage E_i and the output voltage E_c, with secondary burden C (having impedance Z_c) shown in figure 10:

$$\frac{E_i}{E_c} = N\,RCF_c e^{-j\Gamma_c} \tag{22}$$

where RCF_c is the ratio correction factor with secondary burden C and Γ_c is the corresponding phase angle.

Equating the current through Z_0 and Z_c in figure 10, one obtains

$$\frac{E_0-E_c}{Z_0} = \frac{E_c}{Z_c} \tag{23}$$

or

$$E_c = \frac{E_0 Z_c}{Z_0+Z_c}. \tag{24}$$

This can be rewritten in the following form:

$$\frac{E_i}{E_c} = \frac{E_i}{E_0}\left(1+\frac{Z_0}{Z_c}\right). \tag{25}$$

Setting Z_0 equal to R_0+jX_0 and Z_c equal to R_c+jX_c, eq (25) becomes:

$$\frac{E_i}{E_c} = \frac{E_i}{E_0}\left[1+\frac{R_0+jX_0}{R_c+jX_c}\right]. \tag{26}$$

Taking the absolute value of both sides of eq (26), one finds that:

$$\left|\frac{E_i}{E_c}\right| \approx \left|\frac{E_i}{E_0}\right|\left[1+\frac{R_0R_c+X_0X_c}{R_c^2+X_c^2}\right], \tag{27}$$

where it has been assumed that both R_0 and X_0 are much less than Z_c so that terms of order $[(R_0R_c+X_0X_c)/(R_c^2+X_c^2)]^2$ and higher have been neglected. Using eqs (21) and (26), one obtains

$$\frac{E_i}{E_c} = \left|\frac{E_i}{E_0}\right| e^{-j\Gamma_0}\left[1+\frac{R_0+jX_0}{R_c+jX_c}\right] \tag{28}$$

or

$$\frac{E_i}{E_c} = \left|\frac{E_i}{E_0}\right| e^{-j\Gamma_0}\left[1+\frac{(R_0+jX_0)(R_c-jX_c)}{R_c^2+X_c^2}\right]. \tag{29}$$

This can also be expressed as

$$\left|\frac{E_i}{E_c}\right| e^{-j\Gamma_c} = \left|\frac{E_i}{E_0}\right| e^{-j\Gamma_0}[\ldots]. \tag{30}$$

Both exponentials have arguments much less than one so that discarding quadratic and higher order terms and equating the imaginary components of the left and right sides of eq (10) one obtains

$$\left|\frac{E_i}{E_c}\right|\Gamma_c \approx \left|\frac{E_i}{E_0}\right|\left[\Gamma_0+\frac{X_cR_0-X_0R_c}{R_c^2+X_c^2}\right] \tag{31}$$

or from eq (5) assuming $Z_0 \ll Z_c$

$$\Gamma_c \approx \Gamma_0 - \frac{X_0R_c-X_cR_0}{R_c^2+X_c^2}. \tag{32}$$

The resistive and reactive components of the burden C can be expressed as

$$R_c = \sqrt{R_c^2+X_c^2}\cos\theta_c \tag{33}$$

and

$$X_c = \sqrt{R_c^2+X_c^2}\sin\theta_c, \tag{34}$$

where $\cos\theta_c$ is the power factor of the burden C. From eqs (21) and (22)

$$\left|\frac{E_i}{E_0}\right| = N\,RCF_0 \tag{35}$$

and

$$\left|\frac{E_i}{E_c}\right| = N\,RCF_c. \tag{36}$$

Using eqs (27) and (33)–(36) one obtains

$$RCF_c = RCF_0\left[1+\frac{1}{|Z_c|}(R_0\cos\theta_c + X_0\sin\theta_c)\right]. \quad (37)$$

For the purposes of this discussion, it will be assumed that burden C (having impedance Z_c) above is the burden for which the ratio correction factor and phase angle are to be calculated. The ratio-correction factor and phase angle must be known for some other burden T, which shall be designated as having impedance Z_t. Using eq (25) and substituting burden T for burden C:

$$Z_0 = \left[\frac{E_i/E_t}{E_i/E_0} - 1\right] Z_t . \quad (38)$$

or using eq (22)

$$Z_0 = Z_t[RCF_t e^{-j\{\Gamma_t - \Gamma_0\}} - RCF_0]/RCF_0 . \quad (39)$$

Neglecting second order and higher terms

$$Z_0 \approx Z_t[RCF_t - RCF_0 + j(\Gamma_0 - \Gamma_t)]/RCF_0 . \quad (40)$$

Using the facts that

$$Z_t = |Z_t|(\cos\theta_t + j\sin\theta_t) \quad (41)$$

and

$$Z_0 = R_0 + jX_0 , \quad (42)$$

one finds

$$R_0 \approx \left(\frac{|Z_t|}{RCF_0}\right)[(RCF_t - RCF_0)\cos\theta_t + (\Gamma_t - \Gamma_0)\sin\theta_t] \quad (43)$$

and

$$X_0 \approx \left(\frac{|Z_t|}{RCF_0}\right)[(\Gamma_0 - \Gamma_t)\cos\theta_t + (RCF_t - RCF_0)\sin\theta_t] . \quad (44)$$

Using eqs (37), (43), and (44) and the relations:

$$\cos\theta_c\cos\theta_t + \sin\theta_c\sin\theta_t = \cos(\theta_t - \theta_c) \quad (45)$$

$$\cos\theta_c\sin\theta_t - \sin\theta_c\cos\theta_t = \sin(\theta_t - \theta_c) \quad (46)$$

one finds

$$RCF_c \approx RCF_0 + \left(\frac{B_c}{B_t RCF_0}\right)[(RCF_t - RCF_0)\cos(\theta_t - \theta_c) + (\Gamma_t - \Gamma_0)\sin(\theta_t - \theta_c)] \quad (47)$$

or

$$RCF_c \approx RCF_0 + \left(\frac{B_c}{B_t}\right)[(RCF_t - RCF_0)\cos(\theta_t - \theta_c) + (\Gamma_t - \Gamma_0)\sin(\theta_t - \theta_c)], \quad (48)$$

where $B_c = 1/Z_c$ is the burden in Ω^{-1} of the impedance Z_c. Since the second term in eq (47) represents a small correction to the first and since RCF_0 is approximately equal to one, RCF_0 has been dropped from the second term of eq (48). Using eqs (32)—(34)

$$\Gamma_c \approx \Gamma_0 - \frac{1}{|Z_c|}(X_0\cos\theta_c - R_0\sin\theta_c) . \quad (49)$$

Using eqs (43)—(46) and (49)

$$\Gamma_c \approx \Gamma_0 + \left(\frac{B_c}{B_t RCF_0}\right)[(\Gamma_t - \Gamma_0)\cos(\theta_t - \theta_c) - (RCF_t - RCF_0)\sin(\theta_t - \theta_c)] \quad (50)$$

or

$$\Gamma_c \approx \Gamma_0 + \left(\frac{B_c}{B_t}\right)[(\Gamma_t - \Gamma_0)\cos(\theta_t - \theta_c) - (RCF_t - RCF_0)\sin(\theta_t - \theta_c)] \quad (51)$$

since RCF_0 is approximately equal to one.

Equations (48) and (51) can be used to calculate the RCF and phase angle for some secondary burden C, if the ratio correction factors and phase angles are known at some other burden T, and at zero burden.

7. Acknowledgments

The author would like to thank Oskars Petersons, Chief of the Electrosystems Division, who has been the source of nearly all the author's knowledge on the calibration of voltage transformers and capacitors. The author would also like to acknowledge the work of Barbara Frey and Roberta Cummings who helped prepare this manuscript. Last, but certainly not least, the author would like to acknowledge both the "old-timers" here at the National Institute of Standards and Technology, who began the tradition of excellence in measurements, and the present calibration staff who are attempting to carry on this tradition under vastly different constraints.

About the author: William E. Anderson is a physicist in the Electrosystems Division of the NIST Center for Electronics and Electrical Engineering.

8. References

[1] Harris, F. K., Electrical Measurements, John Wiley & Sons, New York (1966) pp. 576–577.
[2] Harris, F. K., Electrical Measurements, John Wiley & Sons, New York (1966) pp. 687–738.
[3] Kusters, N. L., and Petersons, O., Trans. Commun. Electron. (U.S.) CE-82 606 (1963).
[4] McGregor, M. C., Hersh, J. F., Cutkosky, R. D., Harris, F. K., and Kotter, F. R., Trans. on Instrum. (U.S.) I-7 No. 3 and 4 (1958).
[5] Hillhouse, D. L., and Peterson, A. E., IEEE Trans. Instrum. Meas. (U.S.) IM-22 406 (1973).
[6] Anderson, W. E., Davis, R. S., Petersons, O., and Moore, W. J. M., IEEE Trans. Power Appar. Syst. (U.S.) PAS-97 1217 (1973).
[7] IEEE Standard Requirements for Instrument Transformers, American National Standards Institute, ANSI/IEEE C57.13-1978 32 (1978).
[8] IEEE Standard Requirements for Instrument Transformers, American National Standards Institute, ANSI/IEEE C57.13-1978 45 (1978).
[9] Harris, F. K., Electrical Measurements, John Wiley & Sons, New York (1966) pp. 673–687.
[10] Petersons, O., and Anderson, W. E., IEEE Trans. Instrum. Meas. (U.S.) IM-24 4 (1975).
[11] Petersons, O., A Wide-Range High-Voltage Capacitance Bridge with One PPM Accuracy, D.Sc. dissertation, School of Engineering and Applied Sciences, George Washington University, Washington, DC (1974).

Volume 94, Number 3, May–June 1989
Journal of Research of the National Institute of Standards and Technology

Consensus Values, Regressions, and Weighting Factors

Volume 94 Number 3 May–June 1989

Robert C. Paule and John Mandel

National Institute of Standards and Technology, Gaithersburg, MD 20899

An extension to the theory of consensus values is presented. Consensus values are calculated from averages obtained from different sources of measurement. Each source may have its own variability. For each average a weighting factor is calculated, consisting of contributions from both the within- and the between-source variability. An iteration procedure is used and calculational details are presented. An outline of a proof for the convergence of the procedure is given. Consensus values are described for both the case of the weighted average and the weighted regression.

Key words: components of variance (within- and between-groups); consensus values; convergence proof; Taylor series; weighted average; weighted least squares regression.

Accepted: February 10, 1989

1. Introduction

The problem of computing consensus values when the errors of measurement involve both internal (within group) and external (between group) components has been discussed in a number of papers [1–4]. The present authors have studied the case of a simple weighted average, as well as that in which the measured quantity y is a linear function of a known variable x.

In the present paper we extend our results to cases in which the error standard deviations are functions, of known form, of the x-variables. We also provide an outline of a proof for convergence of the iterative process described in reference [1].

While our procedure is entirely reasonable, and results in acceptable values, we have no mathematical proof that the weights, which we calculate from the data, are optimal in any well-defined theoretical sense. The problem has been recognized in the literature [5], but we know of no attempt to provide the proof of optimality.

2. Review

If ω_i denotes the weight (reciprocal variance) of a quantity, $\bar{Y}_i$, then the general equation for a weighted average is:

$$\bar{Y} = \frac{\sum_{i=1}^{m} \omega_i \bar{Y}_i}{\sum_{i=1}^{m} \omega_i}. \quad (1)$$

If $\bar{Y}_i$ equals the average of n_i results from group i ($i=1$ to m), then

$$\mathrm{Var}\,(\bar{Y}_i) = \frac{\sigma_{w_i}^2}{n_i} + \sigma_b^2,$$

where

σ_{w_i} = the component of standard deviation within group i (the σ_{w_i} value can be estimated from the n_i results within each group)

σ_b = the component of standard deviation between groups.

Then the weight ω_i of $\bar{Y}_i$ is equal to:

$$\omega_i = \frac{1}{\text{Var}\,(\bar{Y}_i)} = \frac{1}{(\frac{\sigma_{wi}^2}{n_i} + \sigma_b^2)}. \quad (2)$$

The weight equation, $\omega_i = 1/\text{Var}(\bar{Y}_i)$, yields:

$$\omega_i \text{Var}(\bar{Y}_i) = 1$$

or

$$\text{Var}(\sqrt{\omega_i}\ \bar{Y}_i) = 1\,.$$

Generally, all σ-values, and consequently the ω_i values are unknown. The σ_{w_i} can be estimated (as s_{w_i}) from the replicate measurements. We derive an estimate for σ_b^2 and consequently for the ω_i by using the quantity

$$\text{Var}\,(\sqrt{\omega_i}\ \bar{Y}_i) = \frac{\sum_{i=1}^{m} \omega_i (\bar{Y}_i - \tilde{Y})^2}{m-1}$$

which we equate to unity. Thus we have

$$\frac{\sum_{i=1}^{m} \omega_i (\bar{Y}_i - \tilde{Y})^2}{m-1} = 1. \quad (3)$$

Equation (3) is used in "reverse fashion" to estimate the ω_i and $\tilde{Y}$ from the sample data. This is possible if in eq (2), the σ_{w_i} are estimated from the within-group variability, so that the only unknown is σ_b. Note in eq (3) that σ_b is embedded within each weight and therefore within $\tilde{Y}$. The estimated σ_{w_i} and σ_b can also be used to estimate the standard deviation of the weighted average, which is equal to $1/\sqrt{\Sigma\omega_i}$. Henceforth, we use the symbol ω_i for the sample estimate of ω_i.

The same general reasoning holds for the weighted regression case. The variance of a simple weighted average is replaced by the residual mean square from a weighted least squares regression. For a regression with m groups and p coefficients the analogue of eq (3) is

$$\frac{\sum_{i=1}^{m} \omega_i (\bar{Y}_i - \hat{Y}_i)^2}{m-p} = 1, \quad (4)$$

where ω_i is given by eq (2) and $\hat{Y}_i$ is the fitted value.

We now describe the case of a weighted regression with $p=2$. The fitted value $\hat{Y}_i$, for the ith group can be written as follows:

$$\hat{Y}_i = \hat{\alpha} + \hat{\beta} X_i \quad (5)$$

or

$$\hat{Y}_i = \tilde{Y} + \hat{\beta}\,(X_i - \tilde{X})\,, \quad (5')$$

where $\tilde{X}$ is a weighted average analogous to the weighted average described by eq (1), and $\hat{\alpha}$ and $\hat{\beta}$ are weighted least squares estimates of the coefficients, α and β. Again, the only unknown is σ_b, which can now be estimated from sample data by use of eq (4).

A *direct* solution for σ_b in either eq (3) or (4) would be extremely complicated since ω_i, $\tilde{Y}$, and $\hat{Y}_i$ all contain σ_b. The number of terms m, in both equations will vary depending on the number of groups in a particular sample data set. Furthermore, for the regression case, the $\hat{\beta}$ and $\tilde{X}$ also depend on σ_b. Therefore an iterative solution was proposed in reference [1]. This iterative procedure is central to the practical solution of either eq (3) or (4). In order that this paper be self-contained, we briefly review the iterative procedure for the regression case using eq (4) with $p=2$.

3. Iteration Procedure

We define the function:

$$F(s_b^2) = \sum_{i=1}^{m} \omega_i (\bar{Y}_i - \hat{Y}_i)^2 - (m-2)\,. \quad (6)$$

In view of eqs (2) and (4), the estimate s_b^2 of σ_b^2 must be such that $F(s_b^2)=0$. For ease of notation let $s_b^2 = \upsilon$. Start with an initial value, $\upsilon_0 \approx 0$, and calculate an initial set of weights and then evaluate eq (6). In general, $F(s_b^2)$ will be different from zero. It is desired to find an adjustment, $d\upsilon$, such that $F(\upsilon_0 + d\upsilon) = 0$. Using a truncated Taylor series expansion, one obtains:

$$F(\upsilon_0 + d\upsilon) \approx F_0 + \left(\frac{\partial F}{\partial \upsilon}\right)_0 d\upsilon = 0$$

$$\text{and } d\upsilon = -F_0 \Big/ \left(\frac{\partial F}{\partial \upsilon}\right)_0 .$$

Evaluating the partial derivative in this equation, one obtains:

$$d\upsilon = F_0 \Big/ \left[\sum_{i=1}^{m} \omega_i^2 (\bar{Y}_i - \hat{Y}_i)^2\right]_0 . \quad (7)$$

The adjusted (new) value for υ is:

$$\text{New } \upsilon_0 = \text{Old } \upsilon_0 + d\upsilon\,. \quad (8)$$

This new value is now used and the procedure is iterated until $d\upsilon$ is satisfactorily close to zero.

The iterative procedure is easily adapted to the computer. The programming steps are as follows:

1. Evaluate the s_{w_i} from the individual groups of data.
2. Start the iteration process with a value of v_0 just slightly over zero.
3. Evaluate eq (2) to get estimates of ω_i.
4. Fit eq (5) by a weighted least squares regression of $\bar{Y}_i$ on $\bar{X}_i$, and get estimates of the $\hat{Y}_i$.
5. Use eq (6) to evaluate F_0. If $F_0<0$, then stop the iteration and set $v=0$. If not, continue with 6.
6. Use eq (7) to evaluate dv.
7. If dv is positive and small enough to justify stopping, then stop. If it is positive, but is not small enough, repeat steps 3–7 [using the new v_0 from eq (8)].

The consensus values are the final coefficients of the regression equation. One is also interested in the final $v=s_b^2$ value since this is needed to characterize the imprecision of the fit.

For the case of a weighted average [see eq (1)] the above iteration steps are the same, except that in place of step 4, $\tilde{Y}$ is calculated by eq (1), and steps 5 and 6 use $\tilde{Y}$ in place of $\hat{Y}_i$, and unity is used for the p value. The authors have frequently used this procedure for the evaluation of Standard Reference Materials [6].

4. Theoretical Extensions

Once one recognizes the between- as well as the within-group component of variance in the evaluation of consensus values, one can begin to consider functional forms for these components. The within-group component can be of *any* form, and can be easily handled since the appropriate sample values of the component are simply substituted into the weights described by eq (2). Thereafter, this component does not affect the iteration procedure. See for example reference [7], where the within component of variance refers to a Poisson process. The between-group component, however, affects the iteration procedure and must be handled more carefully. As an example, consider the case where the between-group component of standard deviation is believed to be a linear function of the level of X_i:

$$\sigma_b \approx \gamma + \delta X_i \,. \tag{9}$$

Let us assume that we have preliminary estimates, c and d for the γ and δ coefficients. Suppose further that we wish to adjust the estimated value of the variance by a fixed scale factor, say v'. The desired between-group component of variance is thus:

$$s_b^2 = v'(c+dX_i)^2 \,. \tag{10}$$

The weights estimated by eq (2) would then be:

$$\omega_i = \frac{1}{\left(\frac{s_{w_i}^2}{n_i} + v'(c+dX_i)^2\right)} \,. \tag{2'}$$

This newly defined weight can be used in the iteration process. The iteration process proceeds as before, but now the adjustable iteration parameter v' is the *multiplier* needed to make eq (4) true, that is, to make it consistent with the sample data sets. The denominator of eq (7) which is used in iteration step 6 for calculating dv, needs to be slightly modified since the derivative of F with respect to v now contains the function described by eq (10).

$$dv' = \frac{F_0}{\sum_{i=1}^{m} \omega_i^2 (c+dX_i)^2 (\bar{Y}_i - \hat{Y}_i)^2} \,. \tag{7'}$$

All other steps in the iteration process are the same. The final between-group components of variance will be described by eq (10).

5. Example

The iteration process will be used to fit the data of table 1 to a straight line. These are real data taken from a large interlaboratory study for the determination of oxygen in silicon wafers.

Table 1. Data used in example of iteration process

X	Y_1	Y_2	Y_3
0.806	2.83	2.85	
1.429	4.62	5.35	5.01
1.882	6.89	6.66	
2.140	7.56	7.67	
2.256	7.94	7.90	
2.279	8.42	8.12	
2.814	10.04	9.70	10.17
2.957	10.34	10.05	
2.961	11.09	11.07	
3.108	11.63	11.69	
3.124	10.87	11.01	
3.403	12.40	12.22	
3.466	11.94	12.17	12.92
3.530	12.63	12.41	
3.543	12.98	13.27	
3.724	12.95	12.56	
3.836	13.07	13.69	13.56
3.902	14.54	14.19	
4.280	15.59	16.24	
4.770	16.62	16.59	

A preliminary examination of the data indicates that the within error has a constant standard deviation and that the between error has a standard deviation *proportional* to X. Thus, the error structure for the example is given by the equation:

$$\omega_i = \frac{1}{\left(\frac{s_w^2}{n_i} + \upsilon X_i^2\right)},$$

where υ now stands for the product $\upsilon' d^2$ of eq (2').

From the replicates, the pooled within standard deviation is readily calculated to be 0.265. The iteration process then yields the following results

$$\hat{Y}_i = -0.0833 + 3.6085\, X_i$$

$$\begin{cases} s_{\text{within}} = 0.265 \\ s_{\text{between}} = 0.0827 X_i\,. \end{cases}$$

Figures 1a and 1b show, respectively, the standard deviations within, and the residuals ($\bar{Y}_i - \hat{Y}_i$), as functions of X_i.

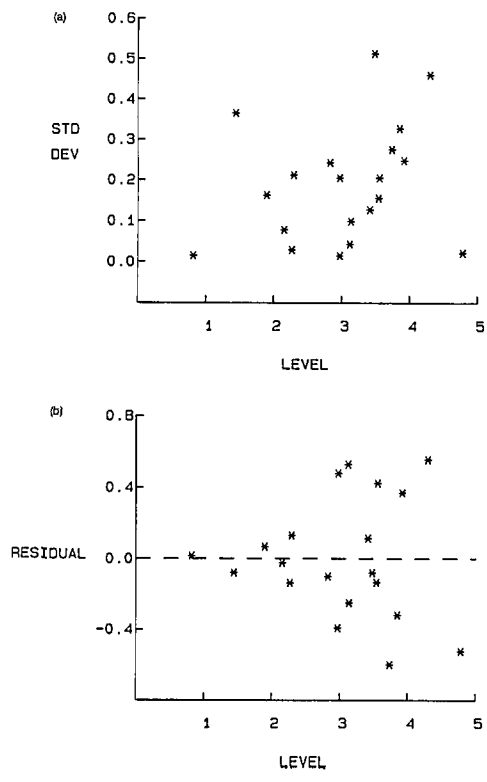

Figure 1. (a) Standard deviations within as a function of X (b) residuals of a function of X.

The figures support the assumpions made concerning the nature of the within and between errors.

6. Appendix

6.1 Sketch of Proof of Convergence

The general functional form of the F of eq (6) is as shown in figure 2a or 2b. It is because of the nature of these forms that convergence always occurs.

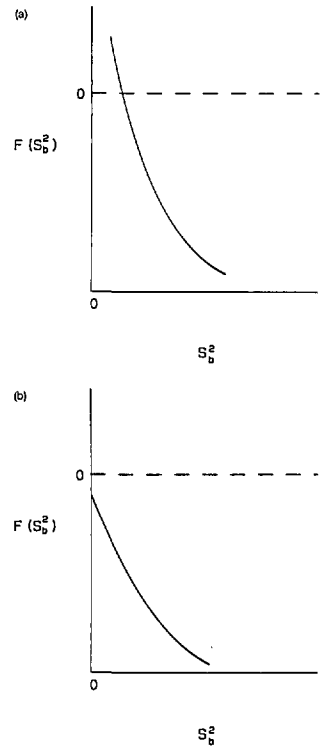

Figure 2. (a) F as a function of s_b^2 where F has a positive root for s_b^2 (b) F as a function of s_b^2 where F does not have a positive root for s_b^2.

If the functional form of F is as shown in figure 2a, the previously described iterative procedure is used to determine the s_b^2 satisfying the equation $F(s_b^2)=0$. If an initial estimate of s_b^2 is chosen that is very slightly above zero, then convergence of the iteration process always occurs. This is a result of the fact that the first derivative of the function F with respect to s_b^2 is negative, and the second derivative is positive. This means that each iteration will undershoot, since the iteration process extrapolates the slope of the F curve at the current s_b^2 estimate to the $F=0$ value. Since each new iteration estimate of s_b^2 is the abscissa value of the inter-

section of the tangent line with the $F=0$ horizontal line, the iteration process will never overshoot and convergence is obtained.

If the form is that of figure 2b, then there will be no positive solutions for the s_b^2 that is associated with the function F. This represents a situation where the variability between the sample groups is less than that expected from the variability within the sample groups. For this situation F_0 is negative and s_b^2 is set to zero (see iteration step 5).

The proof regarding the signs of the first and second derivatives of F with respect to s_b^2 follows. The simple *regression case* will be considered, with the $s_b^2 = v$ being constant. (The extension to the variable s_b^2 case is straightforward.)

6.2 Proof That the First Derivative of F is Negative

An examination of eqs (1), (2), (5′), and (6) shows ω_i and $\hat{Y}_i$ to be functions of s_b^2. Equation 5′ also indicates that $\bar{Y}$, $\bar{X}$, and β are functions of s_b^2. We start with the first derivative of the F of eq (6)

$$\frac{dF}{dv} = \frac{d\left(\sum_{i=1}^{m} \omega_i (\bar{Y}_i - \hat{Y}_i)^2 - (m-2)\right)}{dv}.$$

The derivative of ω_i will frequently be encountered in the following material. At this point, it will be convenient to note its value:

$$\frac{d\omega_i}{dv} = -\omega_i^2 .$$

Continuing, and making use of eq (5′):

$$\frac{dF}{dv} = -\sum_{i=1}^{m} \omega_i^2 (\bar{Y}_i - \hat{Y}_i)^2$$

$$-2\left(\frac{d}{dv}(\bar{Y}_i - \hat{\beta}\bar{X})\right)\sum_i \omega_i (\bar{Y}_i - \hat{Y}_i)$$

$$-2\left(\frac{d\hat{\beta}}{dv}\right)\sum_i \omega_i X_i (\bar{Y}_i - \hat{Y}_i). \qquad \text{(A1)}$$

The last two terms of eq (A1) each contain summations that are equal to zero, so these terms drop out. Next, an examination of the remaining term shows that each product is a positive square, and that the summation is preceded by a minus sign. Thus, the first derivative is negative.

6.3 Proof That the Second Derivative of F is Positive

The evaluation of the second derivative is involved and only an outline of the steps is presented.

$$\frac{d^2F}{dv^2} = \frac{d}{dv}\left[-\sum_{i=1}^{m} \omega_i^2 (\bar{Y}_i - \hat{Y}_i)^2\right],$$

$$\frac{d^2F}{dv^2} = -2\sum_i \omega_i^2 (\bar{Y}_i - \hat{Y}_i)\frac{d(\bar{Y}_i - \hat{Y}_i)}{dv}$$

$$+2\sum_i \omega_i^3 (\bar{Y}_i - \hat{Y}_i)^2, \qquad \text{(A2′)}$$

where

$$\frac{d(\bar{Y}_i - \hat{Y}_i)}{dv} = -\frac{d\bar{Y}}{dv} + \hat{\beta}\frac{d\bar{X}}{dv}$$

$$-(X_i - \bar{X})\frac{d\hat{\beta}}{dv}. \qquad \text{(A3)}$$

Evaluation of the first two derivatives on the r.h.s. of eq (A3) yields:

$$\frac{d\bar{X}}{dv} = -\sum_i \frac{\omega_i^2}{W}(X_i - \bar{X}) \text{ and}$$

$$\frac{d\bar{Y}}{dv} = -\sum_i \frac{\omega_i^2}{W}(\bar{Y}_i - \bar{Y}), \qquad \text{(A4)}$$

where $W \equiv \Sigma\, \omega_i$.

Evaluation of the last derivative of eq (A3) yields:

$$\frac{d\hat{\beta}}{dv} = \frac{d\left[\dfrac{\sum_i \omega_i (X_i - \bar{X})\bar{Y}_i}{\sum_i \omega_i (X_i - \bar{X})^2}\right]}{dv} =$$

$$\sum_{t=1}^{m}\left[\frac{d\left[\dfrac{\sum_i \omega_i (X_i - \bar{X})\bar{Y}_i}{\sum_i \omega_i (X_i - \bar{X})^2}\right]}{d\omega_t}\cdot\frac{d\omega_t}{dv}\right], \qquad \text{(A5′)}$$

where

$$\frac{d\sum_i \omega_i (X_i - \bar{X})\bar{Y}_i}{d\omega_t} = (X_t - \bar{X})(\bar{Y}_t - \bar{Y}),$$

$$\frac{d\sum_i \omega_i (X_i - \bar{X})^2}{d\omega_t} = (X_t - \bar{X})^2,$$

and

$$\frac{d\left[\dfrac{\sum_i \omega_i (X_i - \tilde{X})\,\bar{Y}_i}{\sum_i \omega_i (X_i - \tilde{X})^2}\right]}{d\omega_t} = \frac{(X_t - \tilde{X})(\bar{Y}_t - \hat{Y}_t)}{\sum_i \omega_i (X_i - \tilde{X})^2}.$$

Reassembling eq (A5'):

$$\frac{d\hat{\beta}}{dv} = \frac{\sum_t \omega_t^2 (X_t - \tilde{X})(\bar{Y}_t - \hat{Y}_t)}{\sum_i \omega_i (X_i - \tilde{X})^2} \qquad \text{(A5)}$$

At this point the running index t can be conveniently changed back to the index i. Finally, the substitution of eq (A5) into (A3), and then eq (A3) into (A2') yields:

$$\frac{d^2F}{dv^2} = 2\left[\sum_i \omega_i^3 (\bar{Y}_i - \hat{Y}_i)^2 - \frac{1}{W}\left[\sum_i \omega_i^2 (\bar{Y}_i - \hat{Y}_i)\right]^2 - \frac{\left[\sum_i \omega_i^2 (X_i - \tilde{X})(\bar{Y}_i - \hat{Y}_i)\right]^2}{\sum_i \omega_i (X_i - \tilde{X})^2}\right]. \qquad \text{(A2'')}$$

This second derivative eq (A2'') is a residual weighted sum of squares from regression. To see this, let

$$Z_i \equiv \omega_i (\bar{Y}_i - \hat{Y}_i) \qquad \text{(A6)}$$

and substitute into eq (A2''):

$$\frac{d^2F}{dv^2} = 2\left[\sum_i \omega_i Z_i^2 - \frac{1}{W}\left[\sum_i \omega_i Z_i\right]^2 - \frac{\left[\sum_i \omega_i (X_i - \tilde{X}) Z_i\right]^2}{\sum_i \omega_i (X_i - \tilde{X})^2}\right]$$

$$= 2\left[\sum_i \omega_i (Z_i - \tilde{Z})^2 - \frac{\left[\sum_i \omega_i (X_i - \tilde{X}) Z_i\right]^2}{\sum_i \omega_i (X_i - \tilde{X})^2}\right]$$

The first term on the r.h.s. is the "total" weighted sum of squares of Z. The second term is the weighted sum of squares for the regression of Z on X. Therefore the difference between the two terms is a "residual" sum of squares:

$$\frac{d^2F}{dv^2} = 2\sum_i \omega_i (Z_i - \hat{Z}_i)^2, \qquad \text{(A2)}$$

where $\hat{Z}_i$ is the fitted value of Z_i in a weighted regression of Z on X. Thus, the second derivative is positive for $\omega_i > 0$. The iteration process therefore will never overshoot, and convergence is always assured.

6.4 Extensions

The extension of the convergence proof to the variable s_b^2 case is very similar to that given above. Two basic changes are needed. These changes, which introduce a function of X_i, are in the derivative of ω_i and in the definition of Z_i.

$$\frac{d\omega_i}{dv} = -g(X_i)\,\omega_i^2$$

and

$$Z_i = \omega_i g(X_i)(\bar{Y}_i - \hat{Y}_i).$$

Equation (10) represents an example of a variable s_b^2. For that case,

$$g(X_i) = (c + dX_i)^2.$$

The reader may note that the new Z_i contains X_i, and that Z_i is regressed on X_i. The argument does not require that this regression "make sense", only that the sum of squares can be partitioned by a regression process. Again, convergence is obtained.

The weighted average is a special and simple application of the weighted regression case.

7. Acknowledgments

We wish to thank Miss Alexandra Patmanidou, a graduate student at Johns Hopkins University. She noted that whenever a negative correction in the iteration process is obtained, the process should be terminated and the between-group component of variance set to zero.

About the authors: Robert C. Paule is a physical scientist and John Mandel is a consulting statistician at the National Measurement Laboratory of NIST.

8. References

[1] Paule, R. C., and Mandel, J., Consensus Values and Weighting Factors, J. Res. Natl. Bur. Stand. (U.S.) **87**, 377 (1982).
[2] Mandel, J., and Paule, R. C., Interlaboratory Evaluation of a Material with Unequal Numbers of Replicates, Anal. Chem. **42**, 1194 (1970), and Correction, Anal. Chem. **43**, 1287 (1971).
[3] Cohen, E. R., Determining the Best Numerical Values of the Fundamental Physical Constants, Proceedings of the International School of Physics (Enrico Fermi), Course LXVIII (1980) pp. 581–619.
[4] Birge, R. T., Probable Values of the General Physical Constants, Rev. Mod. Phys. **1**, 1 (1929).
[5] Cochran, W. G., The Combination of Estimates from Different Experiments, Biometrics **10**, 101 (1954).
[6] NIST Standard Reference Materials 1563, 1596, and 1647a.
[7] Currie, L. A., The Limit of Precision in Nuclear and Analytical Chemistry, Nucl. Instr. Meth. **100**, 387 (1972).

Volume 94, Number 3, May–June 1989
Journal of Research of the National Institute of Standards and Technology

News Briefs

Developments

PARTICIPANTS WANTED FOR OSI, ISDN SECURITY PROGRAM

Outside participants are invited by NIST to join in a cooperative research program relating to security and management of computer networks that use the Open Systems Interconnection (OSI) architecture or Integrated Services Digital Network (ISDN) communications services. NIST is looking for participants to provide funding, equipment, and/or staff. A major goal of the program is to expedite the development and commercial availability of OSI and ISDN security products. As part of the program, NIST will provide a facility to define, develop, and test systems for a range of telecommunications, network management, and security services in a distributed information processing environment. For further details, write to NIST, B151 Technology Bldg., Gaithersburg, MD 20899, Attn: Integrated OSI, ISDN, and Security Program.

VENDORS PROVIDE WORKSTATIONS FOR OSI SECURITY WORK

The Open Systems Interconnection (OSI) standards being adopted by both government and industry make it possible to interconnect computer systems manufactured by different vendors for data communications through networks. NIST, through its National Computer Systems Laboratory, has played a major role in developing these standards. Now NIST is working to develop ways to make systems that are secure as well as open. To help NIST develop security protocols for OSI, three major U.S. computer vendors have loaned equipment to the NIST OSI Security Laboratory. NIST will use this equipment to perform research and to develop specifications that can be used as the basis of Federal Information Processing Standards. (FIPS are developed by NIST for use by the Federal Government.)

STANDARD FOR INTERCHANGING DOCUMENTS PROPOSED

Trying to interchange documents among different document or text processing systems such as desktop publishing systems can be a frustrating, sometimes impossible, experience. A new Federal Information Processing Standard (FIPS) formally known as Document Application Profile (DAP) for the Office Document Architecture (ODA) and Interchange Format Standard is being proposed by NIST and should make the process easier. (FIPS are developed by NIST for use by the federal government.) The profile was developed by participants, primarily vendors and users of computer networks, of the long-running NIST Workshop for Implementors of Open Systems Interconnection, and is based on an international voluntary industry standard. A copy of the proposed standard may be obtained from the Standards Coordinator (ADP), NIST, B64 Technology Bldg., Gaithersburg, MD 20899.

MERCURY ION LASER-COOLED TO LIMIT

Scientists at NIST's Time and Frequency Division, Boulder, CO, have succeeded for the first time in laser-cooling a bound atomic ion to its fundamental limit. "We pushed the atom into the ground state of its confining well. That's the end of cooling for a bound particle," says project leader David J. Wineland. Their finding is important for spectroscopy, a study of the nature of matter through various radiations it emits. One result may be the development of a highly sensitive spectrum analyzer. A report on their work appears in the Jan. 23, 1989, issue of Physical Review Letters. They

shined laser light on a mercury ion sideband frequency generated by the Doppler effect associated with thermal motion. The result was to reduce the ion's kinetic energy, limit its movement, and sharpen its spectral features. The ion was confined in a radio frequency trap.

NIST TO STUDY NEW POLYMER RESINS FOR INDUSTRY

E. I. du Pont de Nemours & Co., Inc., has established a cooperative program at NIST to study the chemical and physical behavior of newly developed methacrylate macromonomers, and to determine how well the new materials blend with other resins. The methacrylate macromonomers can be copolymerized by conventional methods or by an electron beam process. Du Pont will supply NIST scientists with specially prepared samples of the materials for examination by several analytical methods. The primary research tools will be small-angle neutron scattering (SANS), a technique where low-energy neutrons from the NIST research reactor are used to characterize the structures of materials on a nanometer scale, and small-angle x-ray scattering (SAXS) which provides information on the phase separation of molecules and polymer chain networks. The NIST Research Associate Program provides an opportunity for scientists from industry, technical societies, universities, and other organizations to conduct cooperative research on programs of mutual interest.

NEW BUILDING CRITERIA FOR PRISONS

Overcrowded and aging, deteriorating prisons have produced a rapid increase in the United States in construction of new facilities. Over $1.5 billion was spent to build new jails and prisons in both 1985 and 1986. But little information exists specifically for the special materials, equipment, and systems used in these facilities. As a result, many correctional agencies have experienced equipment and system performance problems leading to expensive retrofits, repairs, or other fixes. In a project for the U.S. Department of Justice, researchers in the NIST Center for Building Technology have developed preliminary performance criteria to help in the selection, application, and maintenance of building materials, equipment, and systems. A report covers criteria such as choosing a site, selecting appropriate fencing and intrusion detection systems, and developing structural systems. Preliminary Performance Criteria for Building Materials, Equipment and Systems Used in Detention and Correctional Facilities (NISTIR 89-4027) is available from the National Technical Information Service, Springfield, VA 22161 for $21.95 prepaid. Order by PB #89-1148514.

NIST STUDYING UNINTENTIONAL EED FIRING

Electroexplosive devices (EEDs) are electrically fired explosive initiators used in a wide variety of applications from triggering air bags in cars to separating stages in rockets. EEDs are susceptible to unintentional triggering by electromagnetic (EM) fields such as those from local radio transmitters. To help cope with this problem, NIST engineers and statisticians have studied the statistical probability of an EED firing when excited by an electromagnetic pulse of given width and amplitude. The NIST researchers have produced probability plots, called firing likelihood plots, which should assist electrical engineers when designing applications for EEDs. Methods of measuring the time and energy required to fire an EED with a single current pulse also are given. For a copy of this study, contact Fred McGehan, NIST, Division 360.2, Boulder, CO 80303.

CD-ROM SPEECH DATABASE AVAILABLE

As part of its speech recognition research to help computers become better listeners, researchers in the NIST National Computer Systems Laboratory have produced the first speech database in this country in CD-ROM (compact disc-read only memory) format. The database consists of digitized speech data for 420 talkers speaking 4,200 sentences. NIST has been working with private industry and the Defense Advanced Research Projects Agency to develop ways such as this database to measure the performance of speech recognition systems. A limited number of discs are available from David Pallett, NIST, A216 Technology Bldg., Gaithersburg, MD 20899; telephone: 301/975-2935.

NIST REPORT SUMMARIZES INVENTIONS PROGRAM

A portable pothole patcher, a new composite material made of high-strength fibers, a new process for continuous casting of steel cylinders, and a lightweight aluminum cylinder which makes it practical to use natural gas as a vehicle fuel are among the 400-plus inventions which have received support from the federal Energy-Related

Inventions Program. The program, which began in 1975, is conducted jointly by NIST and the U.S. Department of Energy and aims at helping inventors get their ideas from the workshop to the marketplace. NIST provides, at no cost to the inventor, evaluations of energy-related inventions and recommends those it considers promising to DoE. In turn, DoE can provide financial support or help in marketing an inventor's idea. A new report is available which describes the program as well as the inventions which have been recommended for DoE support. Energy Related Inventions Program: A Joint Program of the Department of Energy and the National Institute of Standards and Technology Status Report (NISTIR 88-4005) can be ordered from the National Technical Information Service, Springfield, VA 22161, for $36.95 prepaid. Order by PB #89-141154.

DIAMOND FILMS PRODUCE NEW GEMS

Ancient alchemists did not succeed in changing base metals into gold, but scientists today are able to produce synthetic diamonds from common organic materials. With modern technology, hydrocarbon vapors mixed with hydrogen can be made to deposit a film of diamond on hot objects. Materials scientists at NIST are developing the measurement information that industry needs to produce diamond films with many of the properties of natural diamond. The physical and chemical properties of diamond make it a highly desirable material for aerospace products, electronics, and industrial equipment. At NIST, the scientists are evaluating the production of diamond films by a hot- filament, chemical vapor deposition (CVD) method. Other studies include measuring the thermal conductivity of diamond and developing a better understanding of how defects such as nitrogen impurities and crystal lattice vacancies or voids can affect the performance of diamond films. For further information on the diamond film research program, contact Dr. Albert Feldman, NIST, A329 Materials Bldg., Gaithersburg, MD 20899; telephone: 301/975-5740.

NEW WAY TO EVALUATE PROTECTIVE COATINGS ON METALS

Researchers at the NIST Center for Building Technology have developed a fast, reliable technique for evaluating the performance of organic coatings used for controlling metallic corrosion. In addition to being a threat to the safety and reliability of structures and products, metallic corrosion annually costs the United States an estimated $160 billion. About one-fourth of this cost is for paints, platings, or other surface coatings used to combat corrosion. While other evaluation methods are available, they often are time consuming, sometimes taking months, or may require expensive equipment. The new NIST electrochemical technique is quick (15 minutes to several hours depending on the coating), reproducible, and causes very little perturbation to the coating. In addition, the testing procedure is simple and uses commonly available instrumentation. The method also is believed to have other applications such as screening new coatings and corrosion inhibitors and evaluating the effect of new surface preparation techniques on the performance of the coating and metal system. A report, An Electrochemical Technique for Rapidly Evaluating Protective Coatings on Metals (Technical Note 1253), is available from the Superintendent of Documents, U.S. Government Printing Office, Washington, DC 20402, for $1.50 prepaid. Order by stock no. 003-003-02910-6.

ABSTRACTS OF RECENT PUBLICATIONS AVAILABLE

Researchers in high-temperature superconductivity will be interested in a recent NIST publication that lists abstracts of 61 NIST papers in this field between March 1987 and May 1988. Topics include critical current, crystal structure, electrical contacts, Josephson effect, and magnetic measurements. High-Temperature Superconductivity: Abstracts of NIST Publications, 1987-1988 (SP 759) is available from the Superintendent of Documents, U.S. Government Printing Office, Washington, DC 20402. Order by stock number 003-003-02902-5 for $2 prepaid.

COLLECTED PAPERS ON ION RESEARCH

Some of the world's most advanced research on laser cooling and storage of atomic ions is performed at NIST's Boulder, CO laboratories. A recent publication, Trapped Ions and Laser Cooling II (TN 1324), reproduces a number of papers of this Time and Frequency Division research group and is a companion to an earlier collection of papers. Subjects covered include spectroscopy and frequency standards, quantum jumps, and nonneutral plasma studies. The publication is available from the Superintendent of Documents, U.S. Government Printing Office, Washington, DC 20402. Order by stock number 003-003-02918-1 for $10 prepaid.

CHEMICAL STRUCTURE OF DNA DAMAGE UNCOVERED

For the first time, researchers have determined the chemical structure of a major type of DNA damage caused by oxygen-derived free radicals. Such free radicals, highly reactive groups of atoms with an unpaired electron and very short lifetimes, have been linked to cancer, among other ailments. The methods used by the NIST researchers should help scientists study this type of DNA damage in living cells and gain deeper understanding of its biological effects. The NIST researchers uncovered the structure of hydroxyl radical-induced DNA-protein cross-links, which is damage caused when DNA forms a chemical bond with proteins inside the cell nucleus. This damage to DNA eventually causes chemical changes in the cell that result, for example, in altered proteins.

NIST, NSF PLAN JOINT NEUTRON RESEARCH FACILITY

NIST and the National Science Foundation (NSF) have announced plans to develop a Center for High Resolution Neutron Scattering (CHRNS) for research in chemistry, physics, biology, and materials science. The center will include two state-of-the-art instruments to be built at the recently dedicated NIST Cold Neutron Research Facility, with funding from NSF. The new instruments will probe the microstructure and atomic and molecular dynamics of a wide range of materials, and be competitive with the best such facilities in the world. The center will be managed as a national facility, open to qualified users from universities, industries, government agencies, and nonprofit organizations both U.S. and foreign. Proposals for research time will be evaluated on the basis of scientific merit by a program advisory committee. The first instrument is expected to be complete and operating within 2 years.

MEASURING HIGH-TEMPERATURE SUPERCONDUCTORS

NIST researchers have developed a novel apparatus for variable-temperature measurements of high-temperature superconductors. Termed a cryogenic bathysphere, it can rapidly (in 10 minutes) test superconductors over a range of temperatures from 300–4 K, or it can be used to stabilize the temperature at a given value. The tiny (3-centimeter-width) device has no moving parts and can be used in compact spaces such as shipping Dewars and small-bore high-field magnets. The apparatus has been tested successfully in liquid helium and liquid nitrogen by measuring the resistance-versus-temperature curves of several superconductors. A paper describing a prototype device is available from Fred McGehan, Division 360.2, NIST, Boulder, CO 80303.

STEEL IN FRACTURE TEST SETS U.S. RECORD

Just how tough is a 6-inch thick piece of steel? NIST researchers performed a series of tests on thick steel plates to learn more about how cracks might travel and stop in large pieces of metal. The NIST research team learned that it took 5.94 million pounds of force in tension pulling force to fracture a 6-inch thick, 40-inch wide new steel plate: a U.S. record for fracture tests. All information so far from the tests indicates that the fracture toughness of these steels at the point of crack arrest significantly exceeds minimum values used in applicable design codes and standards. This new information may be used to revise industry codes and standards and will be useful in the design of all types of steel structures including bridges, ships, and buildings, as well as for equipment in industrial plants and utilities.

NIST INVITES VENDORS FOR GOSIP EVALUATION PROJECT

The National Computer Systems Laboratory at NIST is developing guidelines to help users evaluate different implementations of GOSIP (Government Open Systems Interconnection Profile) applications. To help expedite the project, vendors are invited to lend to NIST software and hardware which implements Message Handling Systems (MHS) and File Transfer, Access, and Management (FTAM) applications. Currently, GOSIP supports both applications. GOSIP was approved last fall as a Federal Informaton Processing Standard. (FIPS are developed by NIST for use by the Federal Government.) The standard defines a common set of data communication protocols which enables computer systems developed by different vendors to communicate and enables the users of different applications on these systems to exchange information. For further information on the evaluation project, contact Steve Trus, NIST, B225 Technology Bldg., Gaithersburg, MD 20899; telephone: 301/975-3617.

NATIONAL EARTHQUAKE AWARENESS WEEK

The catastrophic earthquake which struck Armenia last December is a reminder of the threat to lives, property, economic activity, and national security posed by earthquakes. To promote awareness of earthquakes, Congress designated the first week in April 1989 as National Earthquake Awareness Week. But, while earthquakes are an inevitable hazard, they are not an inevitable disaster. Structures can be made earthquake resistant. As part of the National Earthquake Hazards Reduction Program, NIST is working to improve the performance of buildings and other structures subjected to earthquakes. NIST provides research and technical support for the development of improved seismic design and construction practices. The NIST program includes both laboratory research and experiments and post-disaster investigations. A fact sheet on the program is available from the NIST Public Information Division, Jan Kosko, A909 Administration Bldg., Gaithersburg, MD 20899; telephone 301/975-2762.

FIBER-MATRIX INTERFACE PROPERTIES VIA AN INSTRUMENTED INDENTER TECHNIQUE

A commercial microhardness tester has been instrumented to provide measurement of the fiber-matrix interface properties of a ceramic matrix composite. The technique uses a strain gage load cell and a pair of capacitance probes to directly determine the force on and displacement of a fiber in the matrix. The system can be used to determine both fiber-matrix debond strengths and interfacial frictional stresses. These properties are important for determining the occurrence of matrix microcracking and, hence strain limits in the composite as it is loaded in service.

Loads up to 1 kg can be used and displacements up to 25 micrometers can be obtained with this system. Sample sizes are typically $5 \times 6 \times 0.5$-3 mm and require at least one well-polished surface. The system can be used to perform either indentation push-in or indentation push-out tests on a variety of composites. The push-in test requires only that the fiber be pushed into the matrix while the push-out test pushes the fiber out through the other side of the composite. Examples of typical materials characterized to date include CVI SiC/SiC fiber, borosilicate glass/SiC monofilament, and lithium aluminosilicate glass-ceramic/SiC fiber.

NIST COLLABORATION WITH OAK RIDGE NATIONAL LABORATORY ON NEUTRON STANDARDS

The combined resources and measurement capabilities of NIST and the Oak Ridge National Laboratory are being utilized to obtain a high-precision measurement of the neutron interaction with the boron isotope with an atomic mass of 10. This interaction is one of the most widely used standards in the determination of neutron flux. Because neutrons are uncharged, they cannot be measured directly. The neutron interaction with the boron isotope is easy to utilize because a gamma ray is released as a result of the interaction. The easily detected gamma ray can then be used to indicate the intensity of the neutron flux. Large uncertainties are now associated with the measurement for neutrons having energies above 500,000 electron-volts. NIST will take its carefully calibrated neutron flux detector to Oak Ridge where it will be used to calibrate the neutron flux generated by the Oak Ridge Electron Linear Accelerator. The calibrated neutron flux can then be used to make a precise measurement of the boron interaction.

MAJOR NIST COLLABORATION TO STUDY NOVEL MAGNETIC SYSTEMS

NIST Scientists have been participating in a multi-institutional effort at the National Synchrotron Light Source (NSLS) to study novel magnetic systems created in situ by molecular beam epitaxy (MBE). To date, the work has concentrated on establishing a spin-polarized, angle- and energy-resolved, photoemission apparatus on the U-5 beamline of the uv storage ring.

This project is unique in a number of ways: (1) The research team consists of 10 principal investigators from eight institutions nationwide. These are national labs (NIST, Argonne, NRL, and NSLS), universities (Rice, U. Texas at Austin, and Northwestern), and an industrial lab (AT&T Bell). (2) The beamline is the only spin polarized photoemission facility in the United States and the only one in the world with a movable spin analyzer to permit angular studies. (3) It is one of very few beamlines in the United States to have an MBE capability. (4) The experiment is being carried out on the highest flux uv beamline at NSLS. It is based on an undulator currently installed in a straight section of the ring. During the next 2 years this same group, acting as an Insertion Device Team, will install a new state-of-the-art undulator now under construction.

The beamline has recently been used to take spin polarized photoemission data. The object of future experiments will be to observe the magnetic properties, e.g., anisotropy, Curie temperature, remanence magnetization, etc., as a function of layer thickness and growth methodology, and to correlate them with the spin-dependent electronic structure we measure. We expect this facility to greatly extend our ability to study new and interesting magnetic systems.

ATOMIC POSITIONS FROM X-RAY STANDING WAVES

Recent experiments carried out at the Cornell High Energy Synchrotron Source (CHESS) by NIST and CHESS scientists have demonstrated a new method of determining adsorbate positions on crystals with improved accuracy. x-ray standing waves that occur in the process of diffraction from the crystal substrate excite the adsorbed atoms, which fluoresce. Slight changes in crystal alignment translate the standing waves and give the atomic registration.

The novel element in these experiments is the application of the technique to the geometry of glancing incidence. This gives accurate position information parallel to the surface and allows for the possibility that the measurement can be made not only at a surface but at an interface between two different crystalline materials.

PATENT APPLICATION ON NEW X-RAY DIFFRACTION DEVICE

Scientists from the Surface Science Division and the Semiconductor Electronics Division have recently applied for a patent on a new method of detecting the Bragg diffraction condition of x rays incident on a crystal. The determination of diffraction, an extremely common phenomenon in physics experiments, has always been made by monitoring the existence and intensity of the diffracted beam. The novel approach takes advantage of large changes in intensity and penetration depth of the x-ray fields inside the diffracting crystal itself. A semiconductor detector is actually implanted inside the diffracting crystal and responds to small amounts of energy that are always absorbed in the diffraction process. The invention has potential applications in such areas as medical angiography.

MAGNETIC THIN FILMS WITH LARGE PERPENDICULAR MOMENTS

A class of ultrathin magnetic films has been discovered that is ferromagnetic at room temperature and has both a large magnetic moment (high-spin state) and a large perpendicular magnetic anisotropy holding the moment normal to the thin film plane. Such perpendicular anisotropies are a much sought-after property because of their potential for ultrahigh-density information storage in advanced magnetic-recording media.

A key ingredient in achieving these unusually favorable properties has been the ability to optimize the epitaxial growth conditions using the NIST-developed technique of XPS forward-scattering crystallography. Optimum conditions consist of deposition of Fe on Cu at cryogenic temperatures, annealing at 350 K, and deposition of Cu on the Fe at room temperature. This process can be repeated cyclically to produce Cu-Fe superlattices, which have been found to retain the favorable magnetic properties.

This work is a result of collaborative research between scientists at NIST, the Simon Fraser University in Canada, and Cambridge University in England. The work highlights the important potential of such artificially structured materials both for improved understanding of the basic physics of magnetism and as useful novel materials for important technologies.

Calibration Services

INDUSTRY HELP REQUESTED ON COAXIAL CONNECTORS

NIST is interested in learning from the microwave industry of new metrology-grade precision coaxial connectors developed by particular companies. Companies desiring NIST to provide calibration services for components with new connectors are encouraged to furnish NIST with appropriate check standards, air line impedance standards, and test port adapters to use with NIST six-port measurement systems. NIST can then provide measurements traceable to these standards with an uncertainty determined by NIST. The institute provides calibration services for passive devices over the frequency range from 50 MHz to 26.5 GHz with plans to expand to 50 GHz. The standards used by NIST to support coaxial impedance

measurements in this frequency range are lengths of precision air-dielectric transmission lines. In developing these standards, NIST tries to avoid using components or designs available from only one manufacturer; NIST does not wish to favor or become dependent on any one manufacturer. For more information, contact Ramon L. Jesch, NIST, Division 723.01, Boulder, CO 80303; telephone: 303/497-3496.

NEW CALIBRATION SERVICES USERS GUIDE AVAILABLE

The new NIST Calibration Services Users Guide 1989-1990 Special Publication 250 (SP 250) lists the calibration services, special test services, and measurement assurance programs (MAPs) available from NIST. The physical measurement services are designed to help the makers and users of precision measurements achieve the highest possible levels of quality and productivity. The hundreds of services described in the guide are the most accurate calibrations of their type available in the United States. They directly link a customer's precision equipment or transfer standards to national measurement standards. The calibrations and special tests include NIST services that check, adjust, or characterize instruments, devices, and sets of standards. The MAPs are quality control programs for calibrating a customer's entire measurement system. The guide also lists NIST technical experts who may be contacted for information on services and measurement problems. For information on the NIST measurement services program, or to obtain a copy of SP 250, contact the Office of Physical Measurement Services, NIST, B362 Physics Bldg., Gaithersburg, MD 20899; telephone: 301/975-2005.

NCSL AD HOC COMMITTEE 91.3 ON THE CHANGE OF THE TEMPERATURE SCALE

The National Conference of Standards Laboratories (NCSL) ad hoc Committee on the Change of the Temperature Scale met in open session on January 26, 1989, in Anaheim, CA, during the Measurement Science Conference. The committee was formed last year to facilitate the change from the International Practical Temperature Scale of 1968 (IPTS-68) to the new scale that will be implemented on January 1, 1990, and that will be known as the International Temperature Scale of 1990 (ITS-90). The meeting was well attended, both by committee members and by guests. Standards laboratories and instrument manufacturers were well represented. The latest draft of the ITS-90 and the implications of this new scale were discussed in considerable detail. Although the scale is not yet in its final form, it will be complete by September, at which time the CCT will meet and recommend it to the International Committee of Weights and Measures (CIPM). The CIPM will then adopt it in October. Those involved in temperature measurements are being kept informed of changes in the scale, and will be told what steps they should take to either implement the scale or ensure that their measurements are on the ITS-90, beginning in 1990.

Standard Reference Materials

IMPROVING LEAD-IN-FUEL ANALYSES IS AIM OF MATERIALS

Elevated lead levels in the environment could be caused by a number of sources, but one of the chief culprits may still be the alkyl lead used as an additive in gasoline, according to some reports. Because the Environmental Protection Agency regulates lead content in fuel emissions as part of air quality standards, the petroleum industry needs accurate measurement techniques to ensure compliance with federal emission limits. To aid industry in calibrating the instruments that analyze fuel samples and to help confirm the accuracy of measurement techniques, NIST has developed four different standard reference materials (SRMs). Individually, the SRMs consist of gasoline-like fuel in vials, with each SRM representing a different certified lead level (.0297, .0506, .0733, and 2.045 grams per gallon of lead, respectively). By analyzing the SRM fuel the same way as a fuel sample, a chemist can gauge how well analytical instruments and techniques are working at four different lead levels. The new SRMs, numbered 2712 through 2715, are available for $110 each from the Office of Standard Reference Materials, NIST, B311 Chemistry Building, Gaithersburg, MD 20899; telephone: 301/975-6776.

NEW MATERIALS CAN HELP GAUGE COAL SULFUR CONTENT

Because sulfur emissions from coal-fired industrial plants are regulated by environmental agencies, it is important for coal and utility companies to know

how much sulfur is contained in a given coal batch. Likewise, coal companies and their customers need accurate determinations of sulfur and ash content along with calorific value to set fair tonnage prices of coal shipments. A new NIST Standard Reference Material (SRM) can help boost the accuracy of all these measurements by allowing evaluation of laboratory methods and calibration of instruments used in coal analysis. The SRM, which consists of a 50-gram bottle of bituminous coal, is certified for its sulfur and ash content as well as its calorific value. Also included are non-certified values of 23 other elements. The new material (SRM 2692) costs $102 and is available from the Office of Standard Reference Materials, NIST, B311 Chemistry Building, Gaithersburg, MD 20899; telephone: 301/975-6776.

NEW AUSTRALIAN BAUXITE ORE STANDARD ISSUED

A new bauxite ore Standard Reference Material (SRM) is available from NIST for aluminum producers to use in analyzing raw materials. SRM 600, Bauxite from the Darling Range, Australia is the fifth in a series of bauxite standards to be issued by NIST under a cooperative program with industry through ASTM. The other SRMs are Arkansas, Surinam, Dominican, and Jamaican. SRM 600 is in the form of a fine powder for use in validating experimental data and analytical methods. It provides certified concentrations and estimated uncertainties for 15 inorganic constituents. SRM 600 may be purchased for $94 per 60-gram unit from the Office of Standard Reference Materials, NIST, B311 Chemistry Building, Gaithersburg, MD 20899; telephone: 301/975-6776.

Standard Reference Data

DIPPR DATABASE EXPANDED TO 1,023 PURE COMPOUNDS

More than 250 pure chemical compounds have been added to a computerized database on the thermodynamic and physical properties of chemicals. The database, DIPPR (Design Institute for Physical Property Data), Data Compilation of Pure Compound Properties, 1989, now contains information on 39 properties for 1,023 pure chemical compounds of high industrial priority. The database provides chemical engineers, manufacturers, and scientists in industry, government, and universities with quick access to important information on the behavior of substances and their reactions at various temperatures. The chemicals in the database were selected by the industry members of the American Institute of Chemical Engineers' (AIChE) DIPPR group, and are considered to be the most important ones to industry. For information on fees and license agreements for NIST Standard Reference Database 11, DIPPR, Data Compilation of Pure Compounds, 1989, contact the Office of Standard Reference Data, NIST, A323 Physics Building, Gaithersburg, MD 20899; telephone: 301/975-2208.